MASTER OF SCIENCE THESIS

Strain Rate Dependent Compression Properties of Carbon-Epoxy Laminates

Tiago Filipe

Faculty of Aerospace Engineering · Delft University of Technology

Strain Rate Dependent Compression Properties of Carbon-Epoxy Laminates

Master of Science Thesis

For obtaining the degree of Master of Science in Aerospace Engineering
at Delft University of Technology

Tiago Filipe

14 August 2017

Faculty of Aerospace Engineering · Delft University of Technology

The work in this thesis was supported by Audi AG. Their cooperation is gratefully acknowledged.

Delft University of Technology
Faculty of Aerospace Engineering
Department of Aerospace Structures and Materials

GRADUATION COMMITTEE

Dated: 14 August 2017

Chair holder:

Prof.dr. Chiara Bisagni

Committee members:

Dr. Christos Kassapoglou

Ir. Michiel Schuurman

Ing. Tobias Schmack

Abstract

With increasing usage of fibre-reinforced composites for structural components across the automotive and aerospace industry, it became crucial to understand how this kind of materials behave when subjected to high loading rates, which are encountered in the case of crash events. Another important aspect is the correct implementation of the strain rate dependent properties on the numerical models used to perform finite element simulations, as it can lead to more accurate impact simulations.

The current work presents a study on the effect of the strain rate on the compressive mechanical properties of carbon-epoxy laminates.
A servo-hydraulic testing machine, together with high-speed cameras and a contactless strain measurement technique, were used to perform static and dynamic impact tests on rectangular specimens made of T700-DT120 carbon-epoxy laminates of five different layups, each subjected to six distinct impactor velocities. Throughout the strain rate range tested, no significant effect of the deformation rate on the compressive longitudinal, transverse and shear moduli was found. However, improvements of other mechanical properties were evident, which have a considerable consequence on the laminate's response under high rates of deformation. In longitudinal direction (in-fibre direction), a moderate increase in compressive strength was detected, accompanied by an analogous growth in failure strain. A more significant increase was found for the matrix-dominated properties of the laminate, such as the transverse compressive strength and yield stress/strain, and similarly for the shear response.
Impact experiments were also performed on components using a more complex cross-section shape with the objective of understanding how the strain rate dependent properties observed on simple rectangular specimens develop for specimen shapes more commonly used throughout the automotive industry. A meaningful increase in failure load with increasing strain rate was identified, which is in line with the growth observed for simple rectangular specimens.

The experimentally obtained rate dependent compressive properties were implemented in a Pam-Crash® numerical model and simulations that resemble the experimental tests were performed in order to confirm that not only the rate dependent properties were well implemented, but also that simulations are able to accurately predict the behaviour of carbon-epoxy structural components under impact loads. A good agreement between experiments and simulations was obtained for both types of cross-section specimens considered. The simulations carried out were able to accurately predict the increase in failure load of the structural component tested, with increasing rates of loading.

The presented work concludes that the strain rate dependent compressive properties of typical structural components made of carbon-epoxy laminates can be accurately determined by performing impact tests on specimens with a simple shape/cross-section. By implementing the dynamically-obtained material properties in numerical models, more accurate full vehicle crash simulations can be performed, which will not only result in realistic results, when compared with experimental data, but also improvements in the components' optimization process that ultimately will lead to lighter structures.

Acknowledgements

First of all, I would like to express my sincere gratitude to Dr. Kassapoglou for his availability and supervision throughout this project. His valuable suggestions were tremendously appreciated and contributed greatly to the improvement of my work. I am also especially grateful to Ing. Tobias Schmack for his guidance, encouragement and valuable advices, not only throughout the seven months that I have spent at Audi, but also during the process of writing this thesis.

I would like to extend my gratitude to everyone I've met at Audi that, in some way or the other, have contributed to the development of my research. A special thanks to the laboratory technicians for their continuous technical support, and to other Audi interns and students for their assistance whenever I needed and the enjoyable times spent together.

Throughout my time as a student in Delft I had the opportunity to make exceptional friends, with whom I shared not only great academic experiences, but also unforgettable moments. As a foreign student in the Netherlands, I have felt at home in Delft, greatly due to you guys.

On a more personal note, I am grateful to my girlfriend Marta for her unconditional support and encouragement during the whole time I was away. Lastly, and most importantly, I would like to thank my close family, especially my brother Pedro and my parents, Rosa and João, who have taught me that nothing can be achieved without commitment, effort and sacrifice. Thank you.

Delft, University of Technology
14 August 2017

Tiago Filipe

Table of Contents

List of Figures

List of Tables

Nomenclature

Abbreviations

CFRP	Carbon fibre-reinforced polymers
CP	Center point
CV	Coefficient of variation
DIC	Digital Image Correlation
DSC	Differential Scanning Calorimetry
FE	Finite Element
FML	Fibre Metal Laminate
FRP	Fibre-reinforced polymers
GFRP	Glass fibre-reinforced polymer
PoF	Probability of Failure
QI	Quasi-isotropic
QS	Quasi-static
SHPB	Split-Hopkinson pressure bar
UD	Unidirectional

Greek Symbols

β	King band inclination angle
$\dot{\varepsilon}$	Strain rate
η	Hardening law multiplier
Γ	Compressive modulus loss factor
γ_{12}	In-plane shear strain
γ_y	In-plane shear yield strain
ν_{12}	Poisson's ratio
ϕ^0	Initial fibre misalignment

Π_c	Total energy
σ_1	Longitudinal stress
σ_2	Transverse stress
σ_x	X-direction applied load
σ_{τ_y}	Transverse yield stress
σ_{ij}	Stress tensor components
τ_{12}	In-plane shear stress
τ_y	In-plane shear yield stress
ε_1	Longitudinal strain
ε_2	Transverse strain
ε_{back}	Strain reading on back strain gauge
ε_{front}	Strain reading on front strain gauge
ε_{ij}	Strain tensor components

Latin Symbols

A	Cross-section area
b	Damage function evolution coupling factor
B_y	Bending factor
C_{ij}	Stiffness matrix components
d_{12}	Damage factor: fibre-matrix debonding
d_{22}	Damage factor: matrix micro-cracking
D_{ij}	Fitting law first coefficient
E_1	Longitudinal modulus
E_2	Transverse modulus
F_{ij}	Viscosity function
G_i	Beam's end torsion spring constant
G_{12}	Shear modulus
I	Second moment of area
K	Beam effective length factor
k	Spring constant of elastic foundation
K_i	Beam's end linear spring constant
L	Specimen gauge length
n	Hardening law exponent
n_{ij}	Fitting law second coefficient
P	Longitudinal force
q	Lateral load
$R(\varepsilon^p)$	Stress after yielding
R_0	Yield stress
S	Compliance matrix
t	Thickness

u	Strain energy density
v	Velocity
W	Width
w	Beam out-of-plane displacement
x	Coordinate along beam's axis
$Y_{ij}(t)$	Damage functions evolution
Z_{ij}	Damage functions

Subscripts

$_0$	Initial
$_{crit}$	Critical
$_{fail}$	Failure
$_{lim}$	Limit
$_{max}$	Maximum

Superscripts

^{c}	Compression
^{e}	Elastic
^{p}	Plastic
^{ref}	Reference
^{v}	Viscous

Chapter 1

Introduction

The response of a structure to dynamic loads is an important design criterion across several areas of the engineering field. In the aerospace industry, bird impacts on the wing's leading edge or damage on the jet engine's housing caused by the fracture of a fan blade rotating at high speeds are just a few examples in which the highly dynamic load case is one of the main driving factors for the designs. Similarly, in the automotive industry, the structural components are subjected to dynamic load cases during crash events and must be designed to assure passenger's safety. In other areas of engineering, dynamic loading of the structures is also relevant, such as the occurrence of earthquakes in civil engineering structures, or the constant impact of the waves in marine engineering. In all these cases, it is of the highest importance to understand and predict the behaviour of the used materials under the different strain rates they are subjected to.

Over the past decades, fibre-reinforced plastics have been replacing metals as the main structural material in the transportation sector, specially in the aerospace and automotive industries. This trend is attributed to the high specific properties that fibre-reinforced plastics can achieve, compared to metals, which allows engineers to obtain lighter designs. The reduction in weight is not only beneficial for the vehicles performance, but also to the reduced emission of greenhouse gases, which has seen and will continue to have stricter rules implemented for the upcoming years.

The mechanical properties of many materials depend on the rate at which they are loaded. For metals, a great effort was placed on this topic, resulting in a very good understanding of mechanical properties, failure and damage mechanisms over a wide range of strain rates for the most used metal alloys. On the other hand, composites show more complex damage and failure phenomena, which makes it difficult to fully predict the material response at high loading rates.
Even though there is a lack of knowledge regarding failure and damage propagation on composites, these materials have seen an increase in usage across several applications, most of them subjected to dynamic loading, which led to understanding the behaviour of composite

materials at different strain rates an important topic over the last two decades.

The objective of this thesis is to experimentally investigate the compression response of carbon-epoxy laminates with different layup orientations, under a range of strain rates achievable during a car crash event. Furthermore, the response at different rates is to be implemented in simulation software and the numerical results compared with the experimental ones. In addition, the dynamic investigation is to be extended beyond typical compression specimens, into a generic structural component widely used in vehicles in order to validate if the dynamic mechanical response is also obtainable on a structural level.

The results obtained in this thesis can lead to more realistic results during Audi's full vehicle crash simulations. By implementing the strain rate dependent properties of carbon-epoxy components in the finite element simulations, the numerically obtained mechanical response of the structure becomes closer to the experimental results. Since the material properties tend to increase for higher loading rates, taking this growth into account will result in more accurate crash simulations and, ultimately, lighter structural components.

Chapter 2

Literature Review

In the present chapter, the literature reviewed for this thesis is presented. Firstly, the effect of the strain rate on neat resin and fibre bundles mechanical response is shown. Secondly, investigations containing the loading rate effect on the response of fibre-reinforced polymers (FRP) are separated and presented in terms of tension, compression and shear behaviour. On the third section, the results from the two previous sections are normalised and compared. Fourth section contains a short review of the effects of different specimen geometrical factors on the compression testing of FRP, while the fifth section shows the importance of updating the Finite Element (FE) material cards with strain rate dependent properties. Finally, the thesis objectives and a summary of the chapter are presented on the sixth and seventh sections, respectively.

2.1 Strain rate effect on composite constituents

To understand the mechanical response of fibre-reinforced composites under different loading rates, it is important to determine the response of each of its constituents: the fibres and the resin. This is particularly relevant if one wants to understand the reasoning behind the strain rate dependent properties of fibre-reinforced composites. In this section, a literature review of the mechanical response of each constituent is presented.

2.1.1 Fibre

When studying the strain rate dependency of fibres, it is important to note that only tensile tests using fibre bundles are possible due to technical difficulties related with tensile testing of a single fibre [1].

Xia et al. [2] performed tensile tests on E-glass fibre bundles under strain rates ranging from 1.9×10^{-4} to 1100 s^{-1} using a tension Split-Hopkinson pressure bar (SHPB) apparatus, and reported increases up to 180%, 144% and 18% of the quasi-static (QS) values for the tensile strength, rupture strain and modulus, respectively.

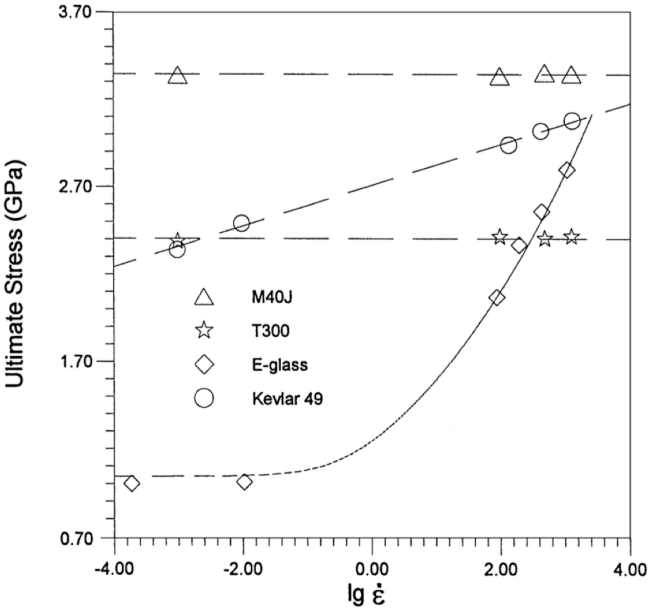

Figure 2.1: Comparison of strain rate effect on the tensile strength of different fibre bundles [1–3]

In a subsequent study, Wang and Xia [1], tested Kevlar® K49 Aramid fibre bundles at a similar strain rate range and noted a strain rate dependency of the fibre's mechanical properties. At a strain rate of 1350 s^{-1}, the increase in tensile strength, rupture strain and modulus is 31%, 17% and 29%, respectively, over the quasi-static values. When compared to the previously obtained increase for E-glass fibre bundle, the properties increase of Kevlar® K49 are significantly lower, but the strain rate dependency is still apparent.
In later studies, Zhou et al. [3, 4], carried out tensile tests under varying strain rates on fibre bundles of three different carbon fibre types: T300, M40J and T700. Their results suggest that both the strength and the rupture strain of all three types of carbon fibre bundles are strain rate insensitive.

Even though the amount of existing literature concerning the strain rate dependency of fibre bundles is quite limited, it is noticeable that the effect of the strain rate on the tensile properties of fibre bundles is remarkably dissimilar for different types of fibres. Figure 2.1 shows a comparison of the strain rate effect on the tensile strength of E-glass fibre bundle, Kevlar® K49 Aramid fibre bundle, T300 and M40J carbon fibre bundles, based on the results presented in the current subsection [1–3].

2.1.2 Neat resin

2.1.2.1 Tension

Gilat et al. [5] used an hydraulic testing machine and a tension SHPB apparatus to perform tensile tests on CYCOM® 977-2 neat epoxy specimens at strain rates varying from 10^{-5} until 400 s^{-1}. In a follow-up study [6], the same authors performed similar static and dynamic

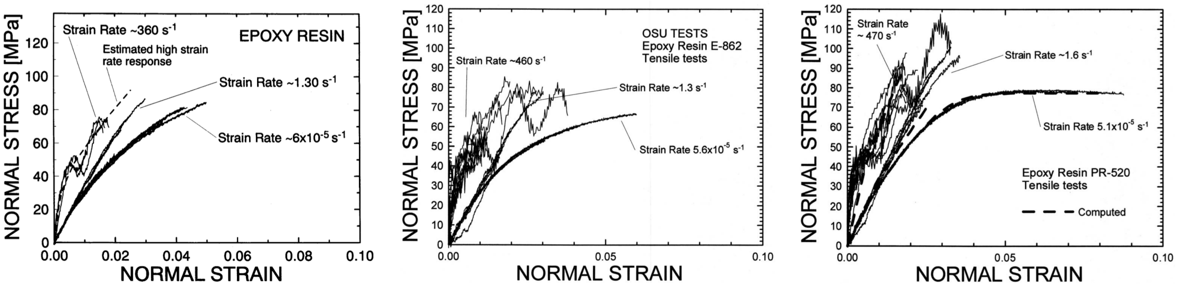

(a) CYCOM® 977-2 **(b)** Epon 862 **(c)** PR-520

Figure 2.2: Tensile stress-strain curves for different epoxy resin systems at varying strain rates [5, 6]

tensile tests on two additional resin systems: Epon 862 and PR-520. Figure 2.2 shows the effect of the strain rate on the tensile stress-strain curves of the three resin systems mentioned in both studies.

In all three epoxy resin systems, the maximum stress increases slightly from low strain rates to dynamic tests performed at moderate and high strain rates. Furthermore, the material response gets more brittle with increasing loading rates, which leads to a reduction in fracture strain for the dynamic tests. The initial modulus increases slightly between low and moderate strain rates - from 2.93 to 3.26 GPa for the Epon 862 resin and from 3.24 to 4.15 GPa for the PR-520 resin [6]. For the high strain rate tests, performed with a tension SHPB, the modulus increases significantly - up to 5.17 and 5.65 GPa for the Epon 862 and PR-520 resins, respectively [6].

Littell et al. [7] also performed quasi-static and dynamic experimental tests on Epon 862 epoxy resin specimens and the resulting stress-strain curves are shown in Figure 2.3. When comparing these stress-strain curves with the ones obtained by Gilat et al. [6] shown in Figure 2.2 **(b)** the main difference is the failure strain. The curves presented by Gilat et al. [6] end at approximately 6 and 3% strain for low and intermediate strain rates, respectively. On the other hand, Littell et al. [7] report tensile stress-strain curves up to 30% strain for similar strain rates. Littell et al. [7] suggest that this difference might be related with the strain measurement technique: Gilat et al. [6] used strain gauges, which have a limited strain measuring range, while Littell et al. [7] used a non-contacting strain measurement technique - Digital Image Correlation (DIC), which has a much broader measuring range.

Nonetheless, the curves from Figures 2.2 **(b)** and 2.3 behave similarly up to 6 and 3% strain for both low and intermediate strain rate, respectively. Furthermore, the dependency of the ultimate stress and yield stress on the strain rate is clear for both studies.

Gerlach et al. [8] performed tension tests on RTM-6 thermosetting resin under a wide range of strain rates. For this, three different testing apparatus were used: a screw-driven tensile testing machine for quasi-static tests, an hydraulic system for moderate loading rates and a tension SHPB to achieve strain rates up to 3800 s^{-1}. Representative stress-strain curves at four different strain rates are shown in Figure 2.4.

The results shown follow the same trend as other previously presented, although the increase in mechanical properties is more substantial due to the higher strain rates achieved. Similarly to the results presented by Gilat et al. [5, 6], the stress-strain curves become more brittle with

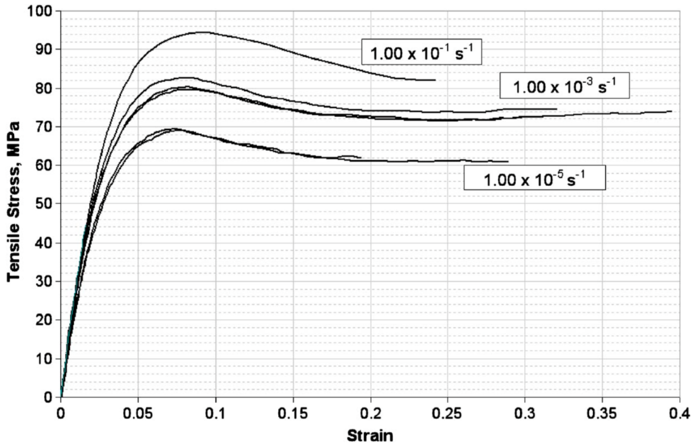

Figure 2.3: Tensile stress-strain curves of Epon 862 neat epoxy resin specimens at different strain rates [7]

Table 2.1: Strain energy density at failure under varying loading rates, for different resin systems [5, 6, 8].

Strain Rate $[s^{-1}]$	Strain energy density at failure $[MJ/m^3]$			
	CYCOM® 977-2	Epon 862	PR-520	RTM-6
10^{-4} to 10^{-3}	1.8	2.8	4.8	8.1
1 to 30	1.5	1.3	1.9	8.4
400 to 1700	1.5	1.1	1.1	3.6

increasing strain rate and the fracture strain decreases. Furthermore, both the initial modulus and the strength increase significantly - approximately a two-fold increase. Additionally, the yield stress more than doubles from the quasi-static value of 75 MPa to 190 MPa at a strain rate of 3800 s^{-1}.

Most results presented in the current section show an increase in strength and modulus, together with a decrease in failure strain, with increasing strain rate. These observations can suggest that the strain energy at failure, i.e. the area under the stress-strain curve, is not dependent on the loading rate.
To better analyse this, the stress-strain curves presented in Figures 2.2 and 2.4 were digitised and the strain energy density at failure determined. Table 2.1 summarizes the results of this analysis for four different resin systems, subjected to three loading rates.
The results presented for the different resin systems are distinct. While the epoxy systems Epon 862, PR-520 and RTM-6 show a clear reduction in stored energy at failure, the resin CYCOM® 977-2 has a relatively constant strain energy level for the different strain rate ranges.

These results suggest that, even though the trend regarding modulus, strength and failure strain with increasing strain rate for all resin systems is similar, the dependency of the strain energy stored at failure for varying loading rates is different for the epoxy systems considered.

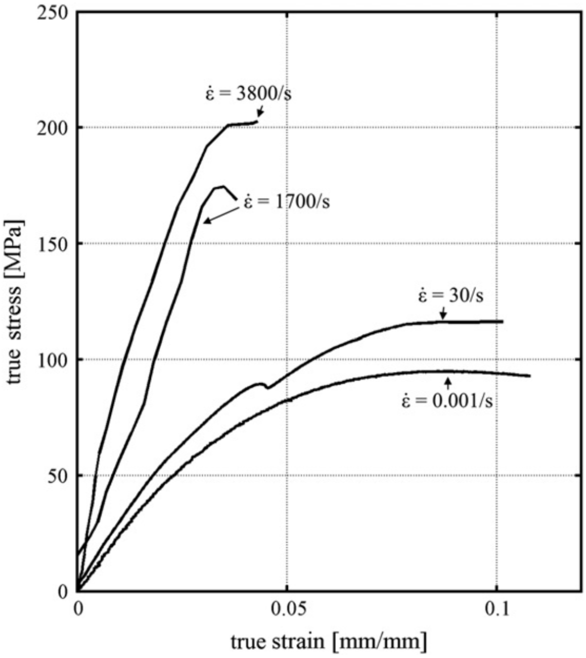

Figure 2.4: Tensile stress-strain curves of RTM-6 thermosetting resin at different strain rates [8]

2.1.2.2 Compression

Gerlach et al. [8] also performed compression tests with RTM-6 thermosetting resin at different strain rates. The representative stress-strain curves at six different loading rates are shown in Figure 2.5. The compressive strain at failure increases from 40% at quasi-static loading rates to 55% at high strain rates, which is the opposite trend as seen for the tension experiments - see Figure 2.4. At intermediate strain rates, no failure was achieved due to restrains in the hydraulic testing apparatus. Similarly to the tension results, there is an indisputable increase of the yield stress and apparent initial modulus with increasing rates of deformation.

Chen et al. [9] and Littell et al. [7] carried out quasi-static and dynamic compression tests on specimens made of similar types of resin. Chen et al. [9] used Epon 828 epoxy resin, while Littell et al. [7] used Epon 862 epoxy resin. The two resin systems have a similar chemical structure, except that the former is diglycidyl ether of bis-phenol A epoxy and the latter is diglycidyl ether of bis-phenol F epoxy.
Figure 2.6 **(a)** and **(b)** show the respective compressive stress-strain curves at different strain rate levels. Considering the same strain rate range - from 10^{-4} to 10^{-1} s^{-1} - the responses of the two resin systems are very much alike until a strain of approximately 7%. After this strain level, the Epon 828 shows a typical compressive behaviour of polymers with a strain softening and a plastic flow region. On the other hand, the Epon 862 epoxy system shows an increasing stress level after yielding. This difference can be explained by the different stress and strain definitions used. Figure 2.6 **(a)** shows true strain and true stress, while **(b)** displays engineering strain and stress.
Nonetheless, in the matching strain rate levels between the two resin systems, the increase in yield stress and peak stress is identical. Furthermore, the initial modulus does not change

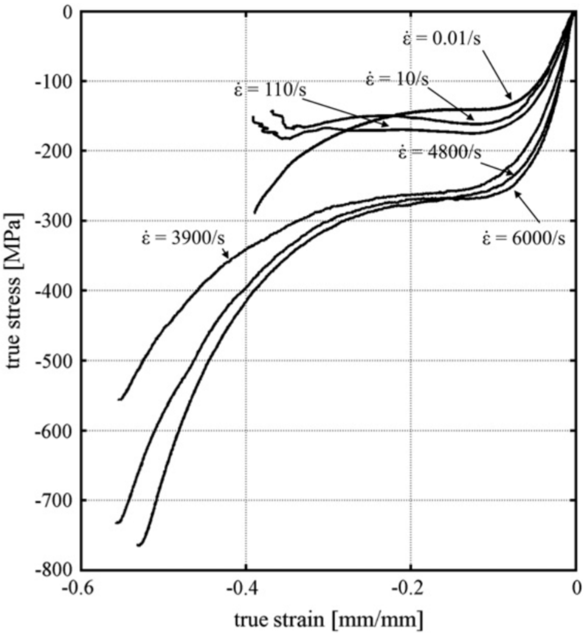

Figure 2.5: Compression stress-strain curves of RTM-6 thermosetting resin at different strain rates [8]

significantly with increasing strain rate.

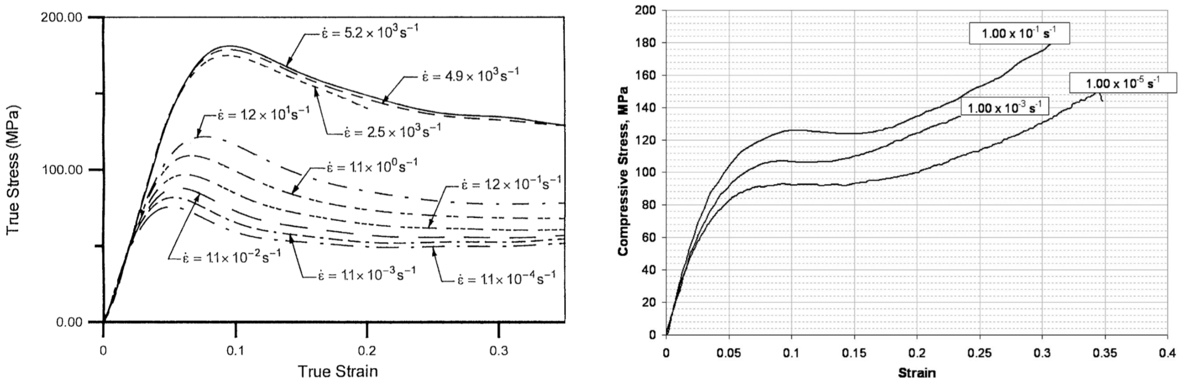

(a) Epon 828 **(b)** Epon 862

Figure 2.6: Compressive stress-strain curves of similar epoxy resin systems at varying strain rates [7, 9]

In a recent study, Tian et al. [10] used three testing rigs to perform compression tests on cylindrical specimens made of neat epoxy resin at low, moderate and high strain rates. The low loading rates (10^{-3} to 10^{-1} s^{-1}) were achieved using a Zwick universal testing machine. The moderate (1 to 35 s^{-1}) and high strain rates (1000 to 3000 s^{-1}) tests were performed using an Instron-8801 universal testing machine and a compression SHPB, respectively. Figure 2.7 presents the compressive stress-strain curves at three different strain rate levels.
The varying material response with increasing strain rate is in line with the previously presented studies. Tian et al. [10] report a 59% increase in yield stress and a 33% decrease in

failure strain for an increase of strain rate from 10^{-3} to 3000 s^{-1}.

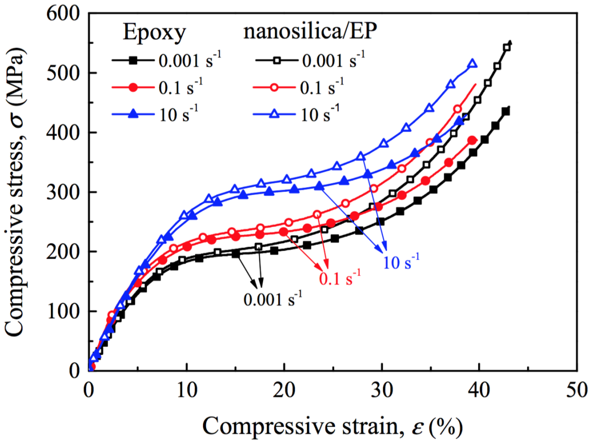

Figure 2.7: Compression stress-strain curves of cylindrical neat epoxy resin specimens at different strain rates [10]

2.1.2.3 Shear

The shear response of neat epoxy resin specimens was investigated by Gilat et al. [6]. Experimental torsion tests using short thin-walled tube specimens were performed with two epoxy resin systems: Epon 862 and PR-520. The low and moderate strain rates were achieved using an hydraulic torsion machine, while the high strain rate tests were carried out with a torsion SHPB. For both resin systems, the shear strength and the shear modulus increases with increasing strain rate. The maximum shear strain reduces with increasing strain rate for the Epon 862 epoxy resin, while the PR-520 epoxy resin maintains the same ductile response for all levels of strain rates, showing no reduction in failure strain.

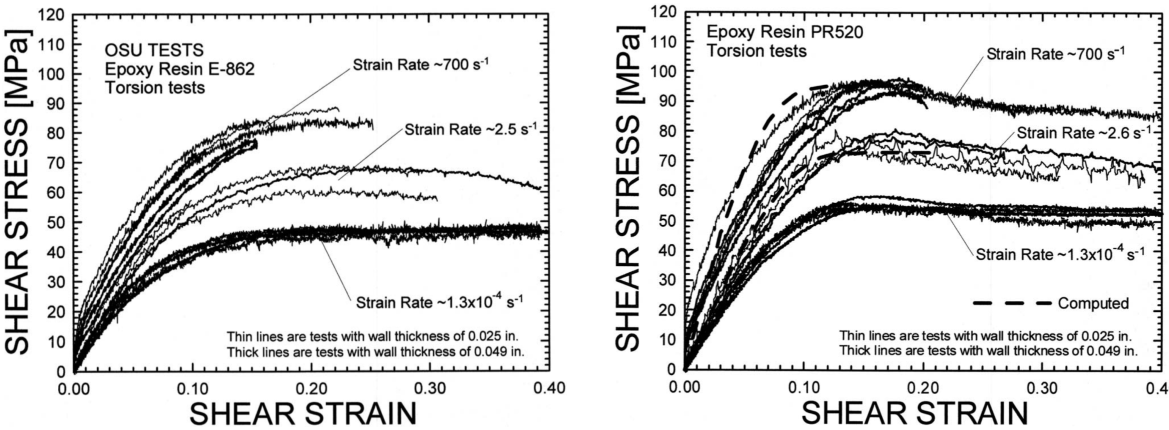

(a) Epon 862

(b) PR-520

Figure 2.8: Shear stress-strain curves for different epoxy resin systems at varying strain rates [6]

Littell et al. [7] also performed static and dynamic torsion tests on thin-walled cylindrical neat Epon 862 epoxy resin specimens. Shear stress-strain curves at three different strain rate levels are shown in Figure 2.9. The authors report an increase of 25% of the shear modulus - from 801 MPa for a strain rate of $1.6 \times 10^{-5}\ s^{-1}$ to 1002 MPa at a strain rate of $1.6 \times 10^{-1}\ s^{-1}$. Moreover, the maximum shear stress also increases by approximately 40% over the same strain rate range.

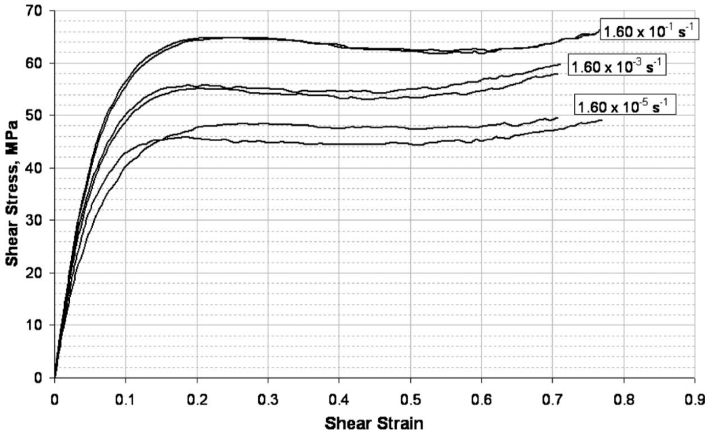

Figure 2.9: Shear stress-strain curves of thin-walled neat Epon 862 epoxy resin specimens at different strain rates [7]

2.1.3 Summary

In this section, the effect of the deformation rate on both the fibres and the resin has been presented by reviewing the available publications. The mechanical response of fibre bundles varies with the type of fibres. Glass and Aramid fibres show increasing mechanical properties with increasing strain rate. On the other hand, carbon fibres are not affected by the deformation rate and display the same ultimate tensile stress, regardless of the deformation speed. Concerning the resin, it was shown that the mechanical response under tension, compression and shear conditions is strain rate dependent for all the epoxy resin systems mentioned. Overall, the maximum stress, the yield stress and initial modulus increase for increasing rates of deformation. Furthermore, in some cases, the material response gets more brittle with increasing strain rate, leading to lower failure strains.

2.2 Strain rate effect on fibre reinforced polymers

2.2.1 Tension

Harding and Welsh [11] performed high strain rate tensile tests on unidirectional (UD) carbon-epoxy composites using a tension SHPB, and found no correlation between the longitudinal tensile properties and the strain rate. Similar results were obtained by Taniguchi et al. [12] by using a tension SHPB to load UD specimens made of T700/2500 carbon-epoxy at strain rates of 100 s^{-1}. Figure 2.10 compares the static and dynamic longitudinal tensile stress-strain curves reported by Taniguchi et al. [12]. The tensile strength, modulus and fracture strain in

fibre direction are not dependent on the strain rate.
In a study to investigate the influence of the strain rate on the mode I fracture behaviour of carbon-epoxy and carbon-PEEK composites, Blackman et al. [13] used a technique based on the propagation of Lamb waves to determine the influence of the strain rate on the composite longitudinal modulus. They report that the composites moduli do not change significantly for different loading rates.
The results presented by Harding and Welsh [11], Taniguchi et al. [12] and Blackman et al. [13] are in agreement with the findings presented in Subsection 2.1.1 for carbon fibre bundles. The longitudinal mechanical properties of composites containing carbon fibres are not strain rate dependent, as the material response in this loading direction is fibre-dominated and this type of fibre shows no dependency on the loading rate.

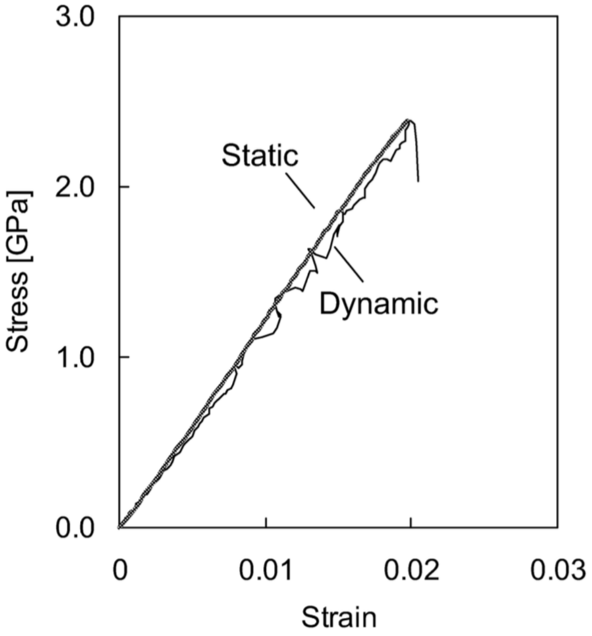

Figure 2.10: Longitudinal tensile stress-strain curves of UD carbon-epoxy at static and dynamic deformation rates [12]

Besides the tension tests on neat epoxy resin presented in Subsection 2.1.2.1, Gilat et al. [5] also performed transverse tension experiments on unidirectional carbon-epoxy composites at varying strain rates, using the same tension SHPB apparatus. Figure 2.11 **(a)** shows the transverse tensile stress-strain curves at three different strain rate levels, as reported by Gilat et al. [5]. The transverse modulus and failure stress increase with increasing strain rate, whereas the variation in failure strain was considered negligible.
Similar results were found by Taniguchi et al. [12] while performing transverse tensile tests on T700S/2500 carbon-epoxy laminates under static and dynamic conditions (Figure 2.11 **(b)**). Taniguchi et al. [12] report increases in transverse tensile modulus and strength of 12.5% and 17.8%, respectively, between quasi-static conditions and strain rates of 100 s^{-1}.

An important feature is the difference in tensile fracture strain between neat epoxy resin specimens (Subsection 2.1.2.1) and the composite in transverse direction. As shown in Figure 2.11, Gilat et al. [5] and Taniguchi et al. [12] report tensile fracture strains below 1% for the transverse direction, which is considerably less than the values reported for the neat epoxy

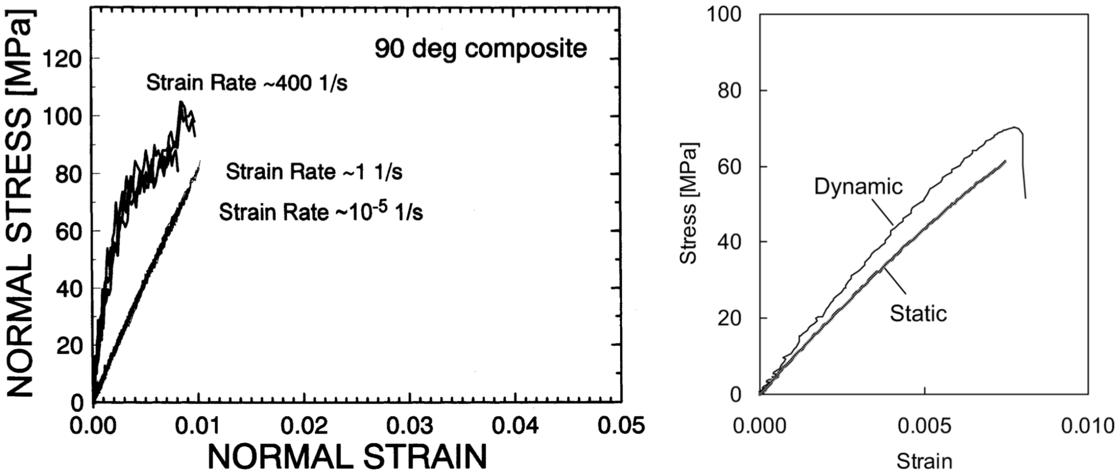

(a) IM7/977-2 carbon-epoxy [5] **(b)** T700S/2500 carbon-epoxy [12]

Figure 2.11: Tensile stress-strain curves of carbon-epoxy laminates with a [90°] layup

specimens. Taniguchi et al. [12] performed microscopic observations of the fracture surface of the [90°] layup specimens at both static and dynamic testing conditions. For both cases, the authors report that the cracks spread adjacently to the fibre-matrix interface, suggesting that the presence of the fibres causes stress concentrations, which leads to debonding of the constituents at low strain levels.

2.2.2 Compression

2.2.2.1 Longitudinal direction

Hsiao and Daniel [14] carried out longitudinal compression tests at different loading rates using unidirectional specimens made of IM6G/3501-6 carbon-epoxy prepreg material. For strain rates below 10 s^{-1}, an hydraulic testing machine was used, whereas higher loading rates were achieved by using a self-developed drop tower apparatus. Figure 2.12 shows the compressive stress-strain curves obtained by Hsiao and Daniel [14] when loading unidirectional specimens in fibre direction at different rates. For the higher strain rate considered ($110\ s^{-1}$), the compressive strength and failure strain increase by 79% and 74% over the static values, respectively. The initial modulus shows a small but negligible change with varying strain rate.

Hosur et al. [15] used a compression SHPB testing rig to perform dynamic in-plane compression tests on cubic samples of unidirectional DA 4518 carbon-epoxy prepreg. Four loading rates were considered and the results are summarized in Table 2.2. The results show a significant increase in longitudinal compressive modulus from the quasi-static conditions to high loading rates. Nevertheless, the modulus decreases with increasing strain rate for the dynamic tests. On the other hand, the longitudinal compressive strength increases steadily with increasing strain rates.

Bing and Sun [16] developed a methodology to extrapolate the longitudinal compressive strength and modulus from off-axis tests of unidirectional AS4/3501-6 carbon epoxy com-

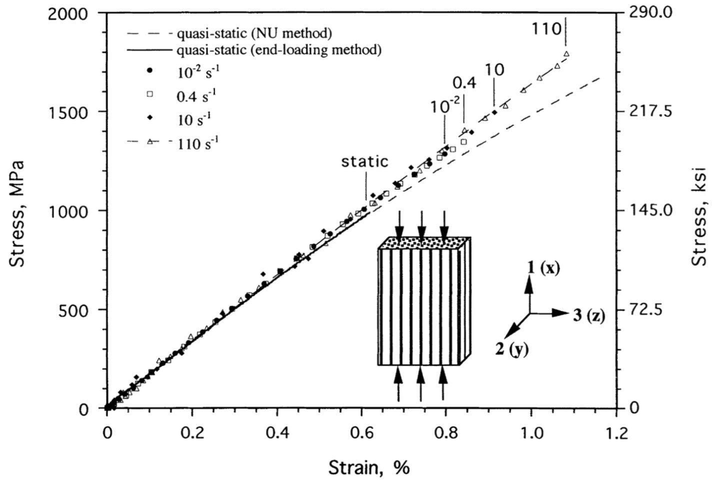

Figure 2.12: Longitudinal compressive stress-strain curves of UD carbon-epoxy at five strain rates [14]

Table 2.2: Longitudinal compression strength and stiffness of unidirectional carbon-epoxy composite at different strain rates [15]

Strain rate $[s^{-1}]$	Modulus [GPa]	Modulus increase over static value	Strength [MPa]	Strength increase over static value
QS	11.5	-	504	-
82	28.6	149%	541	7%
163	25.3	120%	593	18%
817	21.6	88%	637	26%

posites. From specimens loaded at angles of 5°, 11° and 15°, the authors predict an increase of 46% over the quasi-static value for the longitudinal compressive strength at a strain rate of 250 s^{-1}. From the same off-axis tests, Bing and Sun [16] also predict that the longitudinal compressive modulus is not affected by changes in loading rate.
Koerber and Camanho [17] also performed longitudinal compression tests on rectangular IM7-8552 carbon-epoxy specimens using a compression SHPB apparatus to reach strain rates up to 100 s^{-1}. Figure 2.13 shows a comparison between the stress-strain curves under quasi-static conditions and at moderate strain rate ($\dot{\varepsilon} \approx 100\ s^{-1}$). Koerber and Camanho [17] report a 40% increase in longitudinal compressive strength for the higher deformation rate tested, which is followed by a similar increase in failure strain, since there is no variation in compressive modulus.

The results obtained by Hsiao and Daniel [14], Bing and Sun [16], and Koerber and Camanho [17] are consistent with each other: with increasing strain rate, the longitudinal compressive strength increases significantly, but the modulus is not affected. These authors report different strength increases at identical strain rate values, which might be due to dissimilar fibre-matrix systems tested and different testing rigs used. Besides an increase in strength, Hosur et al. [15] also report a two-fold increase in compressive modulus, which is inconsistent with the observations of other authors. This increase in apparent modulus reported by Hosur et al. [15] may be explained by the lack of dynamic equilibrium in the initial elastic response.

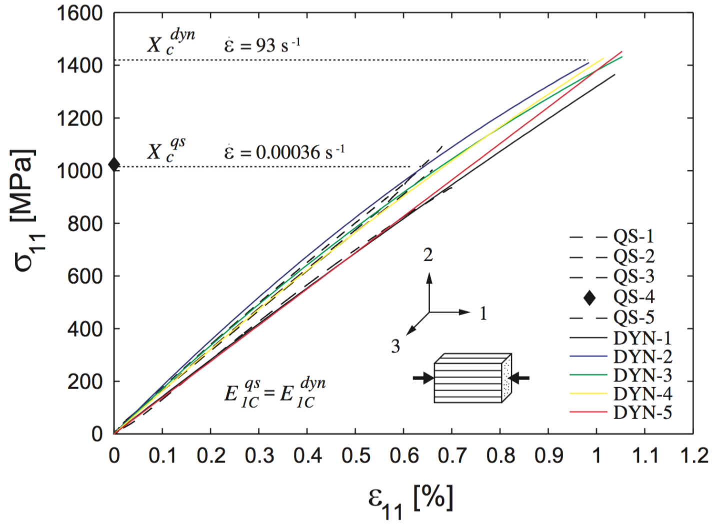

Figure 2.13: Longitudinal compressive stress-strain curves of carbon-epoxy laminates at quasi-static and moderate strain rates [17]

Comment on longitudinal compressive strength growth with increasing strain rate

Failure mechanisms of composites under compressive loads have been target of investigation over the past decades, mainly due to difficulties associated with the instantaneous and catastrophic compressive failures, leading to compressive strengths significantly lower than tensile strengths.

A simple model to determine the compressive strength of unidirectional carbon-epoxy laminates was proposed by Daniel et al. [18], which takes into account the initial fibre misalignment ϕ^0 and the matrix shear properties. The initial fibre misalignment in a unidirectional laminate (Figure 2.14 **(a)**) increases with an applied axial load σ_x by the value of the in-plane shear strain γ_{12} (Figure 2.14 **(b)**).

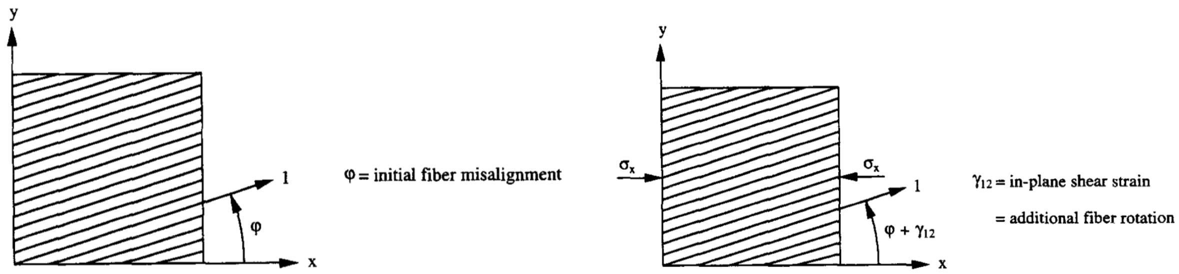

(a) before loading **(b)** after loading

Figure 2.14: Unidirectional laminate with initial fibre misalignment before and after compressive loading [18]

The stress components in the material axes are expressed by

$$\begin{cases} \sigma_1 = \sigma_x \cos^2(\phi^0 + \gamma_{12}) \\ \sigma_2 = \sigma_x \sin^2(\phi^0 + \gamma_{12}) \\ \tau_{12} = \sigma_x \sin(\phi^0 + \gamma_{12}) \cos(\phi^0 + \gamma_{12}) \end{cases} \tag{2.1}$$

which, assuming that both the initial fibre misalignment ϕ^0 and the shear strain γ_{12} are small angles, can be simplified into

$$\begin{cases} \sigma_1 \approx \sigma_x \\ \sigma_2 \approx 0 \\ \tau_{12} \approx \sigma_x(\phi^0 + \gamma_{12}) \end{cases} \tag{2.2}$$

and from the third line of equation (2.2) follows

$$\sigma_x \approx \frac{\tau_{12}}{\phi^0 + \gamma_{12}} \tag{2.3}$$

Knowing that the maximum of equation (2.3) is the longitudinal compressive strength, then the following condition must apply

$$\frac{\partial \sigma_x}{\partial \tau_{12}} = 0 \implies \frac{\partial}{\partial \tau_{12}}\Big(\frac{\tau_{12}}{\phi^0 + \gamma_{12}}\Big) = 0 \implies \frac{1}{\phi^0 + \gamma_{12}} \frac{\partial \tau_{12}}{\partial \gamma_{12}} - \frac{\tau_{12}}{(\phi^0 + \gamma_{12})^2} = 0 \tag{2.4}$$

which can be simplified into

$$\frac{\partial \tau_{12}}{\partial \gamma_{12}} = \frac{\tau_{12}}{\phi^0 + \gamma_{12}} \tag{2.5}$$

The solution of equation (2.5) is the point of the shear stress-strain curve - location $\tau_{12} = \tau^*$ and $\gamma_{12} = \gamma^*$ - in which the tangent to the shear response equals the slope $\tau^*/(\phi^0 + \gamma^*)$. Figure 2.15 shows a graphical representation of the solution for equation (2.5).

Given this, the longitudinal compressive strength of unidirectional composites with an initial fibre misalignment is obtained by simply replacing back into equation (2.3), resulting in:

$$(\sigma_x)_{max} = \frac{\tau^*}{\phi^0 + \gamma^*} \tag{2.6}$$

Budiansky and Fleck [19] presented a model that assumes an elastic-perfectly plastic matrix behaviour to predict the longitudinal compressive strength of unidirectional laminates:

$$(\sigma_x)_{max} = \frac{\tau_y \sqrt{1 + \left(\frac{\sigma_{\tau_y}}{\tau_y}\right)^2 \tan^2 \beta}}{\phi^0 + \gamma_y} \tag{2.7}$$

where τ_y is the in-plane shear yield stress, σ_{τ_y} represents the transverse yield stress, γ_y is the shear strain at yield and β is the kink band inclination angle in relation to the fibre initial direction. Assuming small values of β, equation (2.7) simplifies to:

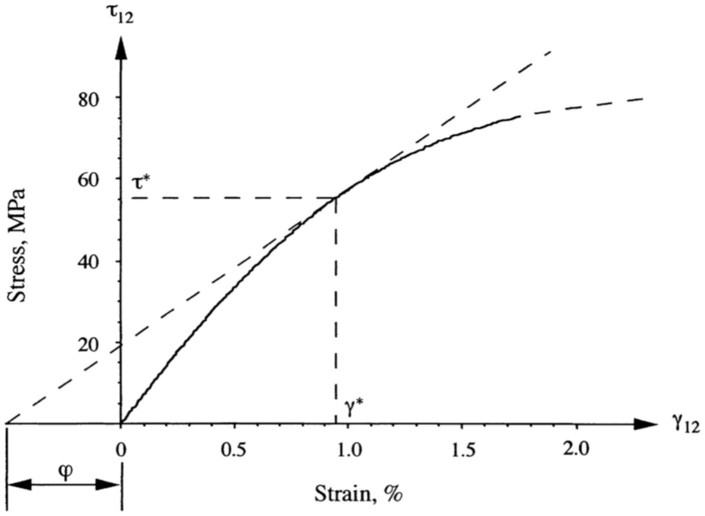

Figure 2.15: Typical shear stress-strain curve of an unidirectional laminate with graphical representation of equation (2.5) [14]

$$(\sigma_x)_{max} \approx \frac{\tau_y}{\phi^0 + \gamma_y} \tag{2.8}$$

which is a similar result to what was presented in equation (2.6) by Daniel et al. [18], except that (2.8) makes use of the yielding shear stress and shear strain of the laminate.

Either way, it is clear that the longitudinal compressive strength of FRP is intimately controlled by the laminate's shear behaviour. These models suggest that when the matrix reaches its yielding stress/strain, plastic deformation starts to take place and the matrix is no longer able to support the fibres, leading to an increase in fibre microbuckling and the consequent creation of kink bands.
Jumahat et al. [20] confirmed the effect of the shear stress-strain response on the strength of axially loaded unidirectional composites by studying the effect of matrix systems with different yielding properties. They concluded that the shear properties play a major role on the compressive strength of carbon fibre-reinforced polymers (CFRP) composites, since a stiffer matrix provides a better support to the fibres, leading to significant increases in compressive strength of CFRP composites.

Even though one would expect the longitudinal compressive properties of carbon-epoxy laminates to be strain rate insensitive, as the response in this loading direction is fibre dominated and it was previously shown section 2.1.1 that carbon fibres are not rate sensitive, the current section shows a clear increase in longitudinal compressive strength and failure strain.
The previously presented discussion provides an explanation for the mentioned strength growth, as it was shown that this property is highly related with the resin properties and the laminate shear response, which show significant increases with increasing strain rates, as shown previously in subsection 2.1.2 and later on in subsection 2.2.3, respectively.

Table 2.3: Transverse compression strength and stiffness of unidirectional carbon-epoxy composite at different strain rates [15]

Strain rate $[s^{-1}]$	Modulus [GPa]	Modulus increase over static value	Strength [MPa]	Strength increase over static value
QS	3.96	-	149	-
82	4.96	25%	150	0.7%
163	5.38	36%	170	14%
817	5.94	50%	186	25%

2.2.2.2 Transverse direction

When loading an unidirectional laminate in the transverse direction, its mechanical response is dominated by the matrix behaviour. Therefore, it is expected that any strain rate dependency in the transverse direction to be related with the matrix's strain rate dependent properties.
Hsiao et al. [21] performed compressive experiments on unidirectional IM6G/3501-6 carbon-epoxy laminates at strain rates varying from 10^{-4} to 1800 s^{-1} using three different testing set-ups: a servohydraulic testing machine for the low rates (below 10 s^{-1}), a drop tower apparatus for the intermediate rates (from 10 to 300 s^{-1}) and a compression SHPB for the high strain rates (above 500 s^{-1}). Figure 2.16 presents the stress-strain curves of the laminate response when loaded compressively in the transverse direction at different strain rates.
At high strain rates, the transverse compressive strength and modulus increase by 94% and 37% over the quasi-static values, respectively. On the other hand, the ultimate strain remains constant over the tested range of loading rates.

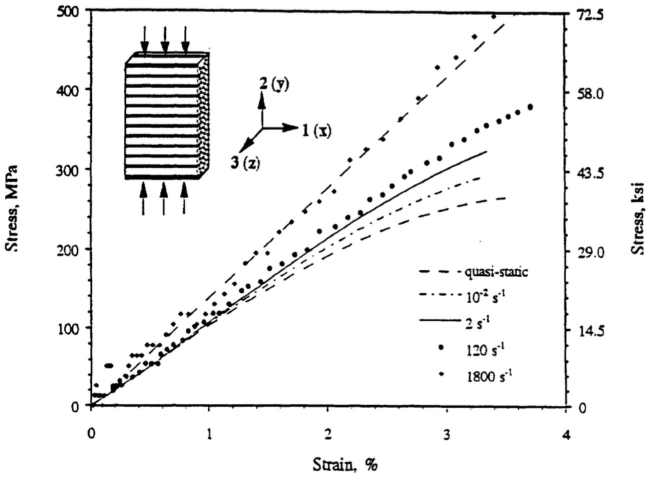

Figure 2.16: Transverse compressive stress-strain curves of UD carbon-epoxy at five strain rates [21]

As mentioned in subsection 2.2.2.1, Hosur et al. [15] performed compression tests on unidirectional cubic carbon-epoxy laminates using a SHPB testing set-up. Their results for the laminate properties when loaded in the transverse direction are shown in Table 2.3.

Similar results were also obtained by Koerber et al. [22], who performed transverse compression tests on unidirectional IM7-8552 carbon-epoxy laminates at quasi-static speeds ($\dot{\varepsilon} \approx 4 \times 10^{-4}\ s^{-1}$) and high speeds ($\dot{\varepsilon} \approx 270\ s^{-1}$). The stress-strain curves obtained at these two loading rates are presented in Figure 2.17. From quasi-static to dynamic testing conditions, an increase of transverse compressive strength from 255 to 371 MPa was found, which represents a growth of 45%. Moreover, the transverse compression modulus and the yield stress increased by 12% and 83%, respectively.

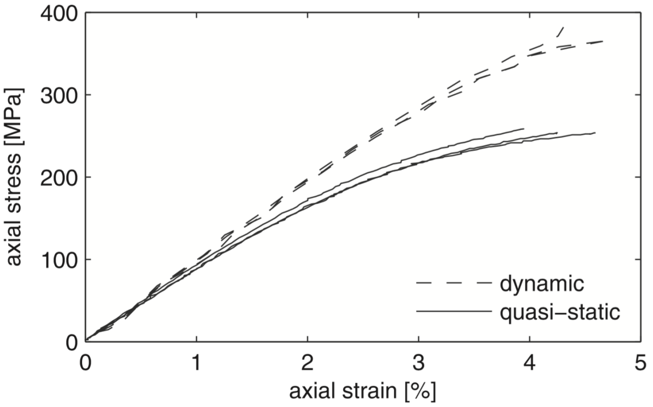

Figure 2.17: Quasi-static and dynamic transverse compressive stress-strain curves of IM7-8552 carbon-epoxy laminates [22]

The results presented by Hsiao et al. [21] and Koerber et al. [22] are in very good agreement with each other. For increasing strain rates, the transverse stress-strain curves stiffen, leading to significant increases in strength and, to a smaller extend, increases in compressive modulus. The different relative increases, from quasi-static to dynamic testing, reported by these two studies might be related with the different resin systems used.

Hsiao et al. [21] suggest two possible explanations for the increase achieved in transverse compressive properties. The first being the viscoelastic behaviour of the resin, which is the dominant constituent in transverse direction. The second reason is related to the time-dependent nature of the damage accumulating process. At higher rates, the damage in the matrix does not have enough time to develop and propagate, which means that the matrix damage is limited to the location where it is initiated. This effect is a reasonable explanation for the stiffer stress-strain curves at higher loading rates.

2.2.3 Shear

As is the case with the transverse direction, the shear mechanical response of FRP is predominately matrix-dominated. Therefore, it is likely that FRP behave differently when loaded in shear with distinct strain rates, just like it was shown in subsection 2.1.2.3 for the neat resin specimens.

For in-plane shear testing of laminates, there are mainly two types of methodologies that are commonly used:

1. A ±45° layup specimens tested in tension, according to ASTM D3518 [23], or in compression.

2. Off-axis compression of unidirectional specimens.

A distinction will be made when analysing shear response of laminates between the two test methods.

±45° specimens tested in tension and compression

Staab and Gilat [24], and Shokrieh and Omidi [25] performed quasi-static and dynamic tensile tests on [±45°] layup glass-epoxy specimens using a tensile SHPB and a servo-hydraulic testing rigs, respectively.
Staab and Gilat [24] reached strain rates of 1000 s^{-1} and found an increase of 43% in shear strength over the quasi-static tests. The shear modulus did not change significantly with increasing strain rate. The obtained stress-strain curves are shown in Figure 2.18 **(a)**.
Shokrieh and Omidi [25] report a maximum strain rate of 100 s^{-1}, at which a 37% increase over the quasi-static value of shear strength was found. Furthermore, the shear modulus reduced slightly (−12%) for the higher loading rates. The shear stress-strain curves for different stroke rates are shown in Figure 2.18 **(b)**.
When comparing the two graphs shown in Figure 2.18, it is important to note that **(a)** is an axial stress-strain curve, while **(b)** is plotted in terms of shear properties. Furthermore, results for a shear strain above 5% should be treated with care, since critical fibre re-orientation has occurred.

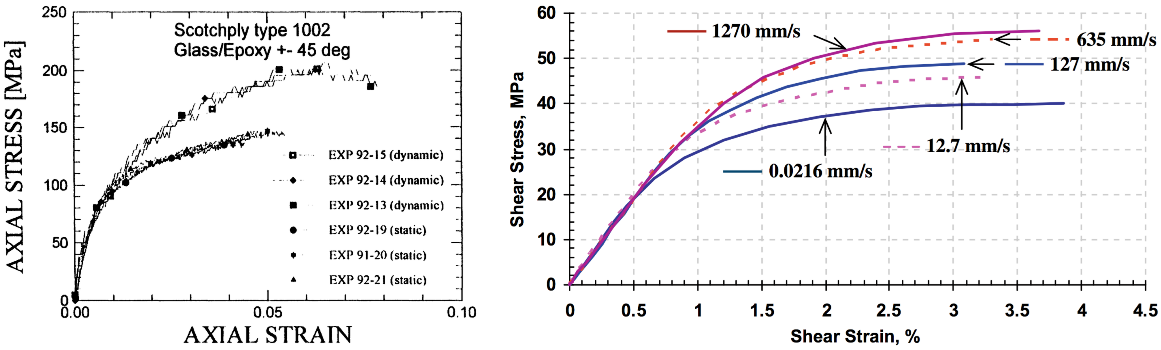

(a) Scotchply 1002. $\dot{\varepsilon}_{max} = 1000\ s^{-1}$ [24]

(b) E-glass/ML-506. $\dot{\varepsilon}_{max} = 100\ s^{-1}$ [25]

Figure 2.18: Stress-strain curves of glass-epoxy [±45°] layup specimens at different strain rates

Similar experiments were performed by Gilat et al. [5] and by Taniguchi et al. [12], but using carbon-epoxy specimens. The experiments of both studies were performed using a tensile SHPB and the former achieved an axial strain rate of 600 s^{-1}, while the latter was limited to 100 s^{-1}.
In both cases, the shear strength at the higher strain rates increased by 55 to 60% of the value obtained at quasi-static testing speeds. Furthermore, both studies mention an increase in shear modulus with increasing strain rate, but do not specify the absolute or relative increase. On the other hand, different conclusions are reached for the shear strain at failure. Gilat et al. [5] found no effect of the loading rate on the failure strain, while Taniguchi et al. [12] mention a severe reduction (from 5% to less than 2%) in shear strain at failure between static and dynamic tests. Representative stress-strain curves of both studies are shown in Figure 2.19.

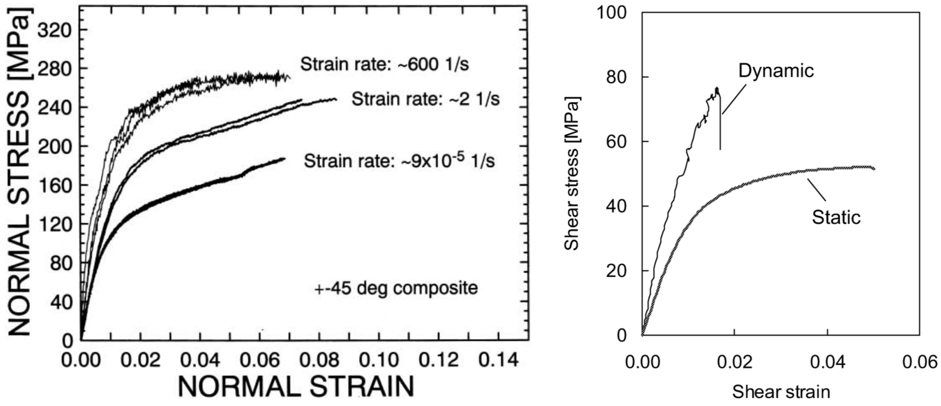

(a) IM7/977-2. $\dot{\varepsilon}_{max} = 600\ s^{-1}$ [5]

(b) T700S/2500. $\dot{\varepsilon}_{max} = 100\ s^{-1}$ [12]

Figure 2.19: Stress-strain curves of carbon-epoxy [±45°] layup specimens at different strain rates

In a recent study by Cui et al. [26], [±45°] specimens made of IM7/8552 carbon-epoxy prepreg were tested both in tension and compression at quasi-static and dynamic conditions, using a screw driven testing machine and a tension/compression SHPB, respectively. A nonlinear shear model was also developed to take into account fibre rotation, thus fibre orientation is updated for large deformation strains. Figure 2.20 shows the shear stress-strain curves obtained for tension and compression tests, at both static and dynamic testing.
For both loading cases, the shear strength increased by approximately 60% between quasi-static and dynamic testing. Furthermore, the material responds linearly up to larger shear strains when loaded faster. The yielding stress and strain are significantly greater at dynamic loading rates.

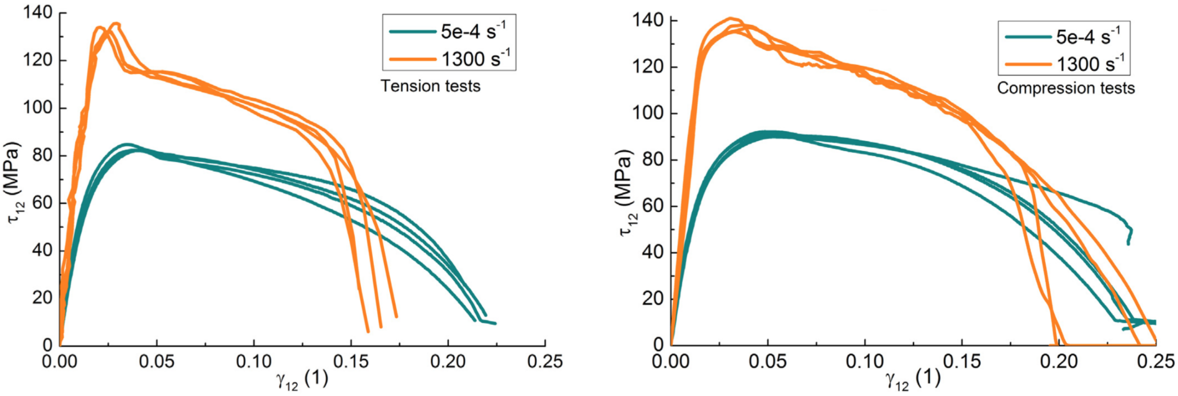

(a) tension tests

(b) compression tests

Figure 2.20: Shear stress-strain curves of carbon-epoxy laminates, corrected for fibre rotation [26]

Off-axis unidirectional specimens tested in compression

The second methodology to obtain the in-plane shear properties is by testing unidirectional laminates with a compressive load applied with an angle in relation to the fibres.
Hsiao et al. [21] performed quasi-static and dynamic compressive tests with 30° and 45° off-axis compressive loads on unidirectional specimens made with IM6G/3501-6 prepreg material. Small, moderate and high strain rates were obtained using a servo-hydraulic testing machine, a drop-tower apparatus and a compression SHPB, respectively. The resulting shear stress-strain curves are presented in Figure 2.21 **(a)**.
In a similar fashion, Koerber et al. [22] performed quasi-static and dynamic tests (up to a strain rate of 350 s^{-1}) on unidirectional IM7-8552 carbon-epoxy laminates with 15°, 30°, 45° and 60° off-axis compressive load. The obtained shear stress-strain curves are shown in Figure 2.21 **(b)**.
Both studies report increases of shear strength and shear modulus for higher loading rates. Hsiao et al. [21] mention increases of 50% and 18% over the quasi-static values for the shear strength and modulus of the 45° off-axis tests, respectively, while Koerber et al. [22] obtained growths of 42% and 25% for the same properties. In both cases, the shear strain at failure decreases with increasing strain rate.

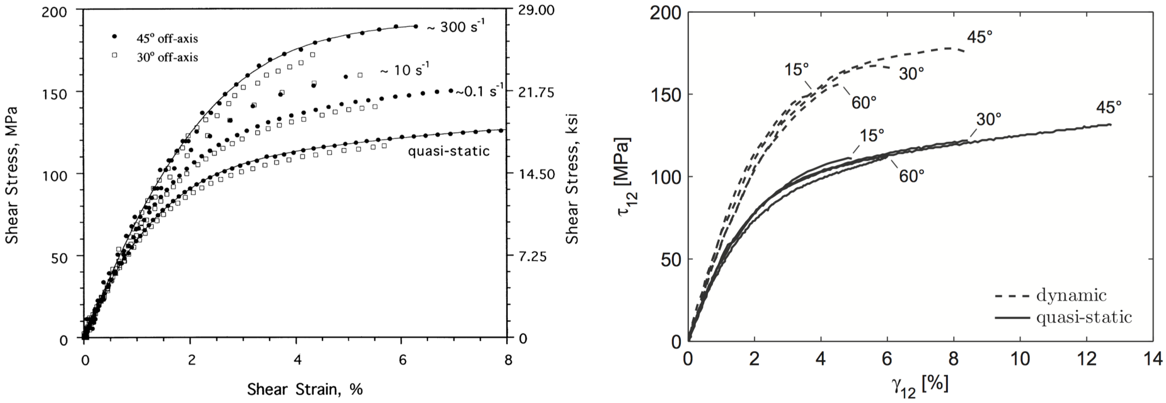

(a) IM6G/3501-6 prepreg [21]

(b) IM7-8552 prepreg [22]

Figure 2.21: Shear stress-strain curve of carbon-epoxy unidirectional specimens at different loading directions and rates

Tsai and Sun [27] performed similar compressive off-axis tests on S2/8552 glass-epoxy laminates using a compression SHPB to reach high strain rates. Note that the resin system is exactly the same as the one used by Koerber et al. [22], who reported an increase of 42% of in-plane shear strength. Over the same deformation rate range, Tsai and Sun [27] mention an increase of 46% in shear strength. Furthermore, Koerber et al. [22] obtained a reduction of 28.4% in shear strain at failure for the dynamic tests, while Tsai and Sun [27] report a reduction of 26.2% of this property over the same strain rate range.
The results presented by these two studies, which use the same epoxy system and different fibre types, are in very good agreement, which indicates that the strain rate dependency of the in-plane shear properties is a matrix-dominated phenomenon.

2.3 Neat resin vs. composite strain rate effect

In the previous sections 2.1 and 2.2, the effect of the strain rate on the mechanical response of the constituents and fibre-reinforced composites was presented, respectively. Even though the presented studies provide a good overview of the strain rate effect, it is not straightforward to directly compare the results between different authors, given not only the large variety of resin and fibres used, but also the different testing rigs. An improved methodology to compare the results of different authors was achieved by normalising the mechanical properties with the reported quasi-static values.

In the current section, a comparison between the strain rate effect on pure resin and fibre-reinforced epoxy specimens is given. This comparison is presented for the properties which are matrix-dominated and show a dependency on the strain rate:

- Compression strength of neat epoxy vs. transverse compression strength of FRP.
- Shear strength of neat epoxy vs. shear strength of FRP.
- Compression modulus of neat epoxy vs. transverse compression modulus of FRP.
- Shear modulus of neat epoxy vs. shear modulus of FRP.
- Compression yield stress of neat epoxy vs. transverse compression yield stress of FRP.
- Shear yield stress of neat epoxy vs. shear yield stress of FRP.

Figure 2.22 **(a)** and **(b)** present the normalised compression and shear strength of both pure and fibre-reinforced epoxy specimens. For both cases, it is clear that the increase in strength of pure epoxy specimens with increasing strain rate is higher than the strength increase of FRP. Nonetheless, the trend is indisputable, as all authors report an increasing strength for higher strain rates.

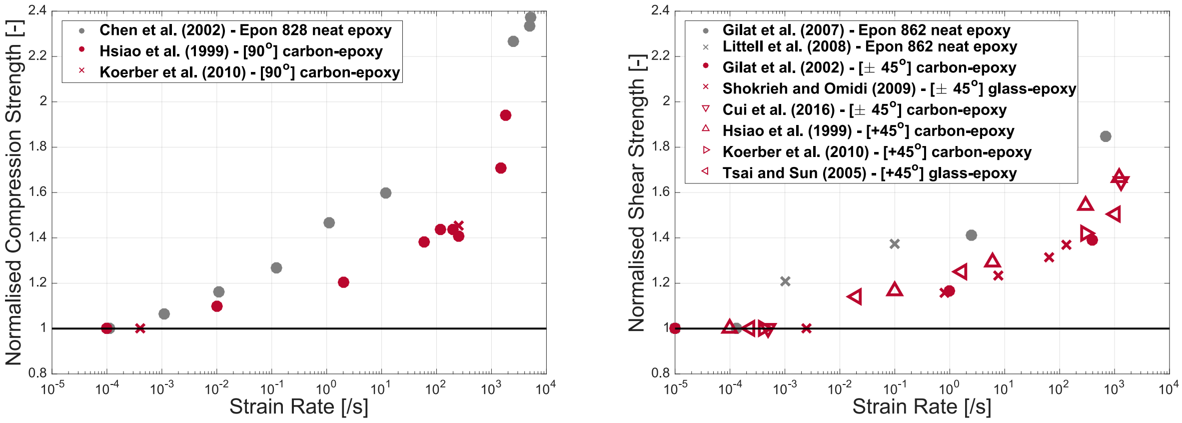

(a) Neat epoxy and FRP transverse compression strength

(b) Neat epoxy and FRP shear strength

Figure 2.22: Comparison between the normalised strength of neat epoxy and fibre-reinforced specimens at different strain rates.

A similar analysis is shown in Figure 2.23, but for the moduli. **(a)** compares the compression modulus of neat epoxy specimens with the transverse compression modulus of FRP, while **(b)** depicts the shear modulus of both neat epoxy and FRP specimens. With increasing strain rate, an increasing trend of moduli is apparent, even though the amount of available data is less than for the strength case.

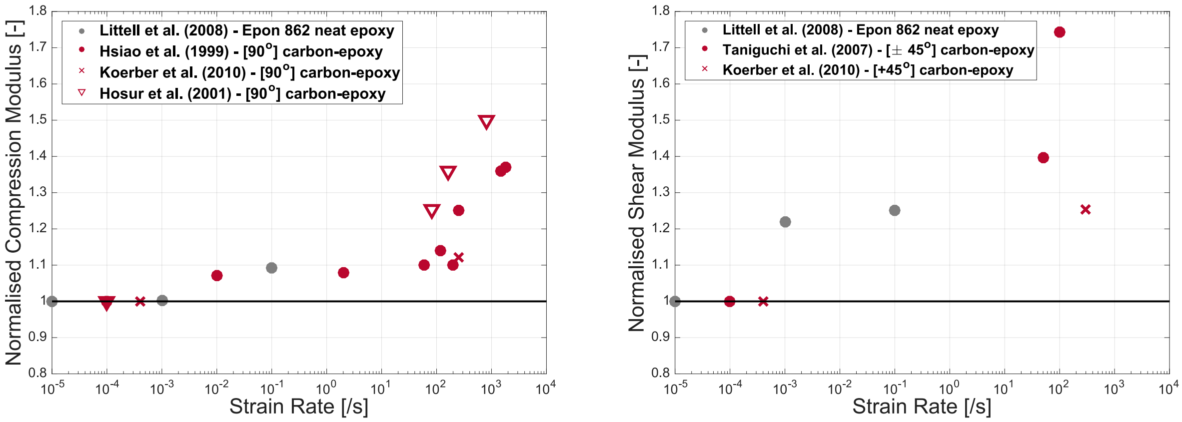

(a) Neat epoxy and FRP transverse compression moduli

(b) Neat epoxy and FRP shear moduli

Figure 2.23: Comparison between the normalised moduli of neat epoxy and fibre-reinforced specimens at different strain rates.

Regarding the yield stress, Figure 2.24 **(a)** presents the normalised values for neat epoxy specimens and for transversely loaded FRP, both under compression, while **(b)** is related with the shear yield stress. The amount of data referring to the yield stress is very scarce and only some authors report this property in tables. Nonetheless, as presented in the stress-strain curves in subsections 2.2.2.2 and 2.2.3, the yield stress of transverse and shear loaded FRP clearly increases with increasing strain rate. For higher loading rates, the curves become stiffer and the range with linear mechanical response is extended.

Overall, it is clear that the strain rate dependency of matrix-dominated properties of CFRPs are related with changes in mechanical response of the matrix, since carbon fibres are not rate dependent. Nevertheless, and possibly more importantly, the properties of longitudinally compression loaded FRPs also improve with increasing strain rate, and an explanation related with the improved support provided by the resin to the fibres was presented in subsection 2.2.2.1.

2.4 Specimen geometry effects on compression testing of FRP

As there is no adopted standard for dynamic compression testing of FRP, it is important to understand what is the influence of each geometrical factor of typical rectangular specimens (thickness, width and gauge length) on the measured compression properties. Therefore, this section will go through these different factors and present the expected consequences when changing the specimen geometry.

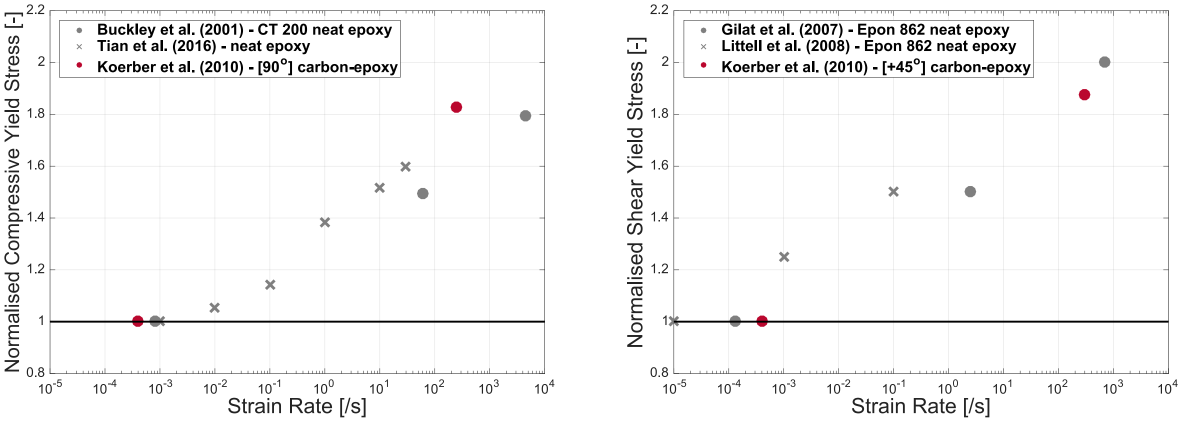

(a) Neat epoxy and FRP transverse compression yield stress

(b) Neat epoxy and FRP shear yield stress

Figure 2.24: Comparison between the normalised yield stress of neat epoxy and fibre-reinforced specimens at different strain rates.

2.4.1 Thickness

The influence of the thickness on the measured compression strength and modulus of unidirectional FRP was investigated by Camponeschi [28] when he was designing a new fixture to allow testing of thick composites. Specimens were manufactured using AS4/3501-6 carbon-epoxy and S2/3501-6 glass-epoxy prepregs with 48, 96 and 192 plies, corresponding to thicknesses of 6.4, 12.7 and 25.4 mm, respectively. The results showed that the compressive modulus of both laminates did not change significantly with varying specimen thickness. However, for both laminates, the compressive strength and the failure strain dropped by 25% and 20%, respectively, for an increase in specimen thickness from 6.4 to 12.7 mm.

Hsiao et al. [29] also noted the effect of the composite specimen thickness when developing a fixture that inserts the load both through the tabs (by shear forces) and by end loading. The tested specimens were made of unidirectional IM6G/3501-6 carbon-epoxy prepreg and were 16, 48 and 72 plies thick. From the thinnest to the thickest specimens, Hsiao et al. [29] found an increase of 5% in measured compression modulus, and decreases of 6% and 13% on the strength and failure strain, respectively. A reasoning for the decrease in compression strength and failure strain with increasing thickness might be related with the increasing fraction of the load that is introduced at the specimen end. Hsiao et al. [29] mention that for the specimens with 48 plies, 20 to 25% of the load is introduced by the tabs (via shear), while for the 72 plies thick specimen this fraction drops to 10 to 15%. The higher load introduced at the specimen end for the thicker composite leads to specimen end-crush, causing premature failure and, thus, a reduction in strength.

In more recent studies, Lee and Soutis [30, 31] studied the effect of several geometrical factors on the measured compression properties of carbon-epoxy laminates, both with unidirectional and multidirectional layups. Figure 2.25 shows the compression stress-strain curves of unidirectional IM7/8552 carbon-epoxy specimens with 2, 4 and 8 mm of thickness. Overall, they found decreases of 35 to 45% in compression strength and reductions up to 50% in failure strain, between 2 and 8 mm thick specimens.

Lee and Soutis [30, 31] mention several plausible explanations for the decrease in compression

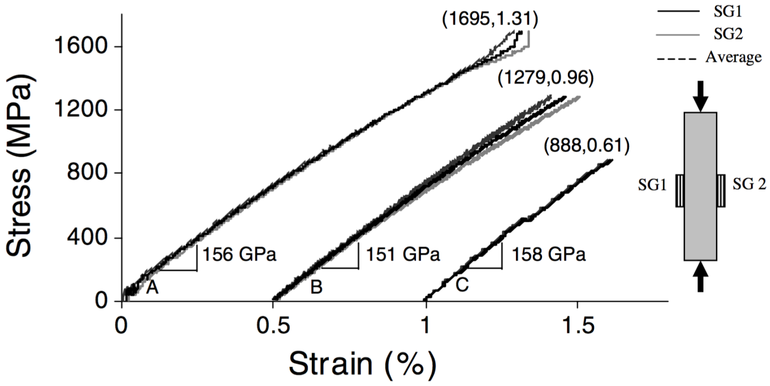

Figure 2.25: Compression stress-strain curves of unidirectional carbon epoxy specimens 2 mm (A), 4 mm (B) and 8 mm (C) thick [30]

strength and failure strain with increasing specimen thickness. First of all, thicker laminates tend to have lower fibre volume fractions due to manufacturing limitations, as the void content is usually larger in thicker specimens. Furthermore, the manufacturing process of thicker laminates also introduces higher values of fibre waviness. The combination of these effects greatly affects the triggering of fibre microbuckling, causing the laminate to fail under lower strain values.

2.4.2 Width

The effect of the specimen width during off-axis compression testing of carbon-epoxy laminates was studied by Bing and Sun [32]. AS4/3501-6 unidirectional prepreg specimens were cut with widths of 4, 7, 14 and 21 mm and tested under compression with off-axis loads of 5°, 10° and 15°. The obtained compression strength as function of the specimen width is presented in Figure 2.26.

A significant decrease in compression strength with increasing specimen width is clearly visible for the three off-axis angles tests. Furthermore, the reduction is higher for the specimens with lower off-axis angle. A possible reason for this reduction is the presence of defects. The wider the specimen, the larger is the chance of manufacturing defects being present. This effect is more critical for specimens tested with a smaller off-axis angle because as the loads gets aligned with the fibres, fibre microbuckling gets more significant and defects tend to trigger this failure mode.

Lee and Soutis [30] also tested the effect of increasing specimen volume on the compression strength of unidirectional carbon-epoxy laminates. The specimen gauge length, width and thickness were raised by factors of 2 and 4 over the standard 10 x 10 x 2 mm (gauge length x width x thickness) specimen. As reported earlier, specimens with more volume tend to fail at lower strain levels, leading to decreased compression strengths. The manufacturing defects present in specimens with more volume act as a trigger to the failure mechanisms, causing the entire specimen to fail earlier than its intrinsic compression stress/strain. Nonetheless, Lee and Soutis [30] also mention a lower limit for the specimen width: it should be at least five times the specimen thickness, to avoid the effect of free edges and reach an uniaxial state of stress.

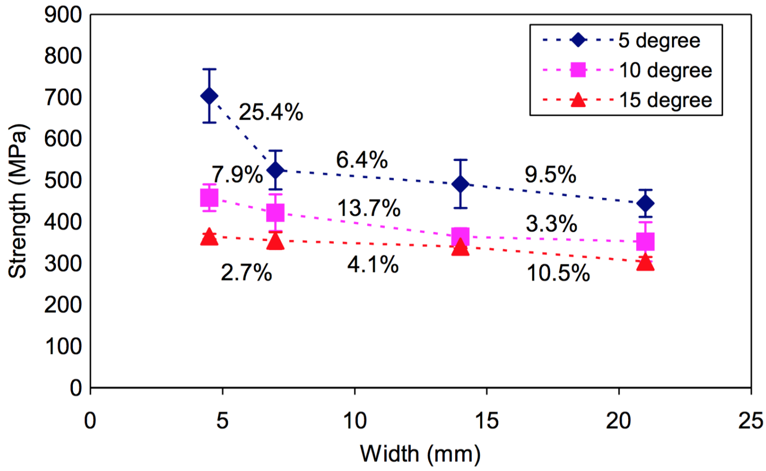

Figure 2.26: Effect of specimen width on the compression strength of off-axis unidirectional carbon-epoxy laminates [32]

2.4.3 Gauge Length

During compression testing of FRP, it is necessary to prevent the phenomenon of Euler column buckling. Therefore, the maximum gauge length of the specimen must be determined based on a buckling analysis, assuming a rectangular cross-section. Whitney and Pagano [33] developed a model that includes the effects of the end support conditions and the shear deflection effects on heterogeneous anisotropic plates. According to their model, to have compressive failure occurring before any Euler instability, the subsequent condition must apply:

$$(\sigma_x)_{max} \leqslant \frac{0.67K\pi^2(E_1 I)}{AL^2} \tag{2.9}$$

where $(\sigma_x)_{max}$ is the material ultimate stress, K is a constant related with the end support conditions, E_1 and I are the longitudinal modulus and second moment of area, respectively, A is the rectangular cross-section area and L is the specimen gauge length, in this case. Equation (2.9) can be rewritten as a condition for the maximum allowed gauge length L:

$$L_{max} \leqslant \pi t \sqrt{\frac{0.67KE_1}{12(\sigma_x)_{max}}} \tag{2.10}$$

On the other hand, the gauge length should be long enough to allow not only for placement of strain gauges if necessary, but also to allow stress decay to uniaxial compression, given the concentration caused by the grips end [34].

This stress concentration is unavoidable during compression testing because there always is a stiffness mismatch at the end of the loading tabs. However, its magnitude is influenced by several testing factors, such as the type of load introduction of the fixture, the type of material used for the loading tabs and its geometry (tapered or untapered).

Several testing fixtures can be used for compression testing of FRP and the main difference has to do with the load introduction method. End-loading fixtures introduce the entirety of the load at the specimen's ends, while the tabs might be used to provide some lateral support, thus leading to very low stress concentration factors at the tab end. The main issue with end-loading fixtures is related with crushing at the specimen's ends, causing non-acceptable failure types. Other kind of fixtures introduce the load only through shear, which results in high stress concentration factors at the grips end. A third type of fixture combines end-loading with shear-loading, leading to intermediate stress concentration factors at the grips end. [35]

Another factor that affects the stress concentration factor and, thus, the reached compression strength is the type of material used for the loading tabs and its geometry. Tabs made with a more compliant material, i.e. softer, lead to lower stress concentrations, which is why glass fibre-reinforced polymer (GFRP) tabs should be used instead of steel tabs [36]. Regarding the geometry of the tabs, the most important factor is the taper angle at the grips end. Specimens equipped with straight (untapered) tabs have a sudden stiffness mismatch at the tabs end, leading to high stress concentration factors. On the other hand, tabs with a taper angle of 20° can lead to reductions in stress concentration up to 50%, when compared to untapered tabs [36]. Nonetheless, an excessive decrease of the tab taper angle leads to an increase in effective gauge length, which can cause global buckling of the specimen.

2.4.3.1 Bending Factor

Even though the occurrence of Euler buckling during the compression test can be prevented by choosing the appropriate specimen thickness and gauge length, there is always an induced bending on the specimen. This bending can be related with imperfections generated during the manufacturing of the specimen or, most commonly, misalignments of the testing fixture. To check for the occurrence of excessive bending stresses during testing, ASTM D6641 [37] suggest the installation of back-to-back strain gauges on several specimens. The strain signals coming from the two strain gauges should be used to determine the bending factor:

$$B_y = \text{bending factor} = \frac{\varepsilon_{\text{front}} - \varepsilon_{\text{back}}}{\varepsilon_{\text{front}} + \varepsilon_{\text{back}}} \times 100 \tag{2.11}$$

which should be less than 10%, for validation of the good manufacturing of the specimens and alignment of the fixture.

2.5 Finite element simulation

Across several areas of the engineering field, especially the automotive and the aerospace industry, a variety of Finite Element software packages are widely available and extensively used to perform numerical simulations of not only structural components, but also entire assembled structures. The execution of these numerical simulations is extremely important, since they allow for a quick evaluation of the suitability of a certain structural design to a given load case, without actually having to commit an excessive amount of time and money in the manufacturing of several design iterations for experimental testing. Nonetheless, it is of the highest importance to make sure that the physical behaviour of the material is being

properly simulated during the numerical runs. This is especially hard for FRP, since these kind of materials fail through a wide variety and combination of mechanisms. Therefore, it is important to have a numerical model which is able to reproduce the complex physics of the different phenomena occurring during a crushing event of FRP [38]. On the other hand, the numerical models should be simple enough to be used in a practical analysis, and numerically robust and inexpensive.
The current section presents a short review and comparison between studies with and without strain rate dependent updated material cards for FRP. The focus is on the correlation between experimental and simulation results obtained using static or dynamic material properties, using commercially available FE software, especially Pam-Crash®.

Morozov and Thomson [39] simulated the response of a thin-walled car structural component made of glass fabric reinforced epoxy, making use of the Pam-Crash® analysis tool.
Firstly, uniaxial tension and compression tests were performed with typical specimens to characterise and implement the material properties and numerically predict the elementary ply behaviour. Very good agreement between the unixial experimental tests and the material response (stress-strain curves) was achieved during the material calibration phase.
Then, the calibrated material behaviour was used to simulate a crash event on a structural part - a compartment typically used to store a spare wheel. The real demonstrator was manufactured and tested under a crash event at 150 mm/s. The experimental results were compared with the simulation in a force-displacement plot, as shown in Figure 2.27.
Even though the authors mention that the agreement between the experimental and the simulation curves is rather good, the simulation curve clearly under predicts the experimental data. A possibility for this under prediction might be related with the strain rate dependent properties. The authors performed a calibration and validation of the simulation material card using data resulting from quasi-static experimental tests. During crash of the demonstrator, the material is subjected to high strain rates, which, as seen in previous sections, results in an overall increase of the mechanical properties of the fibre-reinforced polymer.

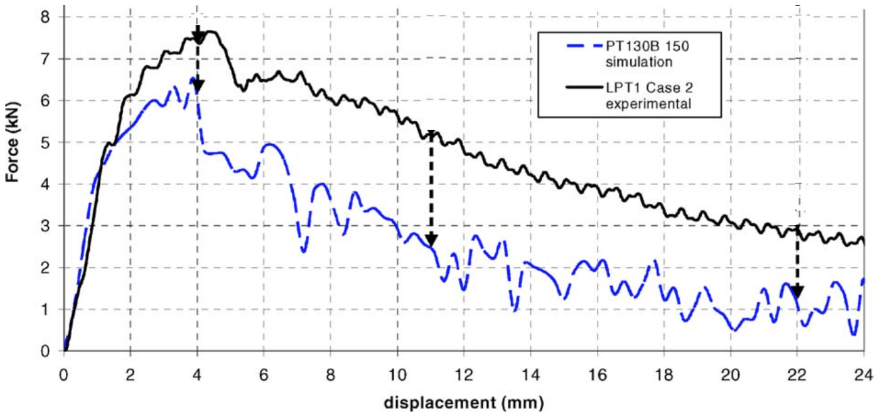

Figure 2.27: Force-displacement comparison of experimental and simulation analysis of a crash impact on a car structural component [39]

In the first publication of a two-part study, McCarthy et al. [40] present the approach used to model a glass-based Fibre Metal Laminate (FML) material card for the software Pam-Crash®. This material model includes the complex strain rate dependent mechanical properties exhib-

ited by these materials and an excellent agreement was achieved between experimental and simulation material behaviour.
In the second publication, McCarthy et al. [41] present the results of a bird strike on an aircraft wing leading edge, both experimental and numerical. The leading edge was manufactured with the same FML as modelled in part one [40] and was impacted by a bird at a speed of 129 m/s. Figure 2.28 shows a comparison of the experimental and numerical force time-history plots obtained at different locations of the testing fixture. Given the high complexity of the problem, the developed Pam-Crash® model shows “excellent agreement with the experiments" [41]. Furthermore, the loads transferred to the supporting structure and the leading edge deformed shape are very well predicted by the numerical simulation, when compared with the experimental results.

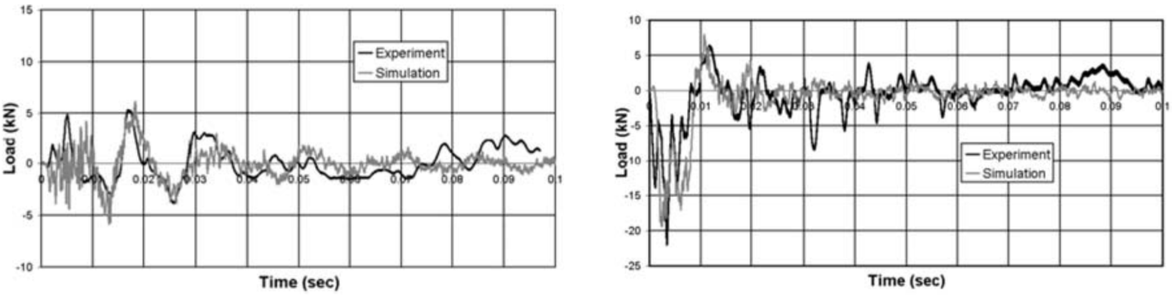

(a) X-direction **(b)** Z-direction

Figure 2.28: Experimental and numerical force time-history plots of a bird impact on a FML wing leading edge [41].

The different obtained results between the two studies summarized previously [39, 40] are a good example of the importance of having strain rate dependent properties implemented in the material cards when simulating crash events. Morozov and Thomson [39] used quasi-static material data and the resulting simulation under predicted the experimental results. On the other hand, McCarthy et al. [40, 41] achieved a better agreement between experimental and simulation results, not only, but also because their FML material card included strain rate dependent properties.

2.6 Thesis objectives and research questions

The main work of this thesis was performed with the support and cooperation of Audi AG. In Audi’s full vehicle crash simulations, FRP are modelled using quasi-static data. However, this leads to a high degree of conservatism, as structures are over-designed due to improved properties at higher loading rates.
The main goal is to develop and test a methodology to be implemented at Audi to determine the strain rate dependent compressive properties of FRP. Then, these properties shall be determined for a carbon-epoxy laminate and implemented in the FE software used at the company (Pam-Crash®). Verification tests will be performed to confirm if there is good agreement between experimental and simulation results at different loading rates. Finally, a structural component widely used at the company shall be axially loaded at different rates in

order to validate the strain rate dependent response, both experimentally and numerically. Therefore, the research questions to be answered during this thesis can be summarized as:

1. As there is no specimen geometry standard for dynamic testing, is there any influence of the geometrical factors on the measured properties of carbon-epoxy laminates?
    - How much do the measured compressive properties change with different specimen thickness, width and gauge length?
    - What should be the ideal specimen geometry to be used for dynamic testing of fibre-reinforced polymers?
2. Is there any noticeable change in the compressive properties of carbon-epoxy laminates at different loading rates?
    - Can the strain rate dependent properties be described through empirical equations and implemented in the Pam-Crash® material card?
    - How does the mechanical response of the laminate correlate between experimental and simulations?
    - Is it possible to numerically predict the behaviour of different laminate layups at varying strain rates correctly?
3. Is the strain rate dependency noticed on rectangular specimens also observable on more complex structural components?
    - Does the maximum load of a structural component change with varying crashing speeds or is this effect only observable in small specimens?
    - Does the layup of the laminate have an influence on the strain rate dependency? How do quasi-isotropic (QI) layups behave at different loading rates?

The first research question is directly related with the first phase of this thesis project. The objective is to find the optimal specimen geometry that should be used for dynamic compression tests of FRP. As there are no standards for dynamic tests and the compression fixture was specifically designed to be used with Audi's high-speed servo-hydraulic testing machine, the ideal specimen geometry must be found.

The second research question is connected with the dynamic tests to be performed at different speeds. It also includes the determination of the strain rate dependent properties and their implementation in the FE software.

The third and final main research question has to do with the applicability of this work on real structural components used in Audi's vehicles. The goal here is to study if the strain rate dependency achieved on simple specimens is also replicable on more complex components with quasi-isotropic layups. This is fundamental to determine if the work developed for this thesis can be applied in the full body crash simulations of Audi's car development process.

2.6.1 Thesis Motivation

As mentioned throughout the presented literature review, there is no established standard for dynamic compression testing of composite materials, even though there are multiple methods. Depending on the desired strain rate range, several testing rigs can be used, such as screw-driven or universal testing machines for quasi-static tests, drop-tower and servo-hydraulic for moderate loading rates, and SHPB rigs for very high strain rates. The employment of these different testing methodologies to reach a particular strain rate range means that comparing the results between static and dynamic conditions is not straightforward, since the testing equipment has an influence on the measured material properties. Furthermore, the vast majority of the presented studies do not quantify the influence of the specimen geometry adopted on the obtained material behaviour, and most authors that use two or more testing rigs, use dissimilar specimen geometries without taking into account the effect that this has on the mechanical properties being compared.

In the current work, a single testing methodology is used to cover a vast range of strain rates. This means that results obtained at highly dissimilar loading rates can be compared directly, as the influence of the testing configuration and specimen geometry is kept constant throughout the entire strain rate range. Additionally, a study on the influence of each geometrical aspect of the specimen is performed in order to quantify the effect and optimize each geometrical factor, to make sure that its influence on the obtained material behaviour is minimal.
As the goal is to reach loading rates typically observed during a crash event of a car, the top limit of the strain rate range relevant for this work is approximately 100 to 200 s^{-1} [42]. The SHPB testing apparatus, which is the commonly used method for dynamic testing, is suitable for strain rates in the range of 100 to several thousands s^{-1} [43, 44]. Furthermore, the SHPB has several limitations associated with measurements obtained at low strains (below 1% strain) due to the wave propagation mechanism through the bars, from which the specimen strain and strain rate are indirectly determined [45, 46]. Additionally, the lack of dynamic equilibrium during a large portion of a SHPB test leads to issues when determining the initial modulus of the material being tested.
For these reasons, the current work uses a highly versatile servo-hydraulic testing machine, with which strain rates in the range of 10^{-5} to 200 s^{-1} are obtainable. Moreover, as opposed to the case of indirect strain measurements that are commonly used in SHPB experiments, the current work makes use of a non-contact optical technique which directly measures the specimen deformation field.

An additional motive for the current work has to do with the connection between dynamic tests performed on typical material coupons and on structural components. In the vast majority of the studies presented in the current chapter, the authors either performed experimental quasi-static and dynamic tests on coupons, or only performed dynamic tests using structural components. Adding this to the fact that the strain rate dependent behaviour is highly dependent on the combination of fibres and resin system chosen, it becomes difficult to create a connection between coupon and structure behaviour, to verify and compare how the strain rate dependent properties evolve from simple geometries (coupon-type) to more complex shapes.
The present work includes compression tests not only with material coupons of different orien-

tations subjected to a wide range of strain rates to accurately predict the material behaviour, but also crash tests on a generic structural component widely used on vehicles, also under several impact speeds. Both the tests on coupons and structural component specimens are performed under identical conditions, i.e. same material system (fibre and resin), same testing machine and very similar testing fixtures, which will help to develop a 'bridge' between dynamic behaviour of material coupons and structural components.

Other important topic is the correct implementation of the strain rate dependent properties in the FE software. From the compression experiments of material coupons and structural component specimens, an accurate description of the material's strain rate dependent behaviour is found. It is then important to correctly implement these properties in a FE software to be able to perform simulations of crash events which yield realistic results.
Two main groups of numerical models are available. The first one, the micro-mechanical, consists in accurately simulating the micro-mechanical behaviour by considering the composite as a non-homogeneous structure, through a detailed modelling of the composites constituents and their interaction. These kind of models require an extremely fine mesh and, thus, are very expensive computationally, which makes them not practical for crash analysis of relatively large structures. The other group, the macro-mechanical one, works on the basis of a macro-mechanical description of the composite's plies. Its shortcoming is the inability of precisely modelling the laminates damage propagation on a micro-scale level. However, macro-mechanical models are much less computationally expensive and, thus, ideal for crash analysis of entire car structures. Since one of the final goals is to implement the strain rate dependent models in Audi's full vehicle crash simulations, the efficiency of the macro-mechanical models prevails over the higher accuracy of the micro-mechanical models.
The commercially available FE software Pam-Crash® allows for an easy and accurate implementation of the strain rate dependent behaviour of FRP. Furthermore, the usage of explicit analysis leads to an improved efficiency, as the global stiffness matrix does not need to be determined and inverted every increment. The utilization of very small time steps, together with the simple implementation of contact and penetration constraints, make Pam-Crash® a suitable FE code for crash and impact simulations on the automotive industry.

2.7 Summary and Conclusions

In the present chapter, a review of the studies used for this thesis was presented. In section 2.1 the behaviour of the individual constituents of fibre-reinforced polymers was given. Carbon fibre bundles show no strain rate dependency, as their behaviour under tension is not influenced by the loading rate. On the other hand, epoxy systems show different mechanical responses when loaded at different rates. Overall, the maximum stress, initial modulus and yield stress/strain of neat epoxy specimens increases with increasing strain. This effect is apparent under compression, tension and shear loads.

In section 2.2, the effect of the strain rate on FRP was presented, with a special focus on carbon fibre laminates. In general, the matrix-dominated properties of carbon-epoxy laminates are strain rate dependent. This is the case for transverse compression and tension of unidirectional laminates, as well as for the shear behaviour. It was shown in section 2.3 that the variation of these matrix-dominated properties of laminates is in line with the variation seen on pure epoxy systems. This conclusion was reached by normalising the results obtained at different strain rates for pure epoxy and fibre-reinforced specimens with their respective quasi-static values. The trend of increasing mechanical properties of neat epoxy is very similar with the increasing trend of matrix-dominated properties of laminates.

On the other hand, as consequence of the results obtained when testing carbon fibre bundles, the fibre-dominated properties of carbon-epoxy laminates should not be strain rate dependent. This is the case when performing longitudinal tensile tests of unidirectional laminates. The tension mechanical response in fibre direction is the same, whether the loading rate is low or very high.

However, this is not the case when performing compression tests in fibre direction. There is a clear increase in longitudinal compression strength and failure strain with increasing strain rate. An explanation for this effect might be related with the typical failure types that occur under compression. Failure of unidirectional laminates under compression is usually related with fibre microbuckling, leading to the creation of kink bands and subsequent abrupt failure. This occurs because the resin reaches its yielding point locally and fails to provide support for the fibres. Nonetheless, with increasing strain rate, the mechanical properties of the resin increase, which means that the fibres are better supported and the entire laminate can reach higher compressive strains. Most authors report an increase in compressive strength and failure strain of approximately 50% over the quasi-static values, when testing at strain rates of 100 s^{-1}.

Section 2.4 contains a short overview of the influence of several specimen geometrical factors on the measured compressive properties. In short, an increase in either the specimen thickness or width tends to reduce the measured strength, because with increasing specimen volume there is a higher chance of manufacturing defects being present, which can lead to premature failure. The specimen gauge length seems to have no effect, as long as Euler buckling is taken into account when defining the length.

In section 2.5 a comparison between two studies is presented, in which the software Pam-Crash® is used to predict the outcome of crash events using FRP. From the compared results, it is clear the importance of having a strain rate dependent model. As FRP show different mechanical response under high rates, having a numerical simulation which uses quasi-static material data will largely under predict the experimental results.

Finally, in section 2.6 the objectives and research questions of this thesis project are presented.

Chapter 3

Experiments

In the current chapter, the results from the experimental tests, the associated testing equipment and experimental methods adopted are presented. In section 3.1, the methodology used to measure and determine the material properties from the tests is presented. Section 3.2 contains a brief description of the testing equipment used, such as the servo-hydraulic testing machine, the compression fixture and the procedure adopted to manufacture the specimens. In section 3.3 an analysis on the effect of the different geometrical factors of the rectangular specimens is presented, from which an ideal geometry is extracted and adopted for the dynamic compression tests. The results of these dynamic tests with five different layups subjected to six strain rates are then presented in section 3.4. Finally, crash tests are also performed on structural components with an omega-profile cross-section at three different compression speeds and the results are shown in section 3.5.

3.1 Experimental methods

3.1.1 Digital Image Correlation

There are several methods to measure the strain during testing of coupons or structures. These can be classified into contact and contactless methods. In the former category, the typical and most used is the strain gauge, which requires an intensive process of placement and connecting when testing a high number of specimens. Furthermore, it has the disadvantage of providing strain information only in the area which it has contact with.

On the other hand, contactless methods are usually less stringent and can be used to reach fast specimen preparation and turn around times. Moreover, these methods allow for a much broader range of strain measurement, can be used in either micro or very large structures and allow the attainment of full-field translations, rotations, shear and normal strains [47]. The most commonly used of these contactless methods is DIC, which is the strain measuring technique used across this work.

DIC is an optical measurement technique, which uses digital image processing and numerical computing to track patterns before and after deformation. A camera captures pictures throughout the test at a given frame rate. The pictures are then imported into a DIC software and compared with the initial (reference) frame. From the variation between frames, strain information can be determined. This section includes an overview of this strain measuring technique.

Before the test, the specimen has to be prepared with a stochastic grey-scale pattern. This was achieved using white and black Aerosol spray paints. The generated pattern is the carrier of the deformation information because it deforms together with the specimen. The size of the black dots on the stochastic pattern must be chosen accordingly with the area of interest, the camera resolution and the strain resolution required. Furthermore, the grey intensity distribution (measured between 0 and 255) needs to be well distributed close to the middle of the scale, i.e. there should not be any spot too bright (close to 255) nor too dark (close to 0 on the scale), as this can affect the correct processing of the pattern. The greyscale intensity of the specimen pattern can be adjusted with the aperture of the camera lenses, the light source or the camera shutter speed.

To perform a tracking analysis between frames, the area of interest is divided into evenly spaced squares of equal pixel size, which are named facets. Ideally, the facet size must be chosen such that each facet contains three black dots of the pattern inside of its area. Throughout this work, a facet size of 15 x 15 pixels^2 was used, which means that each black dot should be 6 to 9 pixels wide. The DIC technique tracks subsets of pixels (facets) instead of tracking pixels by themselves because each facet contains a wider range of greyscale levels, which makes it easier to distinguish between facets from frame to frame [47]. Therefore, each facet is easily identifiable from the reference to the deformed frames.

There are several correlation criteria to judge the matching between facets across frames, and these are explained in detail by Pan et al. [47].

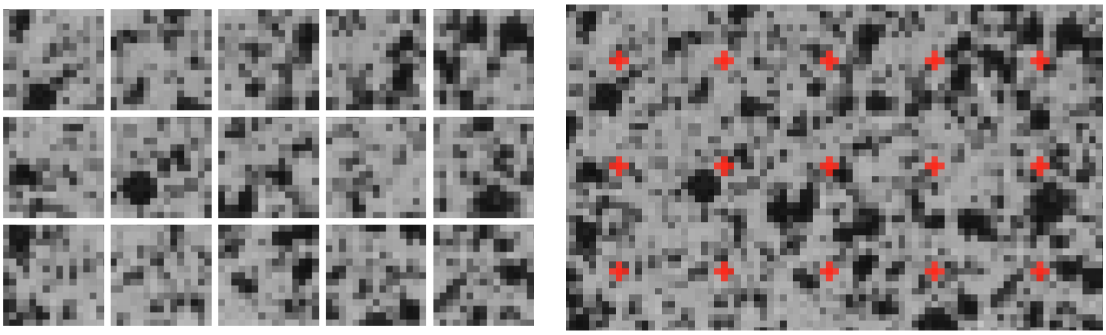

(a) Speckle pattern with facets of 15 pixel size **(b)** Center points of each facet, where the displacement vector is determined

Figure 3.1: Example of speckle pattern with corresponding facet center points.

Figure 3.1 **(a)** shows an example of a stochastic pattern with a facet size of 15 x 15 pixels^2, while **(b)** depicts the corresponding center point of each facet used to determine the displacement vector between reference and deformed shape. Using first order shape functions and the displacement vector of the facet center point, the shape change of the facet can be evaluated and the displacement field is determined. From the displacement field, the displacement gradients (strain) can be estimated through several methods, as explained in detail by Pan et al. [47] or in the book of Sutton et al. [48].

For the tests of the current work, two Photron FASTCAM SA-X high-speed cameras were used. The cameras were placed approximately 550 mm from the specimen and lenses with 100 mm focal length were used, together with 75 mm extension tubes. For most tests, the camera's resolution was set to 384 x 448 pixels^2, since it was enough to get a proper strain resolution on the area of interest. The maximum frame rate of the cameras is limited by the resolution of the pictures, since the speed at which the cameras can write in its internal memory is the limiting factor. For a picture resolution of 384 x 448 pixels^2, the maximum frame rate the cameras can achieve was 54 000 frames per second, which was the recording speed used for tests at a piston velocity of 1 m/s.

The DIC software used in this work was ARAMIS®, supplied by GOM.

3.1.2 Interpretation of test data

In this subsection, a brief explanation will be given regarding the interpretation of the data resulting from the tests and how several properties of the laminate are determined.

Applied Load and Stress

The servo-hydraulic testing machine is displacement-controlled and does not incorporate a load cell. However, the compression fixture used for all the compression tests has a load sensor in its base, as will be shown in section 3.2.2. Therefore, the load applied by the testing machine piston, to which the specimens are subjected to, is directly measured on the fixture. The load signal is sampled by a National Instruments data logger at a rate equal to the camera's frame rate. Moreover, synchronization between the cameras and the data logger is assured through the camera's software, i.e. each measurement of the load is taken at the exact same time as the cameras save a frame of the specimen.

The stress applied at the specimen is simply the load signal being measured divided by the cross-section area of the specimen.

Specimen Strain and Strain Rate

The strain field is obtained thought DIC and the speckle pattern painted on the specimen. It is important to note that the strain field should be close to homogeneous in the loading direction. Any significant displacement in the out-of-plane direction might be related to excessive bending, which leads to the creation of additional stresses.

The strain rate is defined as the variation in strain with respect to time. Therefore, it is determined by differentiating the average longitudinal strain across the area of interest with respect to time.

Ultimate Stress and Strain

During compression testing of carbon-epoxy laminates, failure occurs suddenly and abruptly. Therefore, there is a clear peak on the force signal, after which the specimen is not able to carry load any more. Therefore, the peak in load/stress corresponds to the compressive strength of the laminate.

The strain at which the peak stress occurs is the ultimate strain.

Stiffness

As no testing standard exists for dynamic testing, the static standard (ASTM D6641 [37]) was adopted to determine the laminate longitudinal stiffness. Therefore, the compressive modulus in fibre direction was determined over an axial strain range from 1000 to 3000 microstrain by fitting a linear regression model and taking its slope as the modulus. It is important to note that, due to the dynamic characteristic of the experiments and the noise induced by the testing machine, both the load and the strain signal are quite wavy. Therefore, a smoothing function had to be applied to the stress-strain curves. Figure 3.2 shows a comparison between a stress-strain curve plotted using the raw signals and its corresponding smoothed curve.

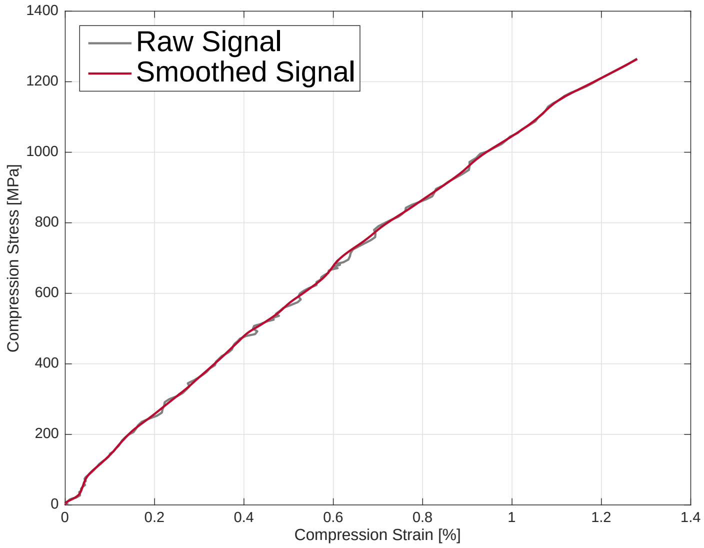

Figure 3.2: Comparison between raw and smoothed stress-strain curves of a compression test performed at 0.01 m/s of a $[0°]$ laminate.

For the transverse and shear moduli, a similar approach was used, except that the strain range from which a linear fitting was adopted is from 4000 to 8000 microstrain. The reason for this is related with the higher compressive strains that $[90°]$ and $[+45°/-45°]_s$ laminates are able to support before failure.

3.2 Testing equipment

In the current section, the most relevant testing equipment is shown, such as the servo-hydraulic testing machine, the compression fixture and the process for the preparation of the carbon-epoxy laminate is briefly presented.

3.2.1 INSTRON Very High Speed (VHS) testing machine

As demonstrated in chapter 2, it is not possible to use a single testing machine to reach the entire range of strain rates, from low (order of magnitude 10^{-5} s^{-1}) to very high (up to several thousands s^{-1}) . Low strain rate tests are usually performed in typical universal or screw driven testing machines, while moderate loading rates are achieved using a servo-hydraulic or a drop-tower apparatus. The higher range of strain rates is only feasible using a SHPB testing rig. For this work, the purpose is to study the compressive behaviour of carbon-epoxy laminates subjected to strain rates varying from the typical quasi-static values (order of magnitude 10^{-5} s^{-1}) to moderate (up to $100 - 200$ s^{-1}). Therefore, the testing machine used during this work was servo-hydraulic machine by INSTRON, which is highly versatile and allows the accomplishment of the desired strain rate range. Figure 3.3 presents the used testing machine with its main components.

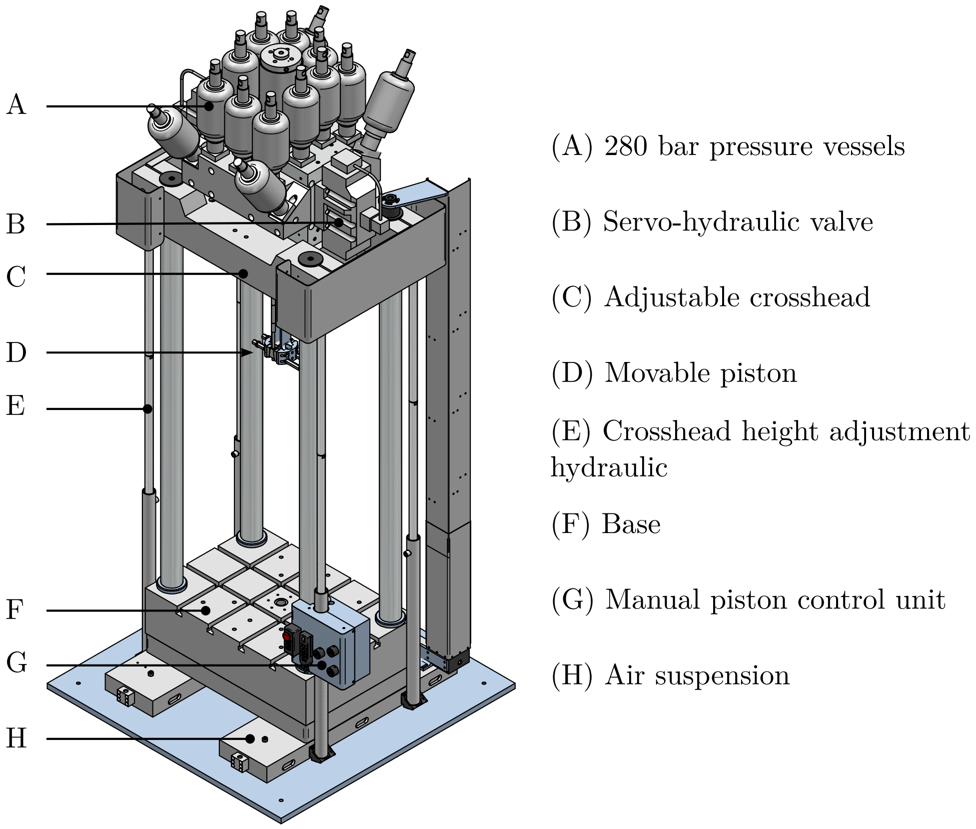

(A) 280 bar pressure vessels

(B) Servo-hydraulic valve

(C) Adjustable crosshead

(D) Movable piston

(E) Crosshead height adjustment hydraulic

(F) Base

(G) Manual piston control unit

(H) Air suspension

Figure 3.3: INSTRON VHS Servo-hydraulic testing machine and its main components [49]

The piston of the used servo-hydraulic machine is able to reach a maximum speed of 10 m/s for compression tests, i.e. for a downwards movement. The maximum load applied on the fixture is limited to 80 kN by a security shear pin on the main shaft of the machine. The internal oil is accumulated in the top pressure vessels at a pressure of 280 bar. To start a test, a controlling valve opens according to the requested testing speed and the oil is released into an acceleration circuit. Due to this very high-pressure system, the piston is able to accelerate up to its maximum speed of 10 m/s in just a few millimetres distance.

3.2.2 Compression fixture

The in-house developed compression fixture used to perform the experiments was designed to be specifically used with the testing machine presented previously. Figure 3.4 shows the two variations used: on the left-hand side the initial design used to test simple rectangular specimens, and on the right-hand side the modified version used to perform axial compression on omega-profile structural components. The fixture contains a piezoelectric load cell (Kistler 9051A for the left-hand side configuration and Kistler 9071A for the right-hand side configuration of Figure 3.4) on the bottom, which connects to an amplifier before having the signal sampled at the data logger. The specimen is fixed at both sides with fixing jaws containing spikes to prevent specimen movement. Furthermore, on the left-hand side configuration, there are three vertical guiding rods which ensure that the specimen is subjected solely to a vertical movement, even if the impact is not completely vertical. On the top, a cone endures the impact and performs small adjustments to the alignment of the impactor attached to the piston. The load is introduced in the specimens through a combined methodology: via end loading at the top and bottom of the specimen and through the tabs via shear introduction, a concept similar to the Northwestern University (NU) compression testing fixture [29].

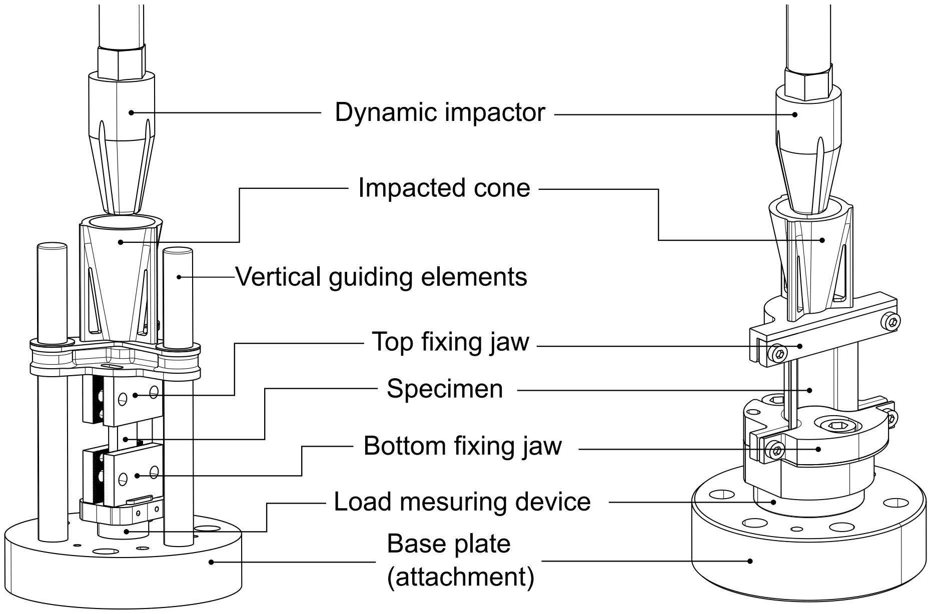

Figure 3.4: Compression fixture used to test simple specimens (left) and omega-profile structural components (right).

3.2.2.1 Bending factor determination

As mentioned in subsection 2.4.3.1, the determination of the bending factor is an important parameter to ensure that the specimens are not being subjected to critical additional stresses related with bending. Therefore, nine specimens were prepared with back-to-back strain gauges and tested until failure. From the signal of both strain gauges, the bending factor can be determined according to equation (2.11). Out of the nine specimens equipped with strain gauges, three had a unidirectional $[0°]_{16}$ layup, three had a biaxial $[0°/90°]_{4s}$ layup and the other three a quasi-isotropic $[+45°/-45°/0°/90°]_{2s}$ layup. Figure 3.5 presents the compressive stress-strain curves obtained for a test with a UD **(a)** and a quasi-isotropic **(b)** specimens.

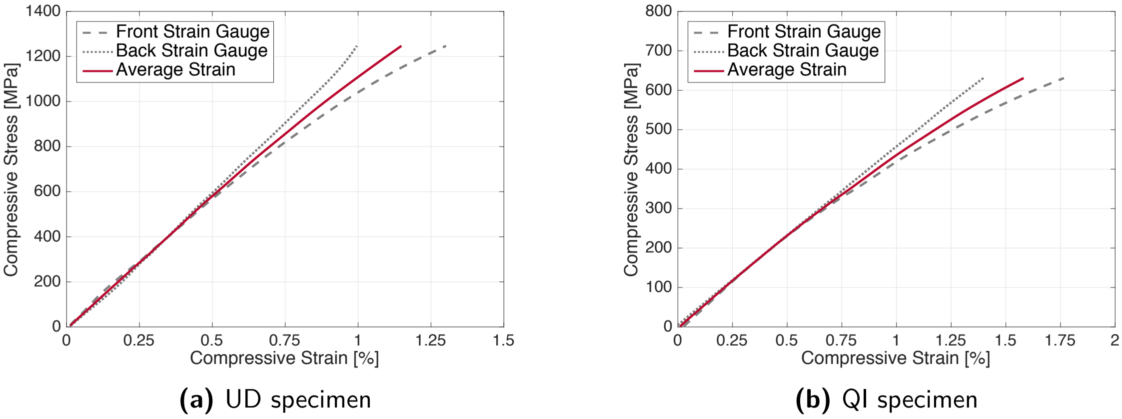

(a) UD specimen **(b)** QI specimen

Figure 3.5: Example of stress-strain curves obtained to analyse the fixture's bending factor.

The analysis regarding the bending factor is made easier if equation (2.11) is plotted as function of the average strain between the front and back strain gauges, as shown in Figure 3.6. It is typical and practical to use the point in which the strain reaches 90% of the failure strain to evaluate the validity of the test. As Figure 3.6 shows, for the nine specimens with three different layups, the bending factor at this critical point is always at or below 10%. Therefore, it can be concluded that the fixture is well aligned and it is not developing additional stresses on the specimens due to bending.

3.2.3 Specimen preparation

Throughout this work, the specimens used were manufactured using high-strength standard-modulus T700S carbon fibre by Toray, pre-impregnated in DT120 epoxy matrix by DeltaTech. The UD prepreg system has an areal weight of 150 g/m^2 and is 0.15 mm thick.

Rectangular specimens preparation

After stacking the plies with the desired orientation and amount of layers, the 500 × 600 mm^2 plates were cured in an autoclave according to the manufacturer's guidelines (120 °C for 1.5 hours). After curing, the plates were cut into smaller 200 × 100 mm^2 panels using a water-cooled diamond saw and 2-mm thick glass-epoxy QI tabs were glued using DP490 Scotch-Weld® adhesive by 3M. Finally, the individual specimens were cut from the panels to the correct dimensions using again a water-cooled diamond saw. Once finished, each individual specimen was measured using a caliper with a ±0.01 mm precision: three thickness measurements, two gauge length measurements (distance between the glass-epoxy tabs) and three width measurements. The dimensions were stored for later determination of the specimen axial stress.

The fibre volume content of each plate was measured at 9 positions and the averaged results are shown in Table 3.1. Furthermore, additional samples were taken from every plate and

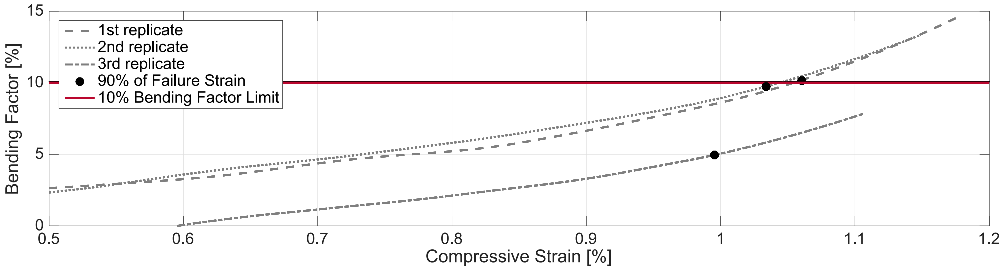

(a) $[0^\circ]_{16}$ specimens

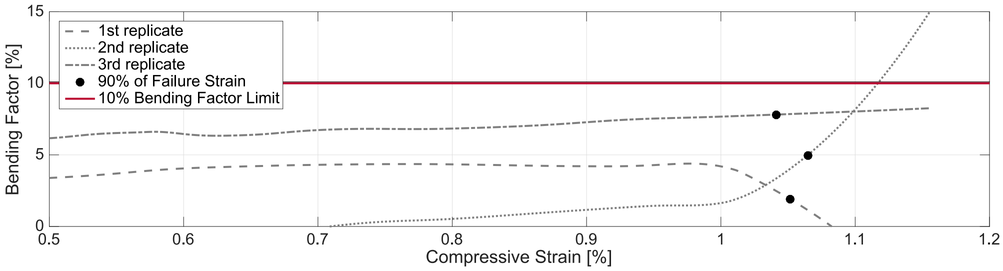

(b) $[0^\circ/90^\circ]_{4s}$ specimens

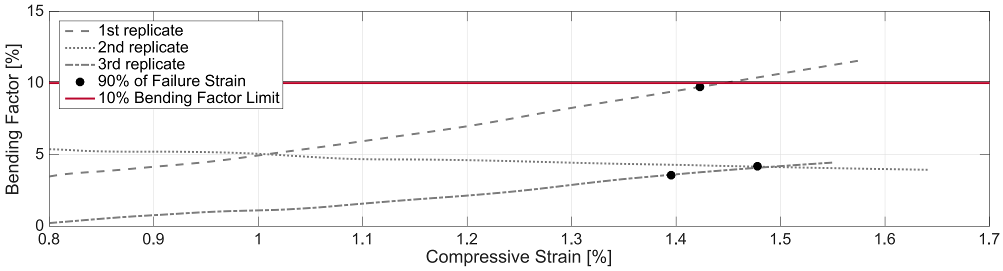

(c) $[+45^\circ/-45^\circ/0^\circ/90^\circ]_{2s}$ specimens

Figure 3.6: Bending factor as function of the average strain for the nine specimens tested with strain gauges.

run through the Differential Scanning Calorimetry (DSC) machine (Mettler Toledo). For all plates, the resin curing degree was between 99.5% and 100%.

Omega-profile cross-sectional specimens preparation

The second type of samples manufactured consists of 100 mm long omega-profile cross-section specimens. These were produced using the same combination of fibre and resin prepreg as the rectangular specimens. The prepreg layers were hand-laid on a concave omega-shape mould and cured also at 120 °C for 1.5 hours. Finally, the edges were trimmed to ensure proper specimen alignment. More information about the dimensions and layup of these specimens is presented later on in section 3.5.

3.3 Test results: specimen geometry optimization

As mentioned in section 2.6, there is no adopted standard for dynamic compression testing of fibre-reinforced polymers. Furthermore, the in-house developed fixture does not allow the use of the specimen geometry as recommended in the static standard ASTM D6641 [37] due to

Table 3.1: Average Fibre Volume Content of each plate.

Plate Layup	Number of plies	Plate thickness [mm]	Fibre Volume Content [%]
$[0°]_{13}$	13	1.95	54.22
$[0°]_{16}$	16	2.40	52.60
$[0°]_{20}$	20	3.00	54.23
$[0°]_{27}$	27	4.05	53.99
$[0°/90°]_{4s}$	16	2.40	52.68
$[+45°/-45°/0°/90°]_{2s}$	16	2.40	53.23

Table 3.2: Upper and lower boundaries for the three geometrical factors whose effect was investigated.

	Thickness [mm]	Width [mm]	Gauge Length [mm]
Lower Limit (-1)	2	10	7
Upper Limit (+1)	4	15	13
Center Point (0)	3	12.5	10

geometrical restraints of the fixture and load limitations of the testing machine. Therefore, a study to find the specimen geometry that leads to the optimal results was performed. In this section, the approach to test several specimen geometries and the results obtained are presented, together with the resulting ideal geometry.

3.3.1 Testing plan

For each of the three geometrical factors whose effect was to be investigated, a lower and an upper testing limit had to be defined. For the specimen thickness and width, the upper limits are related with the maximum force that the machine can apply, since the specimens must be loaded until failure. The thickness lower limit and the gauge length upper boundary are limited by the Euler buckling analysis shown in section 2.4.3. The width and gauge length lower boundaries are both related with the surface area needed to have a proper speckle pattern to use the cameras and the DIC software. Given these constraints, Table 3.2 summarizes the lower and upper limits defined for each of the three geometrical factors.

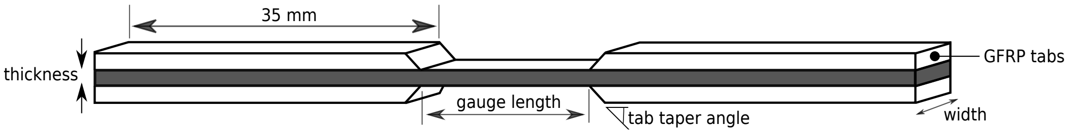

Figure 3.7: Specimen sketch with its main geometrical features.

A 2-level full factorial design approach was selected to investigate the influence of each geometrical factor. For this, every combination in which each factor is at either its lower or upper boundary is tested. Even though the varying factors can take any value in between

Table 3.3: Full factorial testing plan (codded according to Table 3.2) adopted to investigate the influence of each geometrical factor.

Combination #	Thickness	Width	Gauge Length
1	-1	-1	-1
2	-1	-1	+1
3	-1	+1	-1
4	-1	+1	+1
5	+1	-1	-1
6	+1	-1	+1
7	+1	+1	-1
8	+1	+1	+1
9 (CP)	0	0	0

the two boundaries, performing tests with the factors at their lower and upper limits is the most efficient way to determine the influence of each of them on the measured compressive properties. Additionally, a unique combination must also be tested - called a center point (CP) - in which all the factors are at the middle of its varying range. The center point of the testing design is extremely valuable because it allows the detection of non-linearities in the influence of each factor.
Table 3.3 summarizes the testing plan in a coded manner, i.e. -1 symbolizes the lower limit, $+1$ represents the upper limit and 0 stands for the middle point of the varying range.

An additional investigation was carried out to determine whether the tab taper angle (see Figure 3.7) should be 90° or 30°. The tab taper angle is the inclination in which the GFRP tabs are cut near the gauge length. Untapered tabs (90° taper) induce a higher stress concentration, since the stiffness mismatch is abrupt. On the other hand, even though tapered tabs reduce the stress concentration factor, they provide few lateral support for the specimen in the taper region, leading to an increase in effective gauge length, which can cause Euler buckling issues. Therefore, a lower limit of 30° for the tab taper angle was chosen because it is commonly adopted throughout previous studies and was found to be a good compromise between stress concentration factor and increase in effective gauge length [36, 50].

The investigation to conclude about the ideal specimen geometry that should be used in further tests was performed using only specimens with a [0°] layup and at quasi-static testing speeds, i.e. a piston velocity of 2 mm/min. The reasoning for this choice has to do with the variability associated with compression testing, and especially with the testing machine available. Preliminary experimental tests had shown that the standard deviation of the achieved strength distribution of similar experiments is relatively high - as high as 15% of the mean. This means that, in order to obtain a mean strength within an accurate confidence interval, a high number of replicates is necessary. Therefore, 12 replicated experiments were performed for each combination of thickness, width and gauge length shown in Table 3.3.
As shown in section 2.4, the compression modulus is not affected by variations in the geometry of the specimen. On the other hand, the achieved compression strength is affected by variations in thickness and width. Therefore, the compression strength was chosen as the criterion to compare between different specimen geometries.

3.3.2 Results

3.3.2.1 Tab taper angle effect

As mentioned earlier, an investigation was also performed to assess whether tapered or untapered GFRP tabs should be used. Figure 3.8 shows a comparison of the achieved compression strength between specimens manufactured with five combinations of thickness, width and gauge length, with either tapered or untapered tabs.

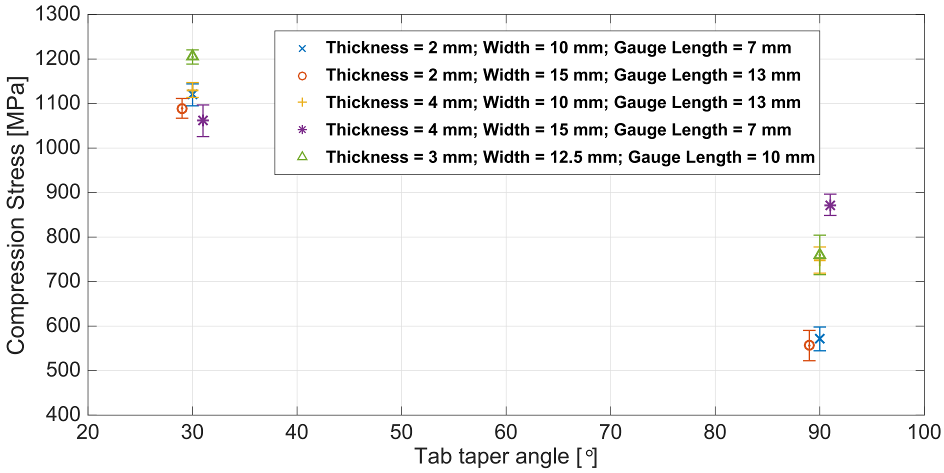

Figure 3.8: Effect of tapered and untapered GRFP tabs on the achieved compression strength.

It is clear that using untapered tabs leads to a significant reduction in compression strength. In some cases, the supported load drops up to −50% between tapered and untapered. For the five different geometries tests, the usage of tapered tabs resulted in an average strength of 1121 MPa, while specimens with untapered tabs reached an average ultimate stress of 702 MPa. This result clearly shows that using untapered specimens leads to a significant increase in the stress concentration factor near the tab end, which is where most of these specimens failed. On the other hand, using tapered specimens induces a smoother load introduction near the tab end, which results in the higher strength achieved.

Additionally, the standard deviation of the 12 replicates tested for each geometry combination is significantly smaller for specimens with tapered tabs. Untapered tabs lead to an average coefficient of variation (CV) of 14.4%, while tapered tabs specimens show, on average, only 5.6% of CV.

Therefore, the conclusion is simple and straightforward: specimens with tapered tabs are not only able to support much higher loads due to smaller stress concentration factors at the tab ends, but also the variability is much lower, which indicates that tapered specimens are less susceptible to small manufacturing defects or misalignments in the placement of the GFRP tabs. These results are in agreement with the conclusions presented in a study by Adams and Odom [50]: unidirectional CFRP specimens equipped with tapered tabs reach higher strengths than with non-tapered tabs.

3.3.2.2 Thickness effect

Using the previously shown conclusion that specimens with tapered GRFP tabs yield higher compressive strength than specimens with untapered tabs, and following the testing plan presented in Table 3.2 and Table 3.3, the effect of changing the specimen thickness is shown in Figure 3.9.

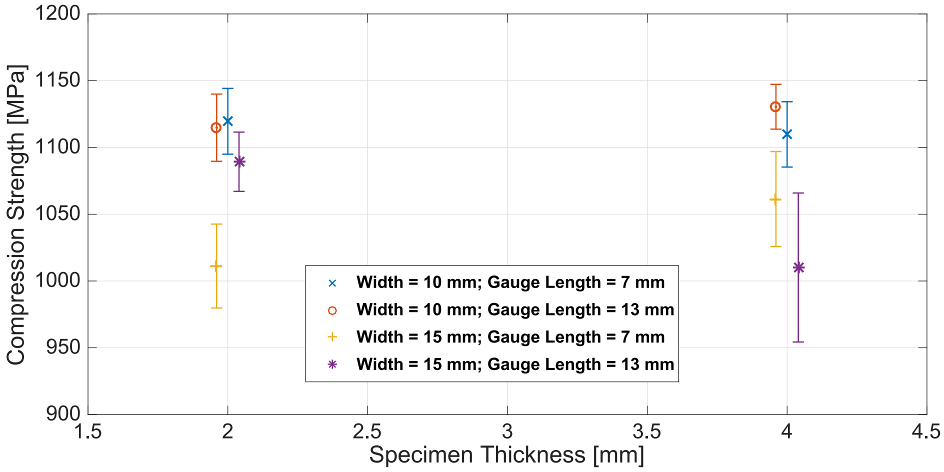

Figure 3.9: Effect of specimen thickness on the compression strength.

It is important to note that in Figure 3.9 some results are shifted on the X-axis for easier analysis of the results. The results shown are for specimens 2 and 4 mm thick.
By performing a statistical significance analysis of the data, it can be concluded that the effect of the thickness is not statistically significant. This means that the difference in results obtained between the two thickness levels can not be attributed to the effect of the thickness solely. However, the tests performed with thicker specimens (4 mm) resulted in a high percentage of non-acceptable failure types. 55% of the 4-mm thick specimens showed failure in the load introduction region, i.e. near the end of specimen. This is attributed to the higher load needed to reach the same stress level and the strength of the adhesive used to glue the GFRP tabs. As the load on the thicker specimens reached higher levels, the adhesive failed and the GFRP tabs became lose, which caused all the load to be introduced at the specimen's ends, leading to crushing at the extremities.
Therefore, even thought there is no statistically significant difference in strength between specimens 2 and 4 mm thick, the specimen's thickness should be kept low in order to prevent non-acceptable failure types, especially since for the dynamic tests it is expected the strength to increase with increasing strain rate.

3.3.2.3 Width effect

In a similar fashion as presented in the previous section, the effect of the specimen width on the measured compression strength is presented in Figure 3.10. Again, for the sake of better analysing the graph, some data is shifted along the X-axis.

Comparing the results obtained at the lowest and highest width levels (10 and 15 mm, respectively), there is a statistically significant difference in strength between them. Taking into

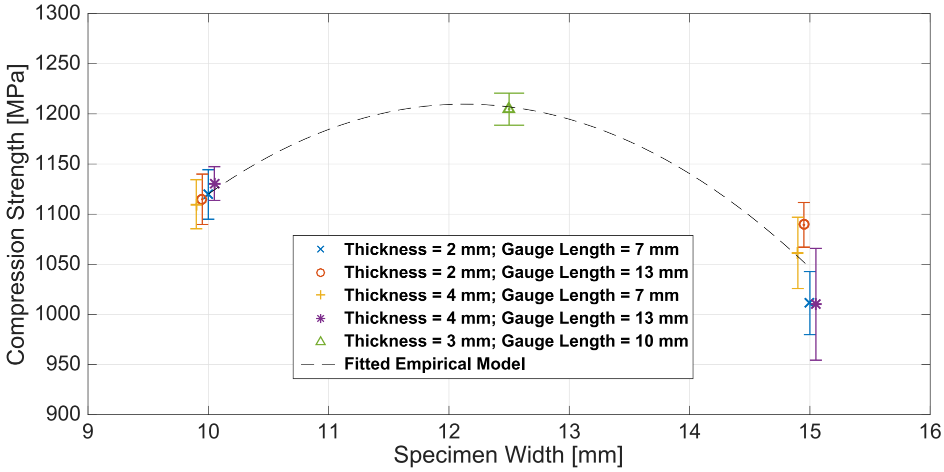

Figure 3.10: Effect of specimen width on the compression strength.

consideration the center point of the experimental design, a quadratic empirical equation can be fitted, which represents the effect of the width (W) solely. The fitted empirical quadratic model is also represented in Figure 3.10 and is described as:

$$X_c = -1703 + 480.3 \times W - 19.8 \times W^2 \text{ [MPa]} \tag{3.1}$$

which has a coefficient of determination $R^2 = 0.78$ and a maximum at Width $\approx 12.1mm$. The obtained model for the effect of the width is in agreement with the conclusions drawn in Section 2.4.2. Narrow specimens are more influenced by the specimen edge effect, which can have a negative influence on the achieved compression strength. On the other hand, wide specimens have a higher chance of containing manufacturing defects, leading to lower compression strengths. Therefore, there must be an 'optimal' width which is a compromise between these two effects, accurately predicted by a quadratic model.

3.3.2.4 Gauge length effect

Figure 3.11 shows the effect of the specimen gauge length on the measured compression strength for the different specimen geometries tested. Specimens with a gauge length of 7 and 13 mm are represented.

Similarly to the results obtained for the effect of the specimen thickness, there is no statistical significance in the difference in results achieved for different gauge lengths. This means that the effect of varying the gauge length solely between 7 and 13 mm has an effect on the compression strength that is smaller than the inherent variation resulting from the experimental data. Furthermore, no significant change in failure type was found at different gauge lengths.

3.3.3 Optimal specimen geometry

Following the results presented in sections 3.3.2.1 through 3.3.2.4, the tab taper angle was found to be the parameter which has the most effect on the measured strength. Between the

Figure 3.11: Effect of specimen gauge length on the compression strength.

two available type of tabs, the ones with a taper angle of 30° showed almost a doubling in compression strength, when compared with specimens equipped with untapered tabs.
From the analysis on the specimen thickness, it followed that its individual effect is negligible and the measured strength does not change significantly between specimens with a thickness of 2 and 4 mm. Nonetheless, the failure type changes with increasing thickness, and to reach acceptable failure modes in a higher number of experiments, the thickness should be closer to 2 mm.
The width was found to have a direct effect on the compression strength and the fitting empirical model presented in Figure 3.10 is maximal in the range $12 - 12.2$ mm.
Following the analysis presented, the specimen gauge length does not have a direct effect on the compression strength, in the range of 7 to 13 mm.

The presented analysis for the effect of each individual geometrical factor only arrives at a conclusion for the specimen width and the taper angle of the GFRP tabs. Nonetheless, an alternative approach to determine the influence of every geometrical factor is by using a Design of Experiments software that interprets all the test data at once and fits an empirical model to it. This was accomplished using the commercially available software MODDE® by the company Umetrics.
Since a full factorial experimental design approach (including a center point) was performed, it is possible to obtain a second-order empirical model, i.e. with terms containing up to second-order one-factor effects and interactions between factors. The resulting empirical model for the compression strength as function of the four previously presented geometrical factors is:

$$\begin{aligned} X_c = & -1977.5 + 162.7 \times t + 412.6 \times W + 27.2 \times L + 385.3 \times TAB \\ & -16.9 \times W^2 - 10.5 \times t \times L - 62.8 \times t \times TAB \quad \text{[MPa]} \end{aligned} \tag{3.2}$$

where t, W and L are quantitative factors that represent the specimen thickness, width and gauge length, respectively, and TAB is a qualitative factor related with the taper angle of the GFRP tabs:

$$TAB = \begin{cases} +1 & \text{if the tab taper angle is } 30^\circ \\ -1 & \text{if the tab taper angle is } 90^\circ \end{cases} \tag{3.3}$$

The fitted empirical model presented in equation (3.2) has a coefficient of determination $R^2 = 0.85$.

The usage of the advanced statistical software allows the creation of Probability of Failure (PoF) plots for the entire design space of each geometrical factor. The PoF plots take into account the variability between replicates and it displays the probability that a specimen with a given geometry fails to reach a certain target strength. Figure 3.12 shows a PoF plot for a fixed width of 12 *mm* and 30° GFRP tabs, as this were previously found as the optimal configurations of width and taper angle, respectively.

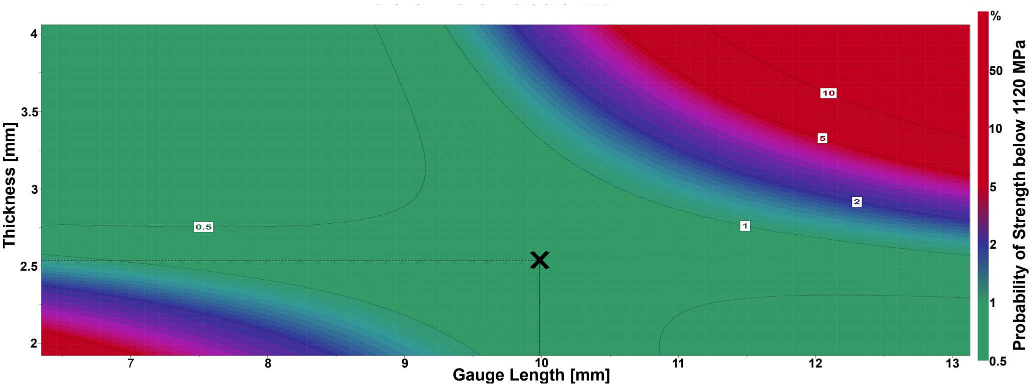

Figure 3.12: Probability of Failure plot (strength below 1120 MPa) for varying specimen thickness and gauge length.

The design area represented in Figure 3.12 shows the probability of a specimen with a certain thickness and gauge length of failing before reaching a compressive strength of 1120 MPa. The entire green area represents specimens geometries that have a 99% chance of failing above 1120 Mpa, and the optimal point suggest a gauge length of 10 mm and a thickness of 2.5 mm.

The chosen specimen geometry to be used in the dynamic tests is summarized in Table 3.4. The 30° taper angle for the GFRP tabs and a specimen width of 12 mm follow from the individual analysis of each parameter, shown in sections 3.3.2.1 and 3.3.2.3, respectively. A gauge length of 10 mm follows from the PoF plot presented in Figure 3.12. A specimen thickness of 2.4 mm was chosen because it is close to the optimal (2.5 mm) and, since each unidirectional ply has a thickness of 0.15 mm, using laminates with 16 plies allows for manufacturing of all the different layups with exactly the same thickness - for example, the QI laminate with a layup of $[+45^\circ/-45^\circ/0^\circ/90^\circ]_s$ must have a number of plies that is a multiple of 8, so a specimen thickness of 2.5 mm would not be practical.

Table 3.4: Specimen geometry chosen for the dynamic compression tests, following the analysis on the effect of each geometrical parameter.

Tab Taper Angle	Thickness	Width	Gauge Length
30°	2.4 mm	12 mm	10 mm

Table 3.5: Six piston speeds at which the five different layups were tested.

Testing Speed [m/s]					
3.3×10^{-5}	1×10^{-4}	1×10^{-3}	1×10^{-2}	0.1	1

3.4 Test results: dynamic compression tests

In the current section, the results obtained from the experimental tests of five different layups at several strain rates are presented. The specimen geometry used in the current section is according to the results of the optimisation performed in section 3.3.

3.4.1 Dynamic testing plan

The servo-hydraulic testing machine used for performing the compression tests can achieve piston speeds up to 10 m/s. However, the high-speed cameras available have a limited frame rate which depends on the size of the area being recorded. For the minimum area of interest necessary to perform a DIC analysis, the maximum frame rate achievable by the cameras limits the machine piston speed to 1 m/s. At faster testing speeds, the cameras are not able to save enough pictures to perform a proper DIC analysis. The six testing speeds chosen are presented in Table 3.5. For each combination of one of the six testing speeds and one of the five layups, 10 replicates were tested, which results in a total of 300 experiments being analysed in the current section.

The lowest speed corresponds to the typical quasi-static velocity of 2 mm/min. The other testing speeds were chosen to be equally spaced on a logarithmic scale because, as seen in chapter 2 for most of the mechanical properties of either resin specimens or laminates, the variations are better visualized when plotted on a logarithmic scale, instead of a linear one.

The strain rate that the specimen is subjected can not be determined straightforwardly from the piston speed and the specimen gauge length due to limitations of the test machine. Even though the piston reaches the desired speed quite accurately and in a short length, once the impactor hits the fixture, the piston tends to decelerate due to the stiffness of the specimen. For stiff specimens, such as the ones with the $[0°]_{16}$ layup, the piston's velocity drops to values close to zero after the initial impact. Nonetheless, the machine quickly accelerates the piston once again and it reaches the requested speed before the specimen fails. The deceleration right after the initial impact is higher for stiff specimens, while it is almost non-existent for softer specimens, such as the ones with a $[90°]_{16}$ or $[+45°/-45°]_{4s}$ layups. For this reason, the actual strain rate that each specimen is subjected to is determined on a case-by-case by analysing the variation over time of the strain measured with the DIC software, and not by

Table 3.6: Averaged longitudinal (in fibre-direction) compression properties at six different strain rates.

Strain Rate $\dot{\varepsilon}$ $[s^{-1}]$	Strength [MPa]	Fracture Strain [%]	Longitudinal Modulus [GPa]
$2.3 \pm 0.1 \times 10^{-4}$	1165 ± 10	1.15 ± 0.03	104.9 ± 2.2
$7.2 \pm 0.5 \times 10^{-4}$	1215 ± 45	1.18 ± 0.06	112.8 ± 2.1
$7.6 \pm 0.4 \times 10^{-3}$	1288 ± 10	1.29 ± 0.04	106.9 ± 3.0
$7.4 \pm 0.5 \times 10^{-2}$	1352 ± 25	1.33 ± 0.05	110.1 ± 3.5
$6.6 \pm 0.4 \times 10^{-1}$	1380 ± 13	1.36 ± 0.05	111.8 ± 2.9
4.1 ± 0.5	1422 ± 33	1.45 ± 0.06	111.2 ± 2.7

using the piston velocity. Specifically, the strain rate is determined by averaging the frame-by-frame strain rate over the last 30% strain before failure, i.e., from 70% to 100% of the failure strain of each individual specimen. This interval was chosen because it was found that, for all layups and piston velocities tested, the impactor had already recovered most of the speed it had lost after the initial impact.

3.4.2 [0°] layup

The stress strain curves obtained at the six piston velocities for the specimens with a $[0°]_{16}$ layup are presented in Figure 3.13, while the averaged main compression properties, such as the longitudinal strength, fracture strain and Young's modulus are summarized in Table 3.6.

The variation in longitudinal (in fibre-direction) compression properties with increasing strain rate is in very good agreement with the results reported by other authors and presented in chapter 2 section 2.2.2.1 [14, 16, 17]. Between tests performed at low (2.3×10^{-4} s^{-1}) and intermediate (4.1 s^{-1}) strain rates, the compression strength and fracture strain increase by 22% and 26%, respectively. On the other hand, the longitudinal compression modulus suffers no significant change.

The increase in strength and failure strain resulting from the current analysis is of a smaller magnitude than the increases reported by other authors [14, 16, 17], who mentioned increases between 40% and 80%, at strain rates ranging from 100 to 1000 s^{-1}, using a SHPB and a drop-tower apparatus. This difference in strength and failure strain increase can be explained by the lower strain rate achieved in the current analysis (maximum of $\approx$ 4.1 s^{-1}), by the different material systems used and dissimilar testing apparatus.

The stress-strain curves of Figure 3.13 show that the noise influence is quite significant, especially for the higher testing speeds. Most of the noise is introduced by the load sensor device, which captures vibrations of the fixture when it is hit by the impactor. A modal analysis to the fixture was performed using an impact hammer to excite the fixture with an impulse and measure its vibrational response, in order to determine its eigenfrequencies to try to reduce the effect of the fixture's vibration. This analysis is presented in appendix A.

The other major explanation for the waviness in the stress-strain curves has to do with the poor synchronization between load and strain signals for the higher testing speeds. The charge amplifier used to augment the signal from the piezoelectric load sensor has a delay below

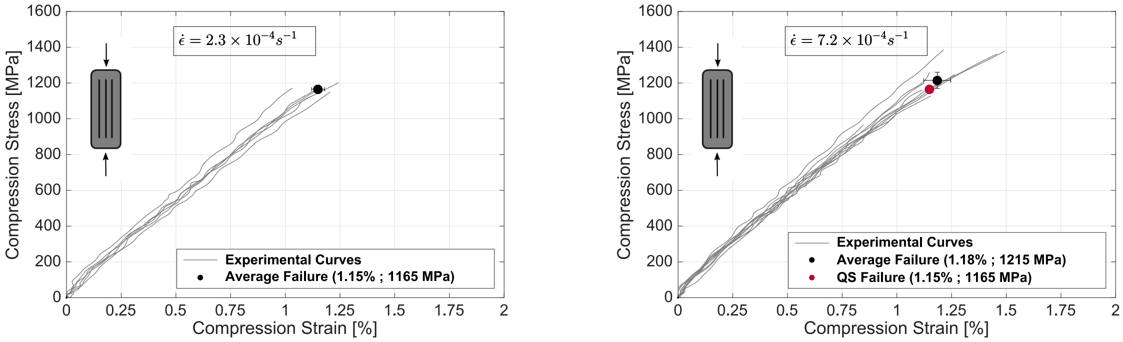

(a) Impactor Speed: 2 mm/min

(b) Impactor Speed: 6 mm/min

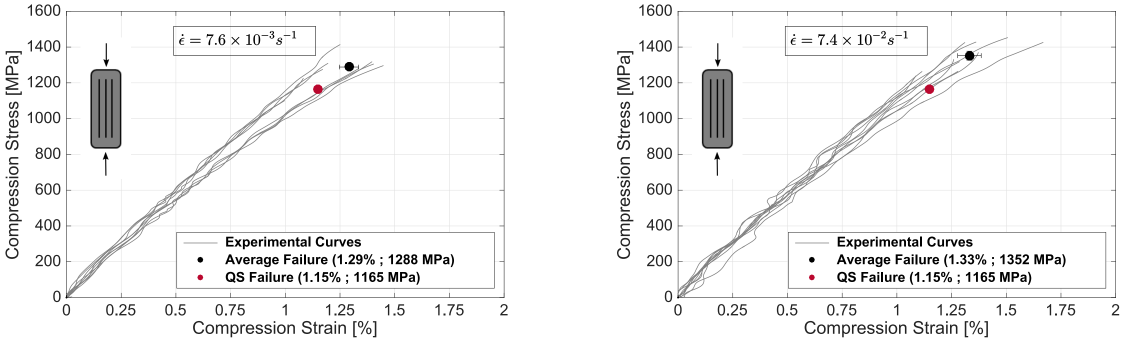

(c) Impactor Speed: 1 mm/s

(d) Impactor Speed: 10 mm/s

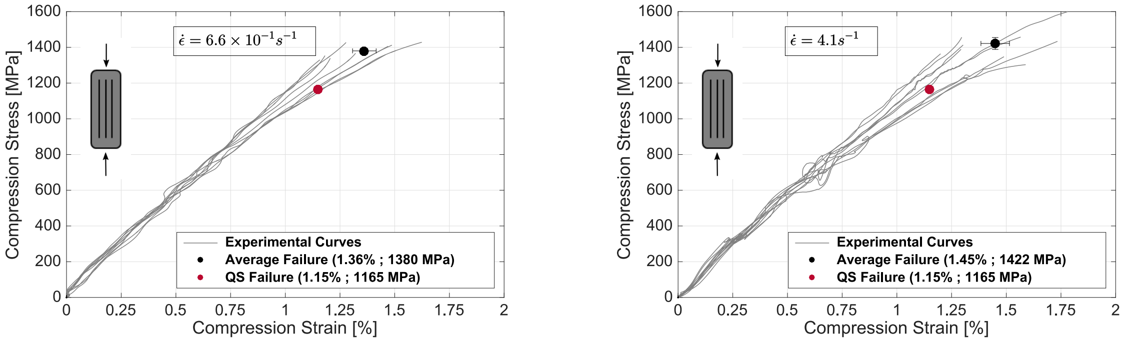

(e) Impactor Speed: 0.1 m/s

(f) Impactor Speed: 1 m/s

Figure 3.13: Stress-strain curves of $[0°]_{16}$ layup specimens at different impactor speeds.

0.1 millisecond. However, the delay set by the charge amplifier is not fixed, which makes it impractical to try to correct the load signal for the delay introduced in every single experiment performed. At low testing speeds, this delay set by the charge amplifier is insignificant when compared to the total duration of the test. However, at a testing speed of 1 m/s, the entire duration of the test, i.e. from the moment the impactor hits the fixture until the specimen breaks is approximately three to five milliseconds. Therefore, the delay introduced by the charge amplifier is significant in this case, which makes the load signal and the strain signal coming from the DIC software not being in phase, resulting in the unusual shape of the stress-strain curves of Figure 3.13 **(f)**, in the range of 0.6% to 0.8% strain.

3.4.3 [90°] layup

Figure 3.14 presents the compressive stress-strain curves of $[90°]_{16}$ layup specimens tested at six piston velocities. The corresponding strain rate and compressive properties are summarized in Table 3.7.

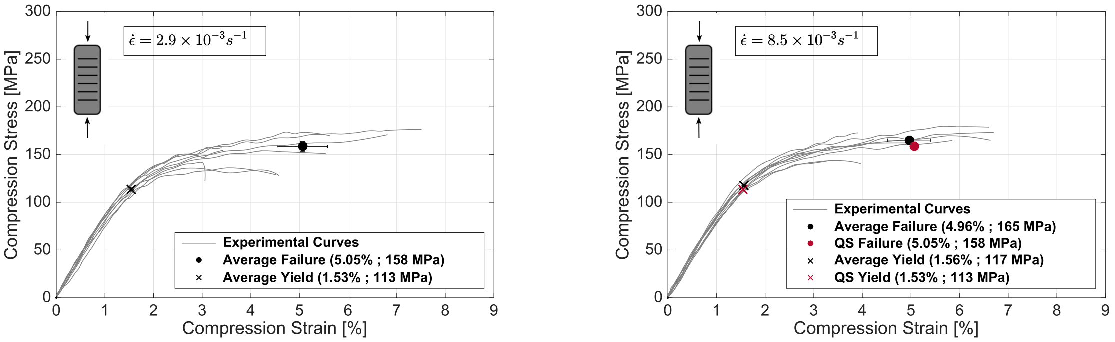

(a) Impactor Speed: $2\ mm/min$

(b) Impactor Speed: $6\ mm/min$

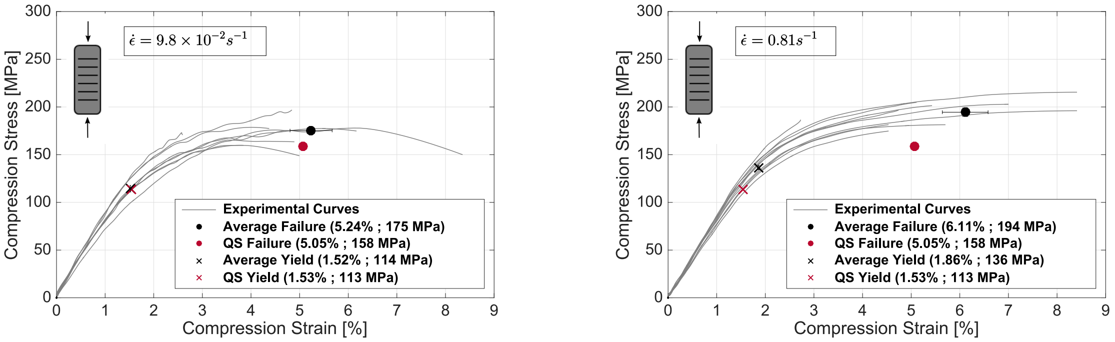

(c) Impactor Speed: $1\ mm/s$

(d) Impactor Speed: $10\ mm/s$

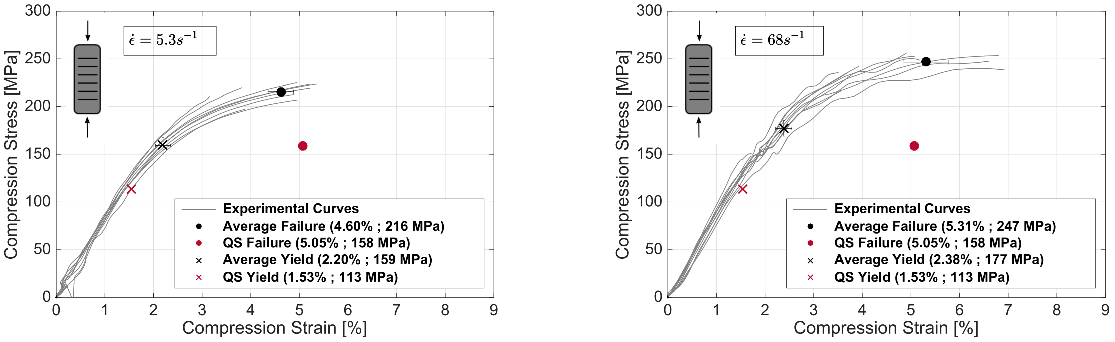

(e) Impactor Speed: $0.1\ m/s$

(f) Impactor Speed: $1\ m/s$

Figure 3.14: Stress-strain curves of $[90°]_{16}$ layup specimens at different impactor speeds.

Between the quasi-static tests and the ones at higher strain rate ($\approx 68\ s^{-1}$), both the transverse compressive strength and yield stress increase by 56%. The average fracture strain has high variability, but there is no significant change with increasing strain rate. Similarly, the

Table 3.7: Averaged transversal ($[90°]_{16}$ layup specimens) compression properties at six different strain rates.

Strain Rate $\dot{\varepsilon}$ $[s^{-1}]$	Strength [MPa]	Fracture Strain [%]	Yield Stress [MPa]	Transverse Modulus [GPa]
$2.9 \pm 0.5 \times 10^{-3}$	158 ± 5	5.05 ± 0.52	113 ± 2	8.53 ± 0.22
$8.5 \pm 0.8 \times 10^{-3}$	165 ± 4	4.96 ± 0.44	117 ± 1	8.59 ± 0.16
$9.8 \pm 1.1 \times 10^{-2}$	175 ± 4	5.24 ± 0.43	114 ± 3	8.70 ± 0.20
$8.1 \pm 1.0 \times 10^{-1}$	194 ± 4	6.11 ± 0.47	136 ± 2	8.22 ± 0.14
5.3 ± 0.6	216 ± 3	4.60 ± 0.26	159 ± 8	8.32 ± 0.25
68 ± 10	247 ± 2	5.31 ± 0.45	177 ± 8	8.29 ± 0.27

Table 3.8: Averaged shear ($[+45°/-45°]_{4s}$ layup specimens) properties at six different strain rates.

Strain Rate $\dot{\varepsilon}$ $[s^{-1}]$	Stress at 5% Strain [MPa]	Yield Shear Stress [MPa]	Shear Modulus [GPa]
$6.2 \pm 0.1 \times 10^{-3}$	60.0 ± 0.2	35.4 ± 0.4	3.49 ± 0.05
$1.9 \pm 0.1 \times 10^{-2}$	63.1 ± 0.3	37.1 ± 0.4	3.78 ± 0.06
$1.8 \pm 0.1 \times 10^{-1}$	67.2 ± 0.4	38.5 ± 0.5	3.70 ± 0.06
1.6 ± 0.1	70.9 ± 0.4	40.3 ± 0.5	3.73 ± 0.06
13 ± 1	76.8 ± 0.2	41.0 ± 1.2	3.75 ± 0.12
69 ± 4	76.3 ± 0.8	48.5 ± 2.0	3.51 ± 0.07

transverse compression modulus is not affected by the increase in loading rate.

These results are in agreement with the ones reported by Koerber et al. [22] and presented previously in section 2.2.2.2, who found increases of 45% and 83% over the quasi-static values for the compressive strength and yield stress, respectively, at a strain rate of $\approx 270s^{-1}$. Furthermore, the results shown here regarding the fracture strain are also consistent with the ones presented in section 2.2.2.2: whether the loading rate is low or high, the strain at which the specimen fails does not change.

However, Hsiao et al. [21] and Koerber et al. [22] also report an increase of 37% and 12%, respectively, on the transverse compressive modulus between static and dynamic tests, while in the current analysis the variation in modulus is not significant.

3.4.4 $[+45°/-45°]_s$ layup

To obtain information about the laminate's shear properties, specimens with a $[+45°/-45°]_{4s}$ layup were also tested under compression at different impactor velocities. The resulting shear stress-strain curves are shown in Figure 3.15 and the corresponding shear properties at different strain rate levels are outlined in Table 3.8.

It is important to mention that, according to ASTM D3518 [23], the tests were truncated at 5% shear strain. This has to do with extreme fibre scissoring, i.e. fibre reorientation, which means that after a significant strain, the fibres are no longer aligned with a +45° and −45° orientation with the applied load, which affects the mechanical response of the laminate.

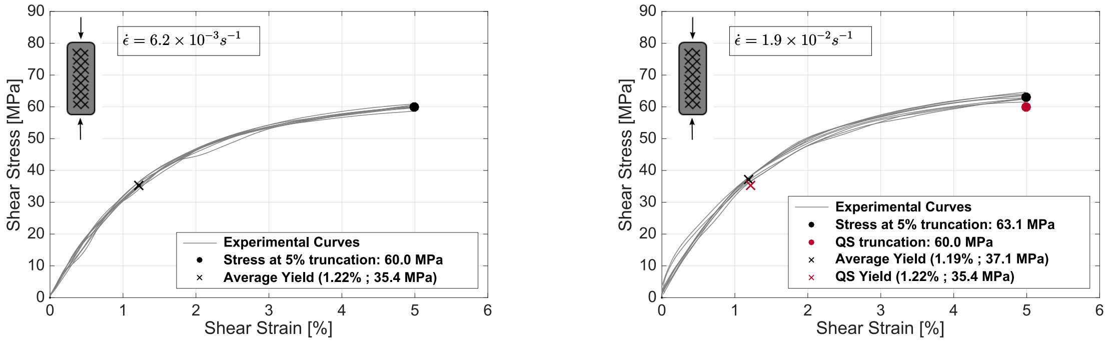

(a) Impactor Speed: $2\ mm/min$ **(b)** Impactor Speed: $6\ mm/min$

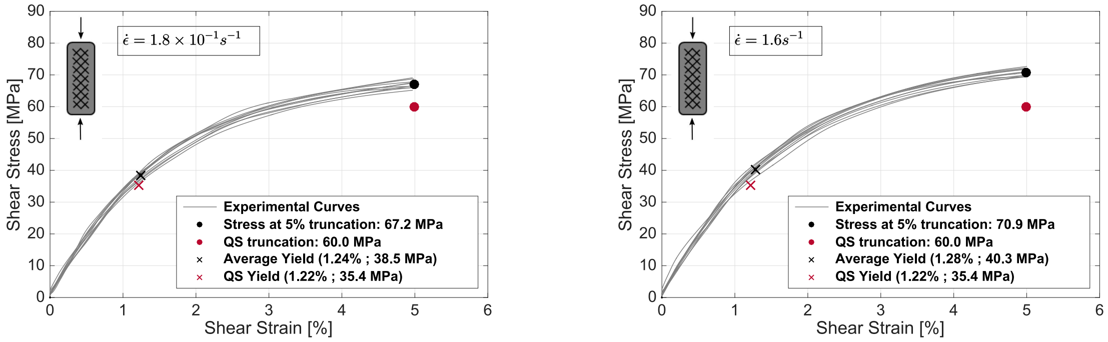

(c) Impactor Speed: $1\ mm/s$ **(d)** Impactor Speed: $10\ mm/s$

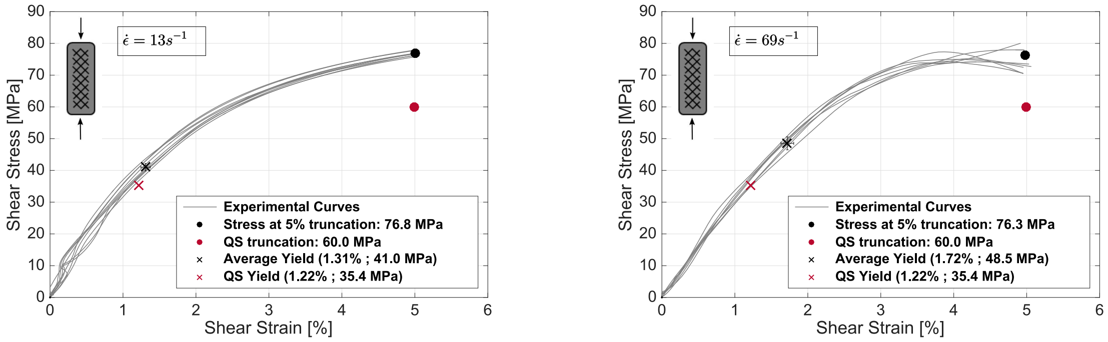

(e) Impactor Speed: $0.1\ m/s$ **(f)** Impactor Speed: $1\ m/s$

Figure 3.15: Stress-strain curves of $[+45°/-45°]_{4s}$ layup specimens at different impactor speeds.

In the present analysis, the shear strength (defined as the stress at 5% shear strain truncation) at the highest strain rate of 69 s^{-1} increases by 27% over the quasi-static value. This increase is inferior to the ones reported by other authors [12, 21, 22, 24–27] and presented in section 2.2.3. These authors report increases in shear strength between 37% and 60% over their measured quasi-static values. A possible explanation for this higher increase is the maximum strain rate reported. The results presented by other authors correspond to a higher strain rate in the range of 100 to 1000 s^{-1} and the current analysis is limited to 69 s^{-1}.

In the performed experiments and presented here, the yield point is defined as the location in which the shear stress-strain curve crosses an offset 0.2% shear strain line parallel to the linear elastic region. The shear stress level at which this occurs is seen to increase from 35.4 MPa to 48.5 MPa (an increase of 37%) between slowest and fastest piston speeds. Several other authors mention a similar shift in yielding location [5, 12, 21, 22, 25, 26] but most of them do not report absolute values for this increase in yield stress. Only Koerber et al. [22] mention an increase in shear yield stress of 87% between quasi-static and a strain rate of 300 s^{-1}, which is a significantly larger increase than the one found and presented here (37%). The main reason for such difference might be related with the different resin systems used, since the strain rate dependency of different epoxies can be highly dissimilar.

The shear modulus, which is determined by fitting a linear regression in the strain range from 4000 to 8000 microstrain (from 0.4 to 0.8% shear strain) was found not to change significantly with increasing strain rate. Similar results had been presented by Staab and Gilat [24] who also found no variation in shear modulus. Other authors, such as Hsiao et al. [21] and Koerber et al. [22] found slight increases of 18% and 25%, respectively, in shear modulus between static and dynamic tests. On the other hand, Shokrieh and Omidi [25] reported a reduction of 12% in shear modulus. These results show some inconsistency in the variation of the shear modulus with increasing strain rate. Nonetheless, the increases and decrease reported are quite minimal and are associated with different epoxy systems used.

3.4.4.1 Prediction of longitudinal compression strength based on shear properties

In section 2.2.2.1, an explanation was presented to justify the increase in longitudinal compressive strength (in fibre direction) with increasing strain rate, given that carbon fibres are not strain rate dependent themselves. Budiansky and Fleck [19] and Daniel et al. [18] suggest that the longitudinal compressive strength of unidirectional laminates is intimately controlled by the matrix behaviour. What their models propose is that when the matrix locally reaches its yielding stress/strain, its stiffness drops, causing it to not be able to provide support for the fibres. This weakened support on the fibres leads to the occurrence of fibre microbuckling and consequent failure by creation of kink bands. The equation developed by Budiansky and Fleck [19] to predict the longitudinal compressive strength based on the laminate shear yield properties can be written as:

$$(\sigma_x)_{max} \approx \frac{\tau_y}{\phi^0 + \gamma_y} \tag{3.4}$$

Given the experimental tests performed with $[+45°/-45°]_{4s}$ layup specimens, equation (3.4) can be used to predict the longitudinal compressive strength at different strain rates. These predictions can then be compared with the experimental results obtained when testing rectangular specimens with a $[0°]_{16}$ layup to check how well the model of equation (3.4) performs at predicting the longitudinal strength at varying loading rates.

Firstly, the fibre misalignment of the unidirectional specimens must be found. This can be done by using results at similar strain rate levels of $[0°]_{16}$ and $[+45°/-45°]_{4s}$ layup specimens. As reported in section 3.4.2, the compression strength of $[0°]_{16}$ specimens subjected to a strain rate of $7.6 \times 10^{-3}\ s^{-1}$ averaged at 1288 MPa. Under a similar strain rate ($\dot{\varepsilon} = 6.2 \times 10^{-3}\ s^{-1}$), the specimens with a $[+45°/-45°]_{4s}$ layup yield at a shear stress of 35.4 MPa and a shear strain of 1.22%. Replacing these results back in equation (3.4):

$$1288 \approx \frac{35.4}{\phi^0 + 0.0122} \tag{3.5}$$

which results in an initial fibre misalignment for the unidirectional specimens of approximately 0.9°.

Making use of the yield shear stress and strain of $[+45°/-45°]_{4s}$ layup specimens at different strain rates presented in Figure 3.15 and Table 3.8, combined with the previously determined fibre misalignment $\phi^0 \approx 0.9°$, the compressive strength of unidirectional laminates can be predicted using equation (3.4). These results are plotted in Figure 3.16, together with the experimentally obtained compressive strength of $[0°]_{16}$ layup specimens presented previously in Table 3.6.

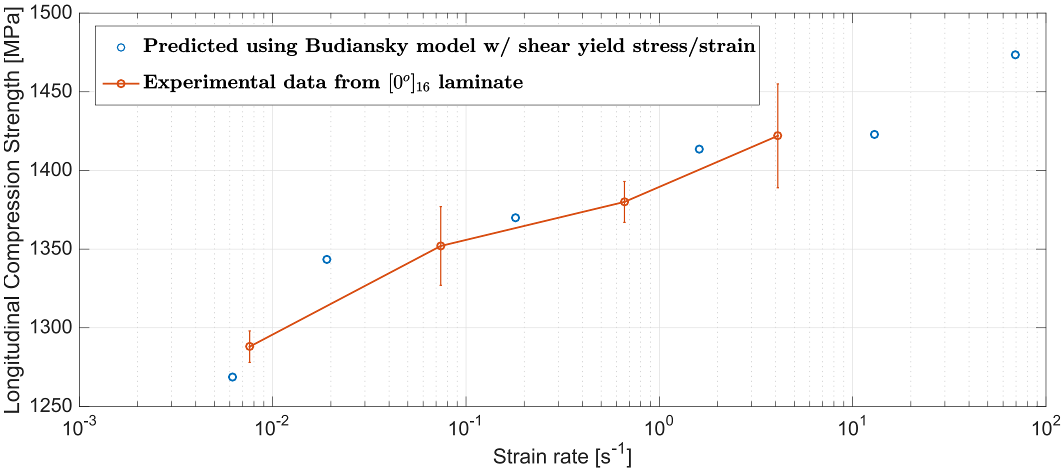

Figure 3.16: Comparison of longitudinal compressive strength results between experimental data and predicted by Budiansky's model.

The comparison presented in Figure 3.16 indicates that the model developed by Budiansky and Fleck [19] (equation 3.4), when used in combination with the shear yield properties of the laminate, slightly overestimates the experimental longitudinal compression strength. However, the increasing trend predicted by this model is in excellent agreement with the experimental growth over the strain rate range tested.

These results indicate that, using a proper initial fibre misalignment ϕ^0 (which can be more accurately determined by microscopic analysis), the growth in longitudinal compression strength with increasing strain rate can be correctly predicted without performing longitudinal tests on unidirectional laminates.

Furthermore, these results also prove that the increase observed in longitudinal compressive strength with varying loading rate is directly related with an increase in the laminate's shear properties, more specifically the shear yield stress and strain.

3.4.5 [0°/90°]$_s$ layup

The three previous subsections presented the tests with the layups necessary to determine and numerically implement how the main mechanical properties of the elementary ply behaves under different strain rates. However, it is important to verify if a similar behaviour is found when plies of different orientations are combined to create more complex layups and more commonly used in automotive applications. For this reason, specimens with a bi-axial $[0°/90°]_{4s}$ and a quasi-isotropic $[+45°/-45°/0°/90°]_{2s}$ were also tested.
In Figure 3.17 the stress-strain curves obtained for the bi-axial layup are presented, with the corresponding mechanical properties summarized in Table 3.9.

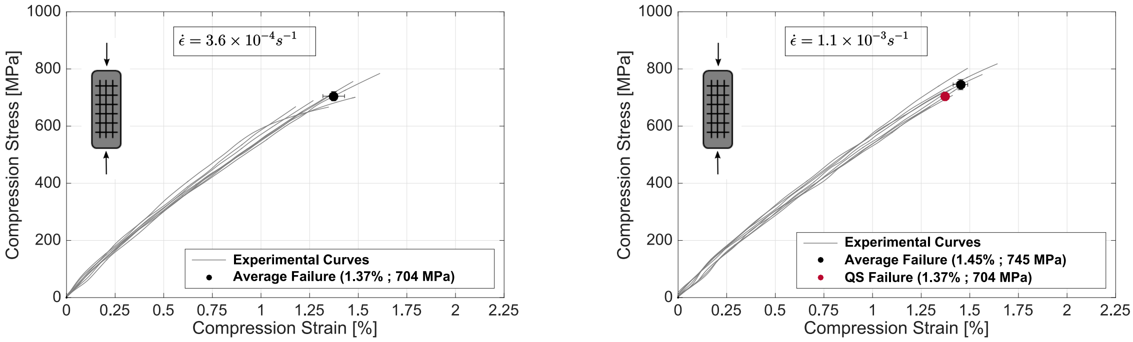

(a) Impactor Speed: $2\ mm/min$ **(b)** Impactor Speed: $6\ mm/min$

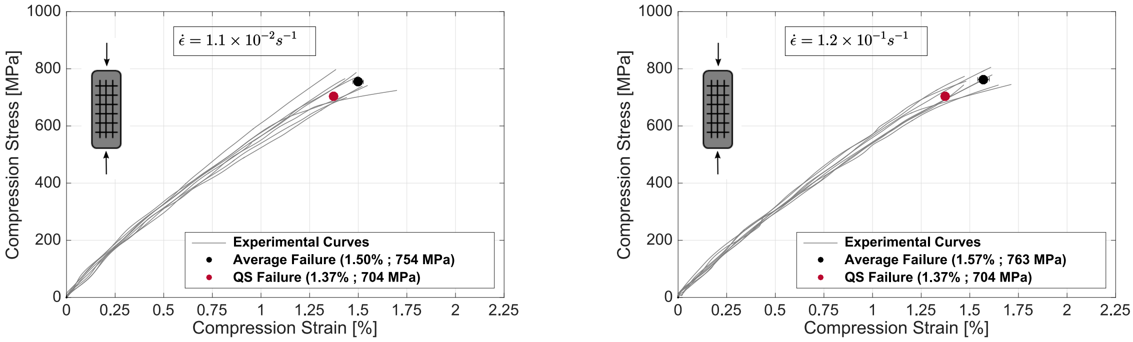

(c) Impactor Speed: $1\ mm/s$ **(d)** Impactor Speed: $10\ mm/s$

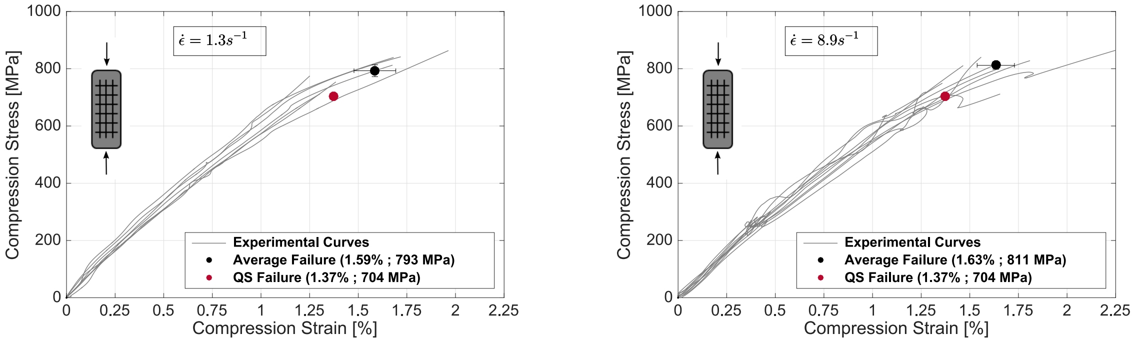

(e) Impactor Speed: $0.1\ m/s$ **(f)** Impactor Speed: $1\ m/s$

Figure 3.17: Stress-strain curves of $[0°/90°]_{4s}$ layup specimens at different impactor speeds.

Table 3.9: Averaged compression properties obtained for the bi-axial layup ($[0°/90°]_{4s}$) specimens at six different strain rates.

Strain Rate $\dot{\varepsilon}$ $[s^{-1}]$	Strength [MPa]	Fracture Strain [%]	Modulus [GPa]
$3.6 \pm 0.3 \times 10^{-4}$	704 ± 16	1.37 ± 0.06	62.9 ± 1.5
$1.1 \pm 0.1 \times 10^{-3}$	745 ± 18	1.45 ± 0.04	65.0 ± 1.7
$1.1 \pm 0.1 \times 10^{-2}$	754 ± 12	1.50 ± 0.03	67.1 ± 2.1
$1.2 \pm 0.1 \times 10^{-1}$	763 ± 10	1.57 ± 0.03	63.7 ± 1.1
1.3 ± 0.1	793 ± 21	1.59 ± 0.11	64.6 ± 2.3
8.9 ± 1.4	811 ± 13	1.63 ± 0.10	64.1 ± 2.9

The variation in mechanical compressive properties for the bi-axial layup ($[0°/90°]_{4s}$) is similar to the variation previously presented for the $[0°]_{16}$ layup specimens, because its response is dominated by the 0° plies.
Between quasi-static and dynamic tests at a strain rate of approximately 9 s^{-1}, the compressive strength increased by 15%, while the unidirectional specimens showed a 22% increase. A slightly smaller increase was also achieved for the failure strain: 19%, while the UD specimens increased by 26%.
Similarly to the $[0°]_{16}$ layup specimens, the stiffness of the $[0°/90°]_{4s}$ specimens also does not change with increasing strain rate.

A factor worth mentioning is the difference in fracture strain between the specimens with $[0°]_{16}$ and $[0°/90°]_{4s}$ layups. Even thought failure in both layups is predominantly driven by fibre microbuckling of the 0° plies, the specimens with a bi-axial layup have, on average, a 17.5% higher failure strain when compared with the unidirectional specimens loaded longitudinally. A possible explanation for this phenomenon is related with the lateral support that the 90° plies provide, which delays the occurrence of kink bands in the 0° plies. A more detailed analysis is presented further in section 3.4.7, in which the 0° plies are modelled as a beam under compression and the 90° plies as an elastic foundation offering lateral support.

3.4.6 $[+45°/\text{-}45°/0°/90°]_s$ layup

The mechanical response of a quasi-isotropic layup ($[+45°/-45°/0°/90°]_{2s}$) subjected to different loading rates is also investigated. Layups similar to this one represent the vast majority of the carbon-epoxy components used in the automotive industry. Therefore, it is critical to understand its behaviour experimentally, so that the numerical simulations can be properly correlated. Figure 3.18 displays the stress-strain curves obtained at different piston velocities, with the corresponding averaged mechanical compressive properties being documented in Table 3.10.

Once again, the increase in mechanical properties is very similar to what was previously reported for the $[0°]_{16}$ layup specimens, which indicates that the 0° plies also dominate the response of the specimens with this QI layup. Between quasi-static conditions and tests with a strain rate of 10 s^{-1}, the strength and fracture strain of the quasi-isotropic layup specimens increased by 20% and 19%, respectively. As expected, the stiffness is not affected by the

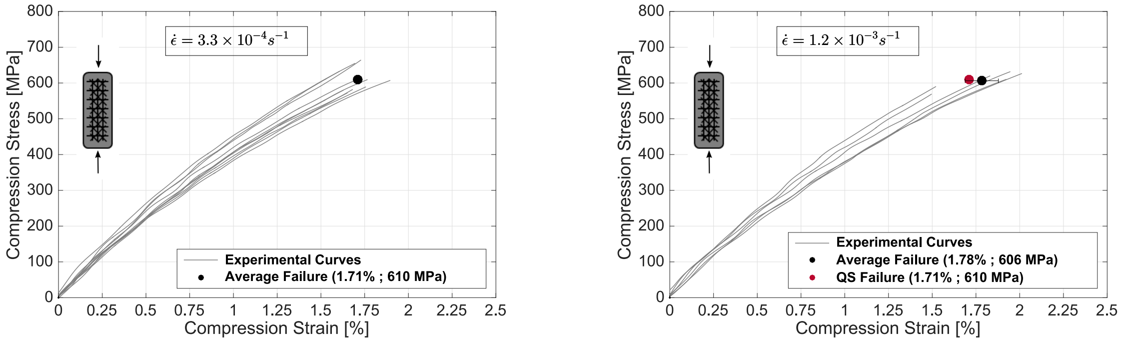

(a) Impactor Speed: $2\ mm/min$ **(b)** Impactor Speed: $6\ mm/min$

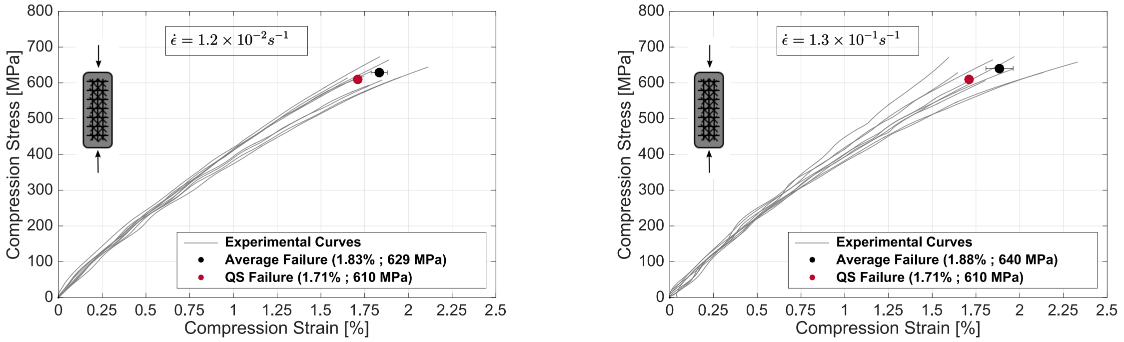

(c) Impactor Speed: $1\ mm/s$ **(d)** Impactor Speed: $10\ mm/s$

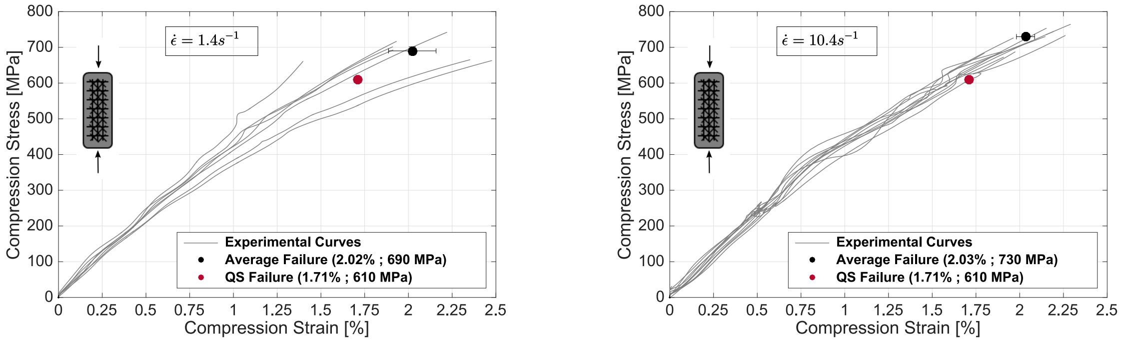

(e) Impactor Speed: $0.1\ m/s$ **(f)** Impactor Speed: $1\ m/s$

Figure 3.18: Stress-strain curves of $[+45°/-45°/0°/90°]_{2s}$ layup specimens at different impactor speeds.

loading rate.

Likewise, the fracture strain of the quasi-isotropic layup specimens is significantly higher than the fracture strain reported for the unidirectional specimens loaded longitudinally. On average, the 0° plies within the quasi-isotropic layup tend to form kink bands at a compressive strain 45% higher than when located together with other 0° plies on an unidirectional laminate.

As mentioned previously, a detailed analysis on the buckling of 0° plies inside different layups is presented in section 3.4.7.

Table 3.10: Averaged compression properties obtained for the quasi-isotropic layup ($[+45°/-45°/0°/90°]_{2s}$) specimens at six different strain rates..

Strain Rate $\dot{\varepsilon}$ $[s^{-1}]$	Strength [MPa]	Fracture Strain [%]	Modulus [GPa]
$3.3 \pm 0.2 \times 10^{-4}$	610 ± 10	1.71 ± 0.02	48.2 ± 1.5
$1.2 \pm 0.1 \times 10^{-3}$	606 ± 10	1.78 ± 0.10	44.6 ± 1.2
$1.2 \pm 0.1 \times 10^{-2}$	629 ± 9	1.83 ± 0.05	45.7 ± 1.4
$1.3 \pm 0.1 \times 10^{-1}$	640 ± 9	1.88 ± 0.08	49.2 ± 2.1
1.4 ± 0.2	690 ± 11	2.02 ± 0.14	46.3 ± 1.6
10 ± 1	730 ± 8	2.03 ± 0.05	50.9 ± 3.3

3.4.7 Elastic foundation

Assuming that the 0° plies can be modelled as a beam under compression subject to buckling and that the adjacent off-axis plies providing lateral support are treated as an elastic foundation (see Figure 3.19), then a general buckling analysis can be performed.

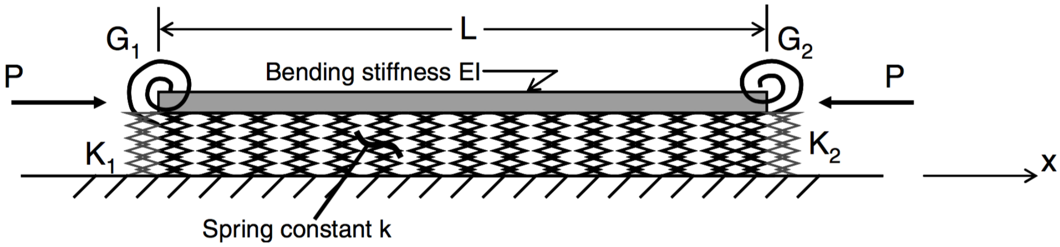

Figure 3.19: Beam under compression on a one-sided elastic foundation [51].

The general differential equation for the axis of a loaded beam:

$$\frac{d^4w}{dx^4} + \frac{P}{EI}\frac{d^2w}{dx^2} = \frac{q}{EI} \tag{3.6}$$

where w is the beam's out-of-plane displacement, x is the coordinate along the beam's axis, P is the applied longitudinal force and q is the lateral load. For a case of pure compression, equation (3.6) becomes:

$$\frac{d^4w}{dx^4} + \frac{P}{EI}\frac{d^2w}{dx^2} = 0 \tag{3.7}$$

which is a fourth order homogeneous differential equation with the general solution in the form of:

$$w(x) = C_1\cos(\lambda x) + C_2\sin(\lambda x) + C_3x + C_4 \tag{3.8}$$

where C_1, C_2, C_3 and C_4 are constants, and $\lambda = \sqrt{P/EI}$.
Assuming fixed ends on both extremities of the beam, which means that in Figure 3.19 $K_1 = K_2 = G_1 = G_2 = \infty$ the boundaries conditions are:

$$\begin{cases} w_{x\ =\ 0,L} = 0 \\ \\ \left(\dfrac{dw}{dx}\right)_{x\ =\ 0,L} = 0 \end{cases} \tag{3.9}$$

From the four previous boundary conditions, the following system of equations arises:

$$\begin{cases} C_1 + C_4 = 0 \\ C_1 \cos(\lambda L) + C_2 \sin(\lambda L) + C_3 L + C_4 = 0 \\ C_2 \lambda + C_3 = 0 \\ -C_1 \lambda \sin(\lambda L) + C_2 \lambda \cos(\lambda L) + C_3 = 0 \end{cases} \tag{3.10}$$

which can be written in a matrix form:

$$\begin{bmatrix} 1 & 0 & 0 & 1 \\ \cos(\lambda L) & \sin(\lambda L) & L & 1 \\ 0 & \lambda & 1 & 0 \\ -\lambda \sin(\lambda L) & \lambda \cos(\lambda L) & 1 & 0 \end{bmatrix} \begin{bmatrix} C_1 \\ C_2 \\ C_3 \\ C_4 \end{bmatrix} = 0 \tag{3.11}$$

The trivial solution is $[C_1\ C_2\ C_3\ C_4] = 0$, which is related with the pre-buckling shape of the beam, and the non-trivial solution requires the determinant of the left-hand side matrix to be 0.

$$\begin{vmatrix} 1 & 0 & 0 & 1 \\ \cos(\lambda L) & \sin(\lambda L) & L & 1 \\ 0 & \lambda & 1 & 0 \\ -\lambda \sin(\lambda L) & \lambda \cos(\lambda L) & 1 & 0 \end{vmatrix} = 0 \tag{3.12}$$

which yields:

$$2\lambda\Big(1 - \cos(\lambda L)\Big) = \lambda^2 L \sin(\lambda L) \tag{3.13}$$

with the solution being:

$$\lambda = \frac{2m\pi}{L} \tag{3.14}$$

where m is an integer.
The solution for the out-of-plane displacement w (equation 3.8) then becomes:

$$w(x) = C_1 \cos\left(\frac{2\pi m}{L}x\right) - C_1 \tag{3.15}$$

According to Kassapoglou [51], the one-dimensional energy expression for the beam with an elastic foundation is:

$$\Pi_c = \frac{1}{2}\int_0^L EI\left(\frac{d^2w}{dx^2}\right)^2 dx + \frac{1}{2}\int_0^L (-P)\left(\frac{dw}{dx}\right)^2 dx + \frac{1}{2}\int_0^L kw^2 dx \tag{3.16}$$

where k is the stiffness of the elastic foundation and has units of force per unit area.
The first term on the right-hand side of equation (3.16) is related with the potential energy stored due to bending of the beam and using the solution shown in equation (3.15) for w to carry out the derivation and integration, this term becomes:

$$\frac{1}{2}\int_0^L EI\left(\frac{d^2w}{dx^2}\right)^2 dx = \frac{4EIC_1^2\pi^4 m^4}{L^3} \tag{3.17}$$

The second term on the right-hand side of equation (3.16) is the work performed by the external compressive load P, which can be simplified to:

$$\frac{1}{2}\int_0^L (-P)\left(\frac{dw}{dx}\right)^2 dx = -\frac{PC_1^2 m^2\pi^2}{L} \tag{3.18}$$

Finally, the third term on the right-hand side of equation (3.16) has to do with the potential energy stored in the elastic (spring) foundation:

$$\frac{1}{2}\int_0^L kw^2 dx = \frac{3}{4}C_1^2 kL \tag{3.19}$$

Replacing equations (3.17), (3.18) and (3.19) back into equation (3.16),

$$\Pi_c = \frac{4EIC_1^2\pi^4 m^4}{L^3} - \frac{PC_1^2 m^2\pi^2}{L} + \frac{3}{4}C_1^2 kL = C_1^2\left[\frac{4EI\pi^4 m^4}{L^3} - \frac{Pm^2\pi^2}{L} + \frac{3}{4}kL\right] \tag{3.20}$$

To find the critical buckling load, the total energy Π_c has to be minimized with respect to the unknown C_1:

$$\frac{\partial \Pi_c}{\partial C_1} = 0 \implies 2C_1\left[\frac{4EI\pi^4 m^4}{L^3} - \frac{P_{crit} m^2\pi^2}{L} + \frac{3}{4}kL\right] = 0 \tag{3.21}$$

which has the following solutions:

$$\begin{cases} C_1 = 0, \quad \text{trivial solution} \\ \\ \dfrac{4EI\pi^4 m^4}{L^3} - \dfrac{P_{crit} m^2 \pi^2}{L} + \dfrac{3}{4} kL = 0, \quad \text{non-trivial solution} \end{cases} \tag{3.22}$$

Taking the non-trivial solution and solving for P_{crit}:

$$P_{crit} = \frac{4EI\pi^2 m^2}{L^2} + \frac{3}{4}\frac{kL^2}{m^2\pi^2} \tag{3.23}$$

For the case without a lateral elastic foundation, equation (3.23) becomes the typical Euler buckling load for a case with a beam fixed on both ends:

$$(P_{crit})_{k=0} = \frac{4EI\pi^2}{L^2} \tag{3.24}$$

which, in the current analysis, is the case of compression testing of [0°] laminate, since there are no off-axis plies providing lateral support.

For a general case with a lateral elastic foundation, the critical load can be normalized by the critical load when $k = 0$:

$$\frac{(P_{crit})_{k>0}}{(P_{crit})_{k=0}} = \frac{\frac{4EI\pi^2 m^2}{L^2} + \frac{3}{4}\frac{kL^2}{m^2\pi^2}}{\frac{4EI\pi^2}{L^2}} = m^2 + \frac{3}{16}\frac{kL^4}{EI\pi^4 m^2} \tag{3.25}$$

Assuming that the 0° plies, which are being modelled as a beam under compression subject to buckling, behave in a similar fashion when in a [0°], $[0°/90°]_s$ and $[+45°/-45°/0°/90°]_s$ laminates, i.e. the modulus of the 0° ply is the same and its response is linear until failure, then (3.25) can be written in terms of failure strains, instead of failure loads:

$$\frac{(P_{crit})_{k>0}}{(P_{crit})_{k=0}} = \frac{(\varepsilon_{fail})_{k>0}}{(\varepsilon_{fail})_{k=0}} = m^2 + \frac{3}{16}\frac{kL^4}{EI\pi^4 m^2} \tag{3.26}$$

Out of all the laminates tested and presented in section 3.4, three of them contained 0° plies:

- $[0°]_{16}$ laminate, in which the 0° plies do not have any lateral support and can be modelled under the current analysis as $k = 0$.
- $[0°/90°]_{4s}$ laminate, in which the outer 0° plies only have one-sided support by a 90° ply. Under the current analysis, the outer 0° plies of this laminate can be modelled as a beam under compression with lateral support on one side only.
- $[+45°/-45°/0°/90°]_{2s}$ laminate, in which the 0° plies are supported on both sides by layers of other orientations. Therefore, the 0° plies can be modelled as a beam under compression subjected to buckling with lateral elastic support on both sides.

Table 3.11: Compression strain (in %) at failure for three laminates containing $0°$ plies at different strain rates.

Strain Rate ($\dot{\varepsilon}$) $[s^{-1}]$	$[0°]_{16}$ laminate	$[0°/90°]_{4s}$ laminate	$[+45°/-45°/0°/90°]_{2s}$ laminate
2.3×10^{-4} to 3.6×10^{-4}	1.15	1.37	1.71
7.2×10^{-4} to 1.2×10^{-3}	1.18	1.45	1.78
7.6×10^{-3} to 1.2×10^{-2}	1.29	1.50	1.83
7.4×10^{-2} to 1.3×10^{-1}	1.33	1.57	1.88
6.6×10^{-1} to 1.4	1.36	1.59	2.02
4.1 to 10.4	1.45	1.63	2.03

Table 3.11 summarizes the averaged compression strain at failure obtained from the experimental tests for each of the 3 laminates under different strain rates.

Since the maximum ratio of failure strain between the case with support on both sides and the case without any support is approximately 1.5, then m in equation (3.26) must be 1. If m took any integer value larger than 1, then the solution for the elastic spring constant k would be negative, which is physically not possible. Therefore, equation (3.26) can be rewritten as:

$$\frac{(\varepsilon_{fail})_{k>0}}{(\varepsilon_{fail})_{k=0}} - 1 = \frac{3}{16}\frac{kL^4}{EI\pi^4} \implies \left[\frac{(\varepsilon_{fail})_{k>0}}{(\varepsilon_{fail})_{k=0}} - 1\right]\frac{16\pi^4}{3} = \frac{kL^4}{EI} \tag{3.27}$$

For both laminates containing $0°$ plies that have lateral support from plies with other orientations, the value of $kL^4/(EI)$ can be determined by comparing the failure strain with the case without any side support (left-hand side of equation 3.27). These results are summarized in Table 3.12.

Table 3.12: Comparison of the lateral elastic foundation constant k between the two laminates tested.

Strain Rate ($\dot{\varepsilon}$)	$\frac{kL^4}{EI}$ [-]	
$[s^{-1}]$	$[0°/90°]_{4s}$	$[+45°/-45°/0°/90°]_{2s}$
2.3×10^{-4} to 3.6×10^{-4}	99.39	253.0
7.2×10^{-4} to 1.2×10^{-3}	118.9	264.2
7.6×10^{-3} to 1.2×10^{-2}	84.57	217.5
7.4×10^{-2} to 1.3×10^{-1}	93.75	214.8
6.6×10^{-1} to 1.4	87.86	252.1
4.1 to 10.4	64.49	207.8

Assuming that the length L and the bending stiffness EI of a $0°$ ply take similar values for both laminates, then a direct comparison can be performed. As expected, the laminate with plies supporting the $0°$ on both sides (the $[+45°/-45°/0°/90°]_{2s}$ laminate) has a higher value of k, the constant of the lateral foundation. One would expect that the laminate providing support on both sides would have a k, on average, that is double the value of the laminate

providing only one-sided support, since a similar analysis can be performed simply by adding another spring of constant k to the other side of the beam in Figure 3.19.
However, on average, the laminate providing double-sided support has a value of k that is 2.5 times larger than the k value of the laminate giving one-sided support. This difference can arise from the fact that the ±45° plies of the second laminate might be able to give an improved support, when compared to a 90° ply. This different orientation of the side layers and also the fact that on the second laminate the 0° ply is two layers away from the laminate surface can explain the fact that the increase in k is by a factor of 2.5 instead of the expected value of 2.
Nonetheless, the current analysis yields results agreeable with the experimental data and can be considered a fairly simple, yet decent clarification for the increase in compression strain at failure for the different laminates containing 0° plies.

3.5 Test results: omega-profile structural component

As mentioned previously, a special focus is placed on the determination of how the strain rate dependent properties of CFRP composites develop from experiments on simple material coupon specimens into a structural component with a more complex shape. For this reason, additional experimental crash tests were performed on omega-profile specimens, whose shape is similar to several structural components used in the automotive industry, such as in long axially loaded beams/pillars. Figure 3.20 contains a sketch of the profile's geometry axially loaded in compression.
The chosen layup for these specimens was $[+45°/-45°/+45°/-45°/0°/90°]_s$, where the 0° is the longitudinal direction of the profile - aligned with the applied load.

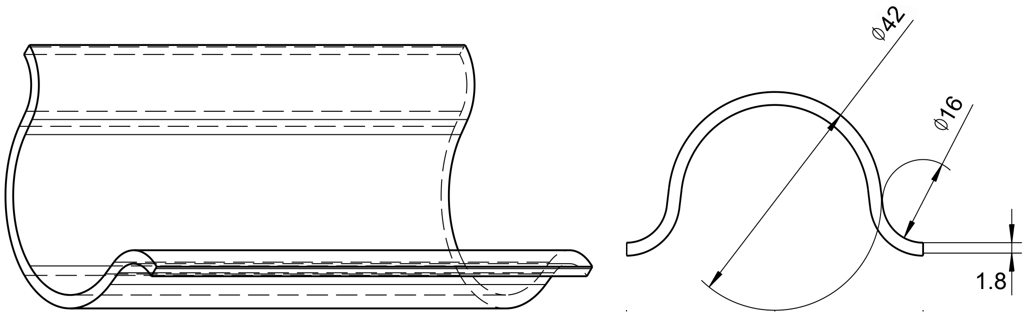

(a) Isometric view.

(b) Cross-section view (dimensions in mm).

Figure 3.20: Drawing of the Omega-profile component.

Three testing speeds were chosen for the crash tests on the omega-profile specimens: the typical quasi-static speed of 2 mm/min, the maximum velocity achievable with the cameras (1 m/s) and an intermediate speed of 0.01 $m/s = 10\ mm/s$. Figure 3.21 presents the resulting graphs containing the compression force as function of the piston displacement after impact for three replicates at each of the three selected impactor speeds. The averaged resulting strain rate, maximum load and strain at failure are summarized in Table 3.13.

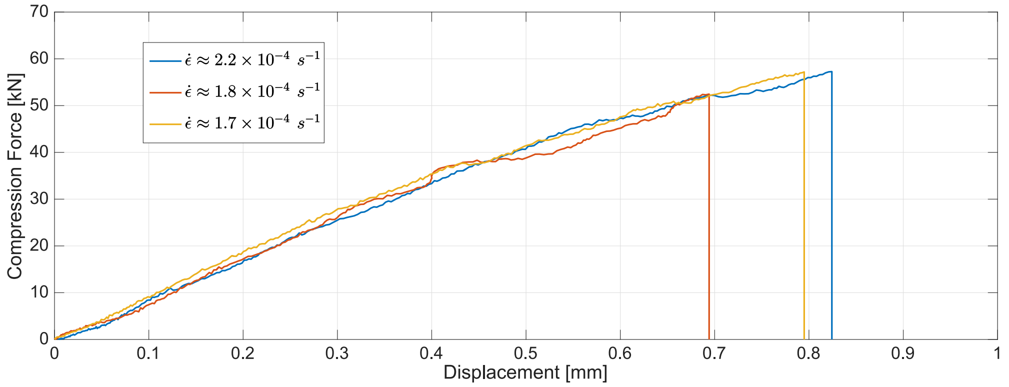

(a) Impactor Speed: $2\ mm/min$

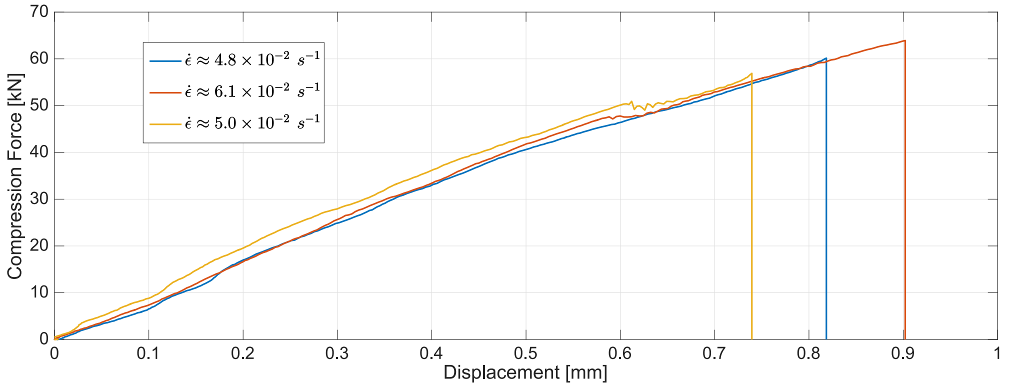

(b) Impactor Speed: $10\ mm/s$

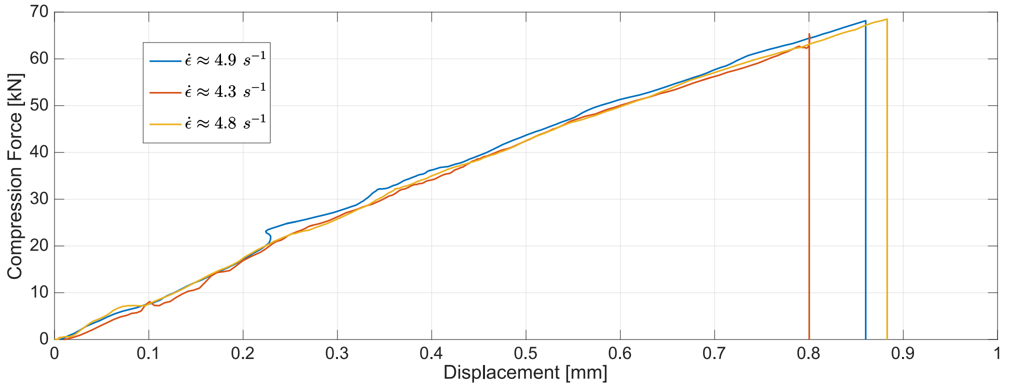

(c) Impactor Speed: $1\ m/s$

Figure 3.21: Force-displacement plots of experimental crash tests on omega-profile specimens at three different impactor speeds.

It is important to note that in Figure 3.21, the piston displacement after impact (X-axis) is not consistent with the trend of increasing force. It would be expected that the piston displacement at failure increased with increasing impactor speed, since higher strain rates lead to higher failure strains. However, the displacement is measured on the fixture top clamp using the DIC software to track its movement, and due to limitations of the fixture, the specimens were able to slightly move vertically inside the fixing jaws. This meant that the tracked

Table 3.13: Averaged strain rate, maximum load and failure strain for the axially loaded omega-profile at three different impactor velocities.

Impactor velocity $[m/s]$	Strain rate ($\dot{\varepsilon}$) $[s^{-1}]$	Maximum load $[kN]$	Strain at failure $[\%]$
3.3×10^{-5}	$1.9 \pm 0.2 \times 10^{-4}$	55.6 ± 1.6	1.21 ± 0.06
1×10^{-2}	$5.3 \pm 0.4 \times 10^{-2}$	60.3 ± 2.0	1.34 ± 0.07
1	4.7 ± 0.2	67.3 ± 1.0	1.42 ± 0.03

fixture displacement after impact does not translate directly into a variation of length on the specimen.

As shown in Table 3.13, both the strength (directly related with the maximum load) and the failure strain increase with increasing strain rate. From quasi-static to tests with an impactor velocity of 1 m/s, the strength increased by 21% and the failure strain by 17%.
These results are in very good agreement with the increase in strength found on $[0°]_{16}$ layup specimens presented in section 3.4.2, where an increase in compression strength of 22% was found for a similar strain rate range.
However, there is a slight discrepancy for the increase in fracture strain. In section 3.4.2, the $[0°]_{16}$ layup specimens showed an increase of 26%, while in the compression tests of the omega-profile an increase of 17% of failure strain was found for a similar strain rate range.

Failure during crash tests of multi-directional omega-profile specimens occurs suddenly and without a drop in stiffness before failure, indicating that failure is dominated by fibre microbuckling in the 0° plies, which are the main load-carrying plies. Figure 3.22 shows the sudden and abrupt failure in an omega-profile specimen subjected to an impactor velocity of 1 m/s. Failure occurs in the center of the specimen's 60 mm length between top and bottom clamps. As soon as the specimen fails - Figure 3.22 **(c)** - the load signal drops immediately from its peak position to zero.

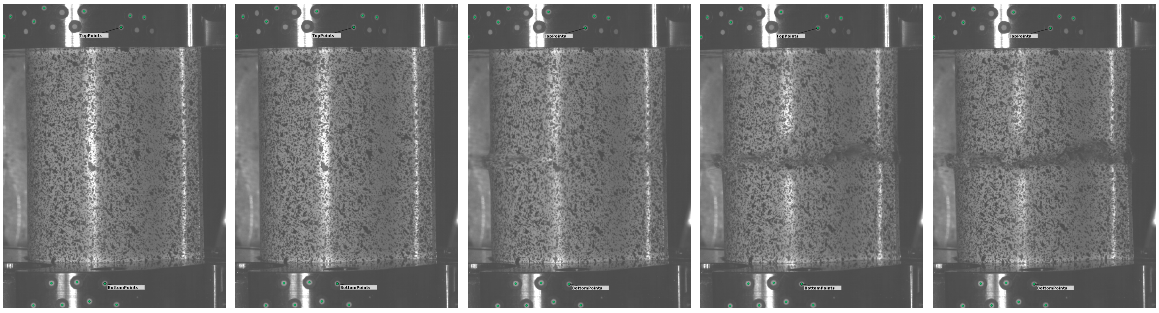

(a) t_0 **(b)** $t_0 + 25\ \mu s$ **(c)** $t_0 + 50\ \mu s$ **(d)** $t_0 + 75\ \mu s$ **(e)** $t_0 + 100\ \mu s$

Figure 3.22: Failure progression on omega-profile specimen during a time period of 0.1 ms at an impact velocity of 1 m/s.

Following the analysis on the occurrence of fibre microbuckling presented in section 3.4.7,

the layup of the omega-profile specimens ($[+45°/-45°/+45°/-45°/0°/90°]_s$) falls in the same category as the case of the $[+45°/-45°/0°/90°]_{2s}$ layup specimens, i.e. the 0° plies are supported on both sides by 90° and −45° orientation plies. However, the failure strain achieved during compression testing of the omega-profile specimens is relatively smaller than on the $[+45°/-45°/0°/90°]_{2s}$ layup material coupons.
A plausible explanation for the reduced fracture strain is related with the manufacturing defects. While the material coupons tested in section 3.4.5 were hand-laid as flat plates and contain extremely few manufacturing defects, the omega-profile specimens were hand-laid on a female mould with a curved shape containing a relatively small radius, thus very prone to the occurrence of defects, such as small wrinkles in certain plies and higher fibre misalignment.

3.6 Summary and Conclusions

In this chapter, the results from all the experimental compression tests on carbon-epoxy specimens were presented. The experimental tests were performed using a combined load introduction fixture (both shear and end loading), a servo-hydraulic testing machine with piston velocities up to 1 m/s and recorded using high-speed cameras for subsequent strain analysis using DIC software.
However, before evaluating the effect of the strain rate on the laminate mechanical properties, a study on the influence of the rectangular specimens geometrical factors was performed. The effect of the specimen thickness, width, gauge length, and the GFRP tab taper angle was investigated through a series of tests on unidirectional specimens with varying geometries at quasi-static testing conditions. From this analysis, an optimal specimen geometry was derived, based on the criterion of maximal compression strength. This analysis was shown in section 3.3.

With a fixed specimen geometry, an exhaustive series of tests with five different laminate layups subjected to six compression velocities was carried out.
For the longitudinal unidirectional ($[0°]_{16}$ layup) specimens, the increase found in compression strength and failure strain is linear on a logarithmic strain rate scale. Between QS conditions ($\dot{\varepsilon} = 2.3 \times 10^{-4}\ s^{-1}$) and the highest loading rate achieved ($\dot{\varepsilon} = 4\ s^{-1}$) the compression force needed to cause failure increased by 22%. Similarly, the strain at failure also increased in a similar trend, revealing a 26% growth. The longitudinal compressive modulus registered no significant change in the strain rate range tested.
The tests performed in a direction transverse to the fibres ($[90°]_{16}$ layup specimens) reveal a significant increase in yield and ultimate stress. Both these properties increased by 56% between slow ($\dot{\varepsilon} = 2.9 \times 10^{-3}\ s^{-1}$) and highly dynamic ($\dot{\varepsilon} = 68\ s^{-1}$) tests. The transverse fracture strain and modulus exhibit no significant variation in the strain rate range tested, as these properties are kept approximately constant at 5.2% and 8.4 GPa, respectively.
The evolution of the shear properties with varying strain rate was also investigated by performing compression tests on specimens with a $[+45°/-45°]_{4s}$ layup. The shear yield stress and maximum stress (corresponding to the shear stress when the shear strain reaches 5%) increased by 37% and 27%, respectively, between strain rates of $\dot{\varepsilon} = 6.2 \times 10^{-3}\ s^{-1}$ and $\dot{\varepsilon} = 69\ s^{-1}$. As was the case with the longitudinal and transverse moduli, the shear modulus also does not suffer a significant change in the range of loading rates tested.
Overall, the mechanical properties in a matrix-dominated direction get more brittle, i.e.

higher strength and delayed yield, but not stiffer as the moduli are constant over the entire range of strain rates. In fibre direction, the laminate's response also keeps its stiffness, but failure (fibre microbuckling) occurs at higher strain levels, which leads to higher strengths. This increase in longitudinal failure strain with increasing strain rate is directly related with the increase in matrix properties, as the matrix is the constituent providing lateral support to the fibres and preventing them from buckling.
These results were presented in section 3.4.

Rectangular specimens with two additional layups ($[0°/90°]_{4s}$ and $[+45°/-45°/0°/90°]_{2s}$) were also tested to study how the 0° plies behave when subjected to varying strain rates while being embedded in multidirectional laminates. It was found that the dynamic strength and failure strain of specimens with these two layups increased by $15-20\%$ and 19%, respectively, over the respective quasi-static values. These growths were found to be in line with the increase achieved for specimens with a $[0°]_{16}$ layup.
An additional aspect worth mentioning is the overall higher failure strain in multidirectional laminates, when compared to the $[0°]_{16}$ layup specimens. This feature was analysed in section 3.4.7, in which a buckling analysis of 0° plies was performed, by modelling the off-axis plies as lateral elastic foundations. This investigation concluded that on the laminate in which the 0° plies are supported on both sides by off-axis plies ($[+45°/-45°/0°/90°]_{2s}$), the lateral elastic support is approximately 2.5 times of that found in the case of 0° plies supported only on one side ($[0°/90°]_{4s}$).

A significant aim of the current work was also to study how the strain rate dependent properties detected on rectangular specimens would develop when testing more complex shape components. Thus, compressive tests under three different piston velocities were performed on specimens with an omega-profile section and a $[+45°/-45°/+45°/-45°/90°/0°]_s$ layup. A particular attention was placed on maintaining the testing conditions very much alike with the tests performed previously on rectangular specimens, by using the same matrix-fibre combination, same curing cycle and a similar fixture/clamping of the specimen.
Between crash tests performed at QS speeds and highly dynamic (piston velocity of 1 m/s), the force at which the omega-profile specimen fails increased from 55.6 to 67.3 kN, which represents a growth of 21%. In a similar fashion, the strain at failure increased by 17%. These results are in very good agreement with the previously obtained for rectangular specimens with a quasi-isotropic layup ($[+45°/-45°/0°/90°]_{2s}$), where the increase in strength and failure strain was 20% and 19%, respectively, over a similar strain rate range.
It can be concluded that the strain rate dependency identified on simple rectangular specimens is very similar to the dependency found on components with a more complex shape. Therefore, these varying mechanical properties with increasing loading rate can be determined in simple rectangular specimens and directly applied on the analysis of structural components with multiple shapes, without leading to significant overestimations.

Chapter 4

Numerical Simulations

This chapter contains the implementation of the carbon-epoxy laminate strain rate dependent properties in a simulation material card and the results of the simulations performed at various velocities. Section 4.1 presents the basic properties of the simulation model used, together with the implementation of the strain rate dependent properties. In section 4.2, the implemented material card is calibrated and validated using a one-element model, through a series of simulations performed with layups and strain rates analogous to the experimental tests from which the material properties were extracted. Finally, section 4.3 presents the results of the crash simulations ran with a typical structural component used on the automotive industry and compares its behaviour with the experimental data of the previous chapter.

4.1 Model Description

The simulations of the present work were carried out with the commercially available explicit finite element software Pam-Crash®. The laminate was modelled using Mindlin plate theory shell elements previously implemented in the software's code.

The ply mechanics are based on a continuum damage mechanics approach proposed by Ladeveze and Le Dantec [52]. In the used model, the individual ply is modelled as an homogeneous orthotropic elastic material, subjected to damage that progressively decreases its properties. The coordinate system is defined such that the 1-direction coincides with the fibre direction, the 2-direction is perpendicular to the fibres within the plane of the ply, and the 3-direction is normal to the plane of the unidirectional ply.

Matrix damage

Two scalar factors are defined to model the elastic damaging behaviour of the matrix: d_{22} is related with the matrix micro-cracking parallel to the fiber direction and d_{12} has to do with the damage associated with the debonding between fibres and matrix. Both these damage variables take values in the interval from 0 to 1.

Given the plane stress condition assumed by the Mindlin plate theory, the compliance matrix containing the effect of matrix damage can be written as:

$$S = \begin{bmatrix} \frac{1}{E_1} & \frac{-\nu_{12}}{E_1} & 0 \\ \frac{-\nu_{12}}{E_1} & \frac{1}{E_2(1-d_{22})} & 0 \\ 0 & 0 & \frac{1}{G_{12}(1-d_{12})} \end{bmatrix} \tag{4.1}$$

from which, the damaged strain energy density can then be expressed as:

$$u = \frac{1}{2}\boldsymbol{\sigma}^{\boldsymbol{T}} S \boldsymbol{\sigma} \quad \text{where} \quad \boldsymbol{\sigma}^{\boldsymbol{T}} = [\sigma_{11} \;\; \sigma_{22} \;\; \sigma_{12}] \tag{4.2}$$

which becomes:

$$u = \frac{1}{2}\left[\frac{(\sigma_{11})^2}{E_1} - \frac{2\nu_{12}\sigma_{11}\sigma_{22}}{E_1} + \frac{(\sigma_{22})^2}{E_2(1-d_{22})} + \frac{(\sigma_{12})^2}{G_{12}(1-d_{12})}\right] \tag{4.3}$$

However, in (4.3) the term with d_{22} has to be split in a tension and a compression case, since if σ_{22} is negative, the matrix microcracks parallel to the fibres close and there is no reduction of E_2:

$$u = \frac{1}{2}\left[\frac{(\sigma_{11})^2}{E_1} - \frac{2\nu_{12}\sigma_{11}\sigma_{22}}{E_1} + \frac{\langle\sigma_{22}\rangle_+^2}{E_2(1-d_{22})} + \frac{\langle\sigma_{22}\rangle_-^2}{E_2} + \frac{(\sigma_{12})^2}{G_{12}(1-d_{12})}\right] \tag{4.4}$$

where $\langle\sigma_{22}\rangle_+$ and $\langle\sigma_{22}\rangle_-$ are defined as:

$$\langle\sigma_{22}\rangle_+ = \begin{cases} \sigma_{22} & \text{if} \quad \sigma_{22} \geqslant 0 \\ 0 & \text{if} \quad \sigma_{22} < 0 \end{cases} \qquad \text{and} \quad \langle\sigma_{22}\rangle_- = \begin{cases} \sigma_{22} & \text{if} \quad \sigma_{22} \leqslant 0 \\ 0 & \text{if} \quad \sigma_{22} > 0 \end{cases} \tag{4.5}$$

The strain components are then taken from:

$$\boldsymbol{\varepsilon} = \frac{\partial u}{\partial \boldsymbol{\sigma}} = S\boldsymbol{\sigma} \tag{4.6}$$

which results in:

$$\varepsilon_{11} = \frac{\sigma_{11} - \nu_{12}\sigma_{22}}{E_1} \tag{4.7a}$$

$$\varepsilon_{22} = \frac{\langle\sigma_{22}\rangle_+}{E_2(1-d_{22})} + \frac{\langle\sigma_{22}\rangle_-}{E_2} - \frac{\nu_{12}\sigma_{11}}{E_1} \tag{4.7b}$$

$$\gamma_{12} = \frac{\sigma_{12}}{G_{12}(1-d_{12})} \tag{4.7c}$$

The quantities that drive crack propagation are called ‘damage functions’, which are analogous to the commonly used energy release rates. The two damage functions, one for each damage parameter, are defined as:

$$Z_{12} = \frac{\partial u}{\partial d_{12}} = \frac{(\sigma_{12})^2}{2G_{12}(1-d_{12})^2} \tag{4.8a}$$

$$Z_{22} = \frac{\partial u}{\partial d_{22}} = \frac{\langle\sigma_{22}\rangle_+^2}{2E_2(1-d_{22})^2} \tag{4.8b}$$

Two additional parameters, which represent the evolution of the damage functions, are defined:

$$Y_{12}(t) = \max_{\tau \leqslant t} \sqrt{Z_{12}(\tau) + bZ_{22}(\tau)} \tag{4.9a}$$

$$Y_{22}(t) = \max_{\tau \leqslant t} \sqrt{Z_{22}(\tau)} \tag{4.9b}$$

where the parameter b was introduced to take into account coupling between tension in the transverse direction and shear.

In equation (4.9), the maximum (max) operator was introduced because the evolution of the damage functions must be based on the maximum value that the damage functions reached in a previous load cycle. This makes sure that there is no healing of the material during unloading. Damage is kept constant until the damage functions reach a new maximum.

Furthermore, the square-root operator is based on experimental data of unidirectional laminates and ensures a more realistic evolution of the damage functions.

For the evolution of the shear damage factor, an exponential function is used:

$$d_{12} = \begin{cases} d_{12,\lim}\left(1 - e^{\frac{Y_{12,0}-Y_{12}(t)}{Y_{12,crit}}}\right) & \text{if} \quad Y_{12}(t) \geqslant Y_{12,0} \\ 0 \quad \text{if} \quad Y_{12}(t) < Y_{12,0} \end{cases} \tag{4.10}$$

where $d_{12,\lim}$ is the maximum allowed value of the shear damage, $Y_{12,0}$ is the value of Y_{12} at which matrix shear damage initiates, and $Y_{12,crit}$ is the critical value of Y_{12} at which the matrix fails due to shear damage. The values of $d_{12,\lim}$, $Y_{12,0}$, $Y_{12,crit}$ and b were previously determined via a series of cyclic tension tests on specimens with $[\pm 45°]_s$ and $[+45°]$ layups, and simple tension tests on specimens with $[\pm 67.5°]_s$ layup specimens with the same fibre-matrix system as used in this work.

The evolution function for the transverse matrix damage was determined experimentally and directly implement into the solver as a series of points for both d_{22} and Y_{22}.

To determine the plastic strain in the matrix, a yield function based on the general anisotropic plasticity criterion proposed by Hill is implemented:

$$f(\boldsymbol{\sigma}, R) = \sqrt{\left[\frac{\sigma_{12}}{(1-d_{12})}\right]^2 + a^2\left[\frac{\langle\sigma_{22}\rangle_+}{(1-d_{22})} + \langle\sigma_{22}\rangle_-\right]^2} - R(\varepsilon^p) \tag{4.11}$$

where f is the yield function, a^2 is a coupling factor between shear and transverse matrix plastic strains which usually is equal to 0.33 for resin based materials, and $R(\varepsilon^p)$ is the stress after yielding and is defined using Ludwik's hardening law:

$$R(\varepsilon^p) = R_0 + \eta(\varepsilon^p)^n \tag{4.12}$$

in which R_0 is the yield stress, η and n are the hardening law multipler and exponent, respectively, and ε^p is the plastic strain.

Nonlinear fibre compressive behaviour

During compression of a ply in fibre-direction, the Young's modulus is not constant until failure. Due to fibre misalignments and local fibre microbuckling, the longitudinal Young's modulus decreases with increasing compression strain and this phenomenon is taken into account by defining the following expression for the compressive longitudinal modulus:

$$E_1(\varepsilon_{11}) = \frac{E^c_{1,0}}{1 + \Gamma E^c_{1,0}\left|\varepsilon_{11}\right|} \tag{4.13}$$

where Γ is a material constant related with the compressive Young's modulus loss and E_1^{0c} is the initial compressive Young's modulus in fibre-direction.

Strain rate dependency implementation

The implemented strain rate dependent model is based on the work of Rozycki [53] and it is an adaptation of the general rate dependency models widely used for metals, except that for composites the dependency is anisotropic.

The base of the rate dependent model is the splitting of the general stress tensor into an elastic part ($\boldsymbol{\sigma^e}$) and a viscous component ($\boldsymbol{\sigma^v}$):

$$\boldsymbol{\sigma} = \boldsymbol{\sigma^e} + \boldsymbol{\sigma^v} \tag{4.14}$$

and the in-plane constitutive relation becomes:

$$\begin{Bmatrix} \sigma_{11} \\ \sigma_{22} \\ \sigma_{12} \end{Bmatrix} = \begin{bmatrix} C_{11} & \nu_{21} C_{11} & 0 \\ \nu_{21} C_{11} & C_{22}(1-d_{22}) & 0 \\ 0 & 0 & C_{12}(1-d_{12}) \end{bmatrix} \begin{Bmatrix} \varepsilon_{11}^{e} \\ \varepsilon_{22}^{e} \\ \gamma_{12}^{e} \end{Bmatrix} \tag{4.15}$$

where C_{ij} are functions of the strain rate in the form:

$$C_{11} = C_{11}^{0}(1 + F_{11}(\dot{\varepsilon})) \tag{4.16a}$$

$$C_{22} = C_{22}^{0}(1 + F_{22}(\dot{\varepsilon})) \tag{4.16b}$$

$$C_{12} = C_{12}^{0}(1 + F_{12}(\dot{\varepsilon})) \tag{4.16c}$$

where the superscript 0 denotes the reference value, i.e. before any strain rate effect, and F_{ij} are three viscosity functions affecting the longitudinal, transverse and shear moduli.
The values of the initial and critical evolution of the shear damage function, respectively $Y_{ij,0}$ and $Y_{ij,crit}$ introduced in equation (4.10) are then affected by the viscosity functions F_{ij}:

$$\underline{Y_{12,0}} = Y_{12,0}\sqrt{1 + F_{12}(\dot{\varepsilon})} \tag{4.17a}$$

$$\underline{Y_{12,crit}} = Y_{12,crit}\sqrt{1 + F_{12}(\dot{\varepsilon})} \tag{4.17b}$$

$$\underline{Y_{22,0}} = Y_{22,0}\sqrt{1 + F_{22}(\dot{\varepsilon})} \tag{4.17c}$$

$$\underline{Y_{22,crit}} = Y_{22,crit}\sqrt{1 + F_{22}(\dot{\varepsilon})} \tag{4.17d}$$

The yield stress of equation (4.12) is also affected by a viscosity function $F_R(\dot{\varepsilon})$, which then also affects the yield function introduced in equation (4.11):

$$\underline{R_0} = R_0(1 + F_R(\dot{\varepsilon})) \tag{4.18a}$$

$$f(\boldsymbol{\sigma}, R) = \sqrt{\left[\frac{\sigma_{12}}{(1-d_{12})}\right]^2 + a^2\left[\frac{\langle\sigma_{22}\rangle_+}{(1-d_{22})} + \langle\sigma_{22}\rangle_-\right]^2} - \left(\underline{R_0} + \eta(\varepsilon^p)^n\right) \tag{4.18b}$$

The fifth and last viscosity function $F_{11}^{\varepsilon}(\dot{\varepsilon})$ affects the longitudinal compressive failure strain $\varepsilon_{1,fail}^{c}$ of the maximum strain criterion, which governs failure in fibre-direction:

$$\underline{\varepsilon_{1,fail}^{c}} = \varepsilon_{1,fail}^{c}\left(1 + F_{11}^{\varepsilon}(\dot{\varepsilon})\right) \tag{4.19}$$

In summary, five viscosity functions (also called functions of evolution) can be implemented in the material card of the unidirectional ply:

- $F_{11}(\dot{\varepsilon})$ which affects the longitudinal Young's modulus E_1;
- $F_{22}(\dot{\varepsilon})$ which affects the transverse Young's modulus E_2;
- $F_{12}(\dot{\varepsilon})$ which affects the shear modulus G_{12};

- $F_R(\dot{\varepsilon})$ which affects the laminate transverse yield stress R_0 and
- $F_{11}^{\varepsilon}(\dot{\varepsilon})$ which affects the longitudinal compressive failure strain $\varepsilon_{1,fail}^{c}$.

Each of these five functions of evolution can be implemented either as a linear, power or logarithmic laws, depending on which type fits better with the experimentally obtained data:

$$\text{Linear Law:} \quad F_{ij}(\dot{\varepsilon}) = D_{ij}\left(\frac{\dot{\varepsilon}}{\dot{\varepsilon}^{ref}}\right) + n_{ij} \tag{4.20a}$$

$$\text{Power Law:} \quad F_{ij}(\dot{\varepsilon}) = D_{ij}\left(\frac{\dot{\varepsilon}}{\dot{\varepsilon}^{ref}}\right)^{n_{ij}} \tag{4.20b}$$

$$\text{Logarithmic Law:} \quad F_{ij}(\dot{\varepsilon}) = D_{ij}\ln\left(\frac{\dot{\varepsilon}}{\dot{\varepsilon}^{ref}}\right) + \ln(n_{ij}) \tag{4.20c}$$

where $\dot{\varepsilon}^{ref}$ is the threshold above which the strain rate influences the respective mechanical property and the function of evolution is used, and D_{ij} and n_{ij} are the parameters to fit the laws with the experimental data.

Strain rate dependency of moduli

From the experiments performed and presented previously in section 3.4 using specimens with $[0°]_{16}$, $[90°]_{16}$ and $[+45°/-45°]_{4s}$ layups it is possible to verify how the longitudinal, transverse and shear moduli change with increasing strain rate. Figure 4.1 presents this information on a logarithmic scale x-axis.

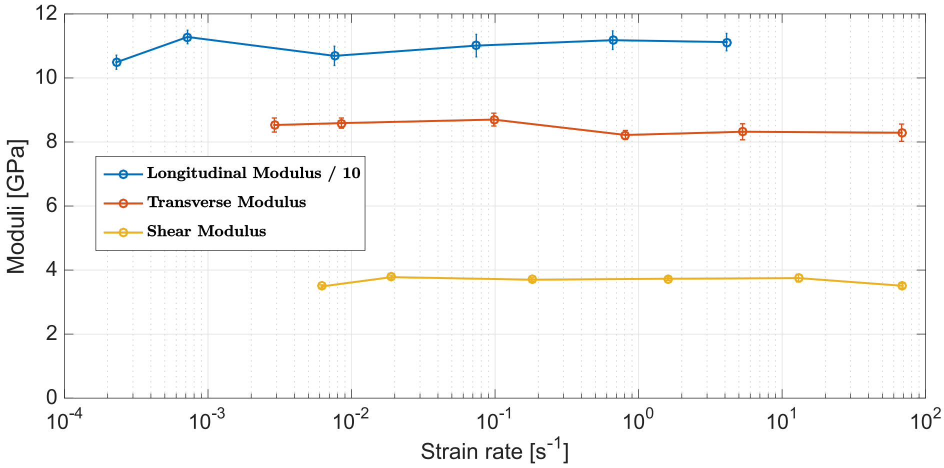

Figure 4.1: Longitudinal, transverse and shear moduli over the strain rate range tested.

As shown in Figure 4.1, none of the three moduli for the elementary ply change significantly with increasing strain rate. Therefore, no function of evolution can be fitted to any of them.

Strain rate dependency of longitudinal fracture strain

As shown in section 3.4.2, the longitudinal compressive strain at failure of unidirectional plies increases with increasing strain rate. Over the strain rate range achieved, the fracture strain increased by approximately 26%.

Figure 4.2 shows the experimentally obtained data for the fracture strain, together with the best fit power and logarithmic laws. It was decided to not include the linear fitting law because, given the experimental data, a linear law is not suitable.

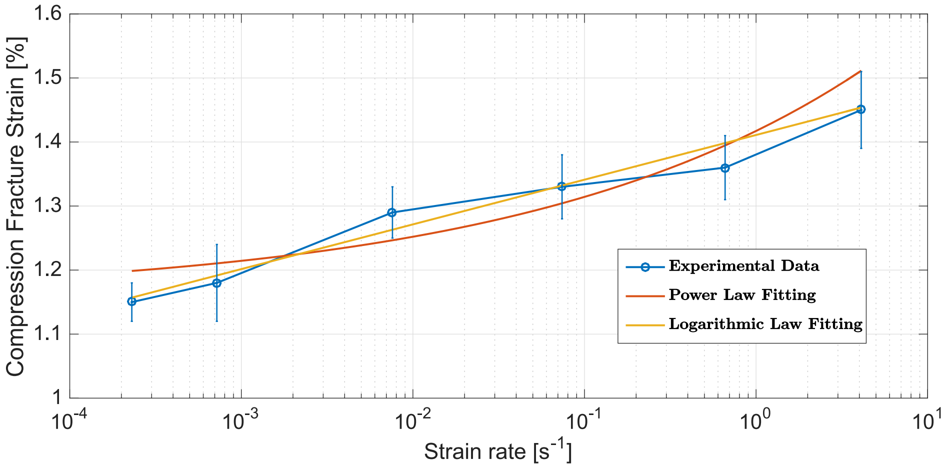

Figure 4.2: Experimentally obtained longitudinal compressive failure strain at different strain rates, together with fitting laws.

Between the power and logarithmic fitting laws, the logarithmic one is a significant better fit for the experimental data. The squared error of the logarithmic law is about one fourth of the squared error obtained for the best fitting power law. Furthermore, the power fitting law leads to a discontinuity at the the strain rate threshold, which in this case is the quasi-static speed.

Therefore, the longitudinal compressive fracture strain is implemented in the FE software using the logarithmic fitting law in the range of strain ranges tested as:

$$\underline{\varepsilon^{c}_{1,fail}} = \varepsilon^{c}_{1,fail}\left[1 + D_{ij}\ln\left(\frac{\dot{\varepsilon}}{\dot{\varepsilon}^{ref}}\right) + \ln(n_{ij})\right] \tag{4.21}$$

which, replacing the values of D_{ij} and n_{ij}, and taking into account that the logarithmic law should not be extrapolated beyond the maximum strain rate achieved:

$$
\underline{\varepsilon^{c}_{1,fail}} = \begin{cases} 1.15\ [\%] & \text{if} \quad \dot{\varepsilon} < 2.3 \times 10^{-4}\ s^{-1} \\ 1.15 \times \left[1 + 0.0262 \ln\left(\dfrac{\dot{\varepsilon}}{2.3 \times 10^{-4}}\right) + \ln(1)\right] [\%] & \text{if} \quad 2.3 \times 10^{-4} \leqslant \dot{\varepsilon} \leqslant 4.1\ s^{-1} \\ 1.45\ [\%] & \text{if} \quad \dot{\varepsilon} > 4.1\ s^{-1} \end{cases} \tag{4.22}
$$

Strain rate dependency of yield stress

From the experimental tests performed with $[90°]_{16}$ layup specimens, the evolution of the yield stress over the strain rate was obtained (see section 3.4.3) and is presented in Figure 4.3, together with the best fitting power and logarithmic laws.

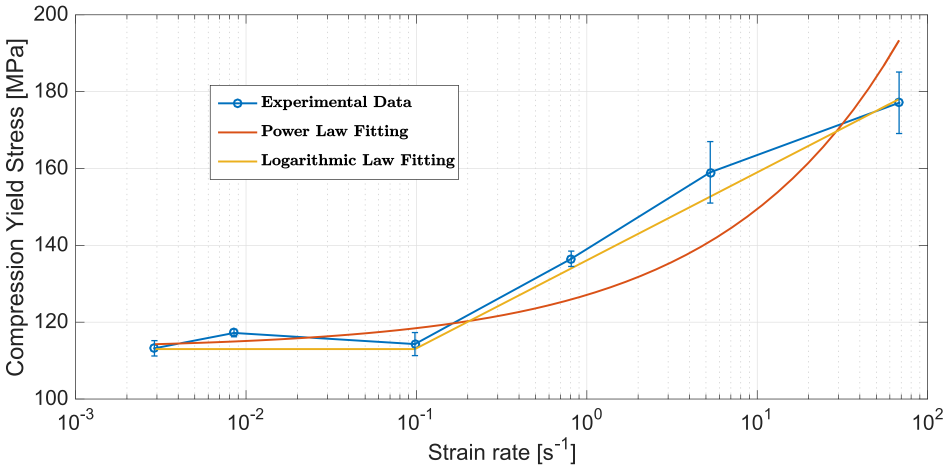

Figure 4.3: Experimentally obtained yield stress at different strain rates, together with fitting laws.

Between the two presented laws, the logarithmic is clearly a better fit for the experimental data. It is important to note that the threshold strain rate in this case is not the quasi-static one. Only above a strain rate of $10^{-1}\ s^{-1}$ does the yield stress significantly change. Therefore, the yield stress can be expressed for the entire strain rate range as:

$$
\underline{R_0} = \begin{cases} 113\ [\text{MPa}] & \text{if} \quad \dot{\varepsilon} < 10^{-1}\ s^{-1} \\ 113 \times \left[1 + 0.088 \ln\left(\dfrac{\dot{\varepsilon}}{10^{-1}}\right)\right] [\text{MPa}] & \text{if} \quad 10^{-1} \leqslant \dot{\varepsilon} \leqslant 68\ s^{-1} \\ 180\ [\text{MPa}] & \text{if} \quad \dot{\varepsilon} > 68\ s^{-1} \end{cases} \tag{4.23}
$$

4.2 Model Calibration and Validation

After the implementation of the strain rate laws in the ply material card, it is important to confirm that the material's behaviour is as close to the experimentally observed as possible. This is commonly performed using a one-element model, whose boundary conditions and load case are similar to the experimental tests from which the material properties were acquired [39,54]. The goal is to compare the experimental and simulation stress-strain curves, and if necessary, modify the ply material card until their agreement is satisfactory.

The model used in this work consists of a single squared shell element with a 10 *mm* side length. Similarly to the laminate used for the experiments on rectangular specimens, it is composed of 16 plies, each with a thickness of 0.15 *mm*, resulting in a total shell thickness of 2.4 *mm*.

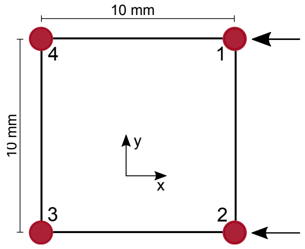

Node #	x-direction BC	y-direction BC	z-direction BC
1	free	free	fixed
2	free	fixed	fixed
3	fixed	fixed	fixed
4	fixed	free	fixed

Figure 4.4 & Table 4.1: One shell element model with the respective nodal displacement boundary conditions.

Figure 4.4 contains a drawing of the used one-element model with indication of the nodal displacement boundary conditions.

Nodes numbered 1 and 2 are allowed to move in x-direction, which corresponds to compression/extension of the element. To allow for Poisson's effects, nodes numbered 1 and 4 are free to move in the y-direction. Node numbered 3 is fixed in both x and y directions. The compression force is applied in the element by a prescribed velocity on nodes 1 and 2. Depending on the magnitude of the applied nodal velocity v, the strain rate is constant and determined by:

$$\dot{\varepsilon}_{\text{1-element model}} = \frac{v\ [\text{m/s}]}{\text{side length [m]}} = \frac{v}{0.01}[s^{-1}] \tag{4.24}$$

A comparison between the experimentally and numerically obtained stress-strain curves can be performed for the different laminates tested and previously presented in section 3.4.1.

4.2.1 Longitudinal Ply Properties Validation

By setting the shell element's layup to 16 plies of 0° orientation, i.e. along the x-direction, and adjusting the nodal velocity v in accordance with (4.24) to meet the strain rate achieved experimentally, the numerical stress-strain curves in the longitudinal direction can be directly compared with the experimental ones presented in section 3.4.2. Figure 4.5 shows the simulation longitudinal stress-strain curves obtained at different strain rates with the one-element

Table 4.2: Comparison of longitudinal compressive strength and failure strain between experimental and simulation results.

Strain Rate	Compression Strength			Compression Failure Strain		
$\dot{\varepsilon}$ $[s^{-1}]$	Exp. [MPa]	Sim. [MPa]	Error [%]	Exp. [%]	Sim.[%]	Error [%]
2.3×10^{-4}	1165	1168	+0.3	1.15	1.16	+0.9
7.2×10^{-4}	1215	1198	-1.4	1.18	1.19	+0.8
7.6×10^{-3}	1288	1258	-2.4	1.29	1.26	-2.4
7.4×10^{-2}	1352	1316	-2.7	1.33	1.33	0
6.6×10^{-1}	1380	1371	-0.7	1.36	1.39	+2.2
4.1	1422	1415	-0.5	1.45	1.44	-0.7

model and Table 4.2 summarizes the compression strength and failure strain, obtained both experimentally and numerically.

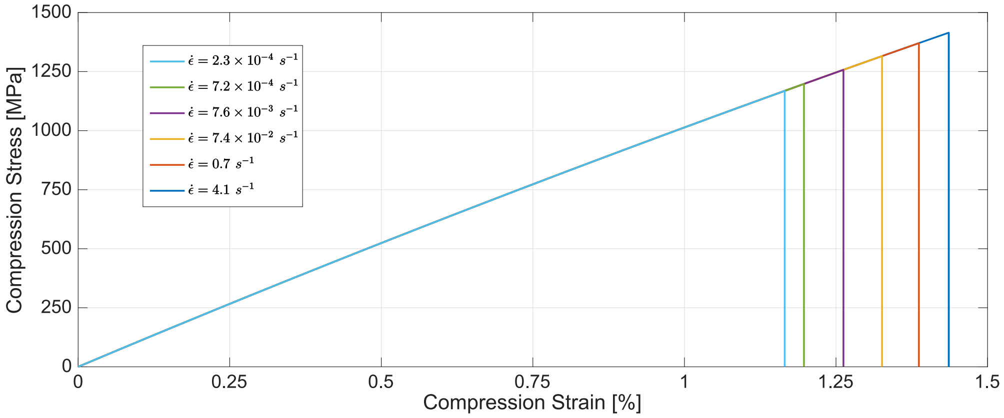

Figure 4.5: Longitudinal stress-strain curves obtained with the one-element calibration model.

As Figure 4.5 shows, the simulation longitudinal stress-strain response is in agreement with the results found experimentally and presented in section 3.4.2. With increasing loading rate, the longitudinal Young's modulus does not change. The increase in compression strength for faster impact speeds is solely due to an increase in fracture strain.

The comparison presented in Table 4.2 indicates a very good agreement between experimental and numerical data. The strain rate dependent longitudinal properties of the laminate are accurately predicted and simulated by the implemented model, as the relative error of compression strength and failure strain is, on average, 1.3% for the six strain rate levels tested.

4.2.2 Transverse Ply Properties Validation

The implemented model's behaviour can also be analysed in the transverse direction by running simulations with a $[90°]_{16}$ layup shell element, i.e. with the fibres aligned along the y-direction. Figure 4.6 presents the simulation transverse stress-strain curves at loading rates similar to the ones experimentally obtained.

As expected, the transverse Young's modulus is constant throughout the strain rate range simulated, which is a similar result to the one obtained in the experiments of rectangular specimens and presented previously in section 3.4.3.
Even though it shows a high variation, the transverse failure strain was found experimentally to not be strain rate dependent, and it averages at 5.2% for the six loading rates tested. Therefore, in the maximum strain failure criterion of the implemented model, a maximum transverse strain of 5.2% was defined, which is the reason why the simulation stress-strain curves of Figure 4.6 all fail at this strain level.
In general, the implemented model replicates accurately the experimentally observed trend in increasing yield stress, and corresponding yield strain, for higher strain rates. Table 4.3 presents a more explicit comparison between experiments and simulations of the laminate's transverse direction properties.

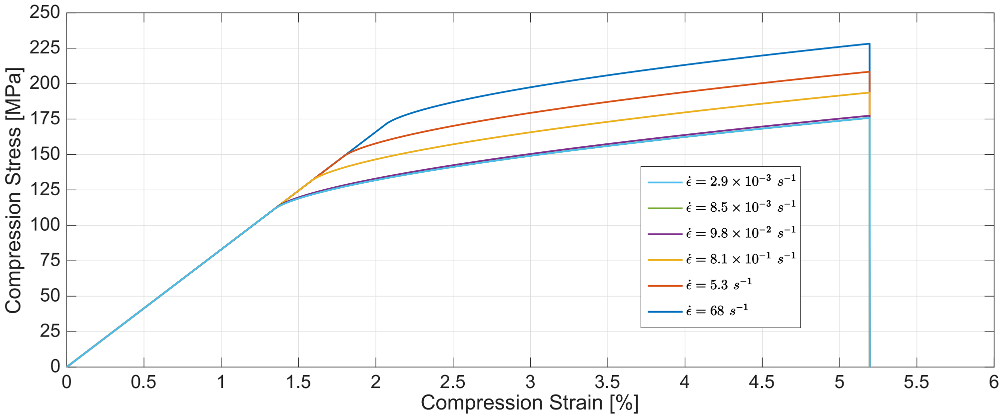

Figure 4.6: Transverse stress-strain curves obtained with the one-element calibration model.

As Table 4.3 shows, the numerical model accurately reproduces the transverse yield stress, as the relative error between experiments and simulations is kept below 4%.
However, there is a quite significant discrepancy in transverse compression strength between experiments and simulations. The reason for this difference has to do with the hardening law after yielding. As shown in the experimental stress-strain curves of Figure 3.14, the hardening law seems to vary with increasing rate, causing the laminate's transverse response to be less ductile after yielding. Yet, this variation in hardening law with varying loading rate cannot be implement in the simulation model, as it only allows for the incorporation of a single hardening law, which is used across the entire strain rate range. To limit the relative error between experiments and simulation, the implemented hardening law fits the real material response at the middle of the strain rate range. For this reason, the simulation model overpredicts the transverse compression strength at low strain rates (up to +9.7% relative error) and underpredicts at higher strain rates (up to −7.8% relative error).
The differences between experimental and simulation stress-strain curves can be better examined in Appendix B, where these are plotted together.

Nevertheless, this small error in transverse compression strength between experiments and simulation occurs at relatively large strains - higher than 3%. For most applications, it is not common to reach such high deformation levels, as usually there are plies containing fibres

Table 4.3: Comparison of transverse compressive yield and ultimate stress between experimental and simulation results.

Strain Rate	Yield Stress			Compression Strength		
$\dot{\varepsilon}$ $[s^{-1}]$	Exp. [MPa]	Sim. [MPa]	Error [%]	Exp. [MPa]	Sim.[MPa]	Error [%]
2.9×10^{-3}	113	113	0	158	175	+9.7
8.5×10^{-3}	117	113	-3.5	165	175	+5.7
9.8×10^{-2}	114	114	0	175	177	+1.1
8.1×10^{-1}	136	134	-1.5	194	194	0
5.3	159	153	-3.9	216	209	-3.3
68	177	175	-1.1	247	229	-7.8

aligned with the loading direction and these fail at much lower strains. For this reason, it was decided that the found discrepancy in transverse compression strength at high strains can be disregarded, as the likelihood of reaching such strains is minuscule.

4.2.3 Shear Ply Properties Validation

The implementation of the material shear properties can be analysed by running simulations with a layup similar to the one used in the experiments - $[+45°/-45°]_{4s}$.
Figure 4.7 shows the simulation shear stress-strain curves resulting from running the one-element model with strain rates similar to the experimental ones. Once again, the initial modulus does not vary with increasing strain rate, which is a result consistent with the experimental data.
There is, however, a quite significant difference between the simulation shear response (Figure 4.7) and the experimental shear response (Figure 3.15). The simulation curves are characterized by an almost-linear response up until the matrix yields and a clear drop in stiffness is visible. On the other hand, the experimental curves of Figure 3.15 do not have a clear sudden drop in stiffness, but a more smooth stiffness reduction across a larger strain range. This difference can be explained by the effect of fibre scissoring that is present during the experimental tests, which causes the fibres to lose its ±45° orientation and constantly reduce the shear stiffness. On the simulation model, however, this effect is not implemented and a reduction in stiffness happens only when the matrix yield stress is reached.

A comparison between experimental and simulation shear stress-strain curves is summarized in Table 4.4 by digitising the shear stress at two shear strain levels: 2.5% and 5%, for the six strain rates tested.
At a shear strain of 2.5%, the simulation overpredicts the experimental shear stress by an average of 4.1% mainly due to the reason mentioned previously related with the slightly dissimilar shape of the experimental and simulation shear stress strain curves. At a shear strain level of 5%, the correlation between simulation and experimental shear stress is somewhat better, with the simulation underpredicting the experimental stress by 1.7%, on average.
Even with the small issue presented previously regarding the slightly different shear behaviour between experimental and simulation, the relative error between the curves is kept below 10%, which means that a rather good agreement is reached.

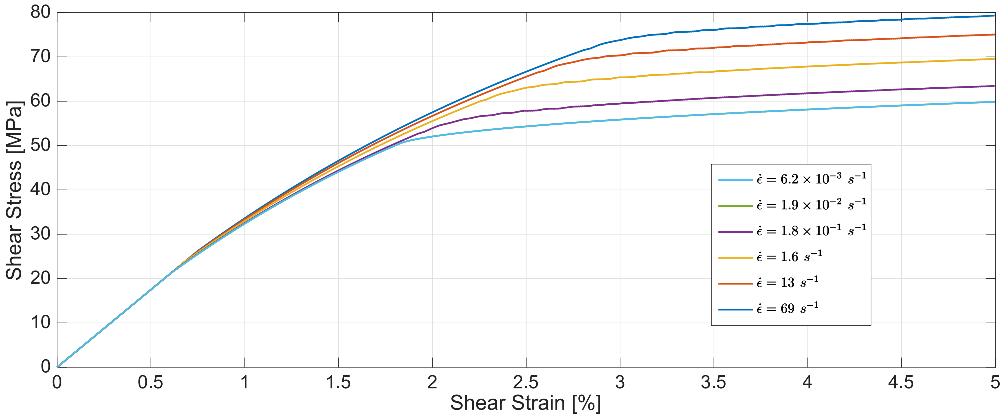

Figure 4.7: Shear stress-strain curves obtained with the one-element calibration model.

Table 4.4: Comparison of shear stress between experimental and simulation results at two shear strain levels.

Strain Rate	Stress at 2.5% shear strain			Stress at 5% shear strain		
$\dot{\varepsilon}$ $[s^{-1}]$	Exp. [MPa]	Sim. [MPa]	Error [%]	Exp. [MPa]	Sim.[MPa]	Error [%]
6.2×10^{-3}	51.7	54.3	+4.8	60.0	59.9	-0.2
1.9×10^{-2}	53.3	54.3	+1.8	63.1	59.9	-5.3
1.8×10^{-1}	55.6	57.9	+3.9	67.2	64.5	-4.2
1.6	59.7	63.0	+5.2	70.9	69.6	-1.9
13	61.5	65.5	+6.1	76.8	75.1	-2.3
69	64.7	66.7	+3.0	76.3	79.3	+3.8

4.2.4 Multidirectional Laminates Validation

Given the rather good agreement between experimental and simulation for the longitudinal, transverse and shear properties presented in the three previous subsections, a comparison can also be performed for the multidirectional laminates.
Setting focus on the applicability of the present work, it is important to understand the behaviour of the implemented model when simulations are performed with layups that are more commonly used in the automotive and aerospace industry. These simulations can then be compared with the experimental tests performed with rectangular specimens and presented in sections 3.4.5 and 3.4.6, and conclusions regarding the correlation can be drawn. Specimens with a $[0°/90°]_{4s}$ and $[+45°/-45°/0°/90°]_{2s}$ layups were experimentally tested, and the simulation results are presented in the following subsections for each layup.

4.2.4.1 $[0°/90°]_{4s}$ layup simulation results

As presented in section 3.4.5 and further analysed in section 3.4.7, the failure strain of 0° plies when embedded in multidirectional laminates is significantly larger than when testing a laminate containing only 0° plies. The simulation model implemented in Pam-Crash® presented in section 4.1 is based on the properties of a single ply, especially the longitudinal fracture

strain implemented for the maximum failure strain criterion, which was determined from experiments on specimens containing only 0° plies. Using the same maximum strain failure criterion in fibre-direction when running simulations on laminates with multiple orietantions would lead to considerable underpredictions, as the laminate would fail at the strain that it does when not embedded in layups with other orientations.
For this reason, a slight adjustment has to be performed in the simulation material card when running simulations with multidirectional laminates. For the current case of a $[0°/90°]_{4s}$ layup, the longitudinal fracture strain at quasi-static strain rates has to be modified from 1.15% (value obtained when testing $[0°]_{16}$ specimens) to 1.37%, which is the value obtained experimentally when testing $[0°/90°]_{4s}$ layup specimens at QS speeds.

Figure 4.8 contains the compression stress-strain curves obtained numerically with the one-element shell model for a $[0°/90°]_{4s}$ layup, at strain rates analogous to the experimentally achieved. Similarly to the experimental results, the stiffness of the laminate does not vary with increasing strain rate, since the response is dominated by the 0° plies and the longitudinal Young's modulus is constant throughout the strain rate range tested. There is, however, a clear trend in increasing failure strain with increasing strain rate, which leads to an identical increase in compression strength.

Table 4.5 summarizes the compression strength and failure strain obtained both experimentally and through simulations with the one-element model for the six strain rates tested. For the compression strength, the simulation slightly overpredicts the experimental results, resulting on an average relative error of approximately 2%. On the other hand, the failure strain is underpredicted by 4% on average.
These small discrepancies between simulation and experimental results are quite insignificant and they fall under the variation observed experimentally. Therefore, it can be concluded that the implemented simulation model is able to capture the strain rate dependent behaviour of the $[0°/90°]_{4s}$ layup specimens quite well.

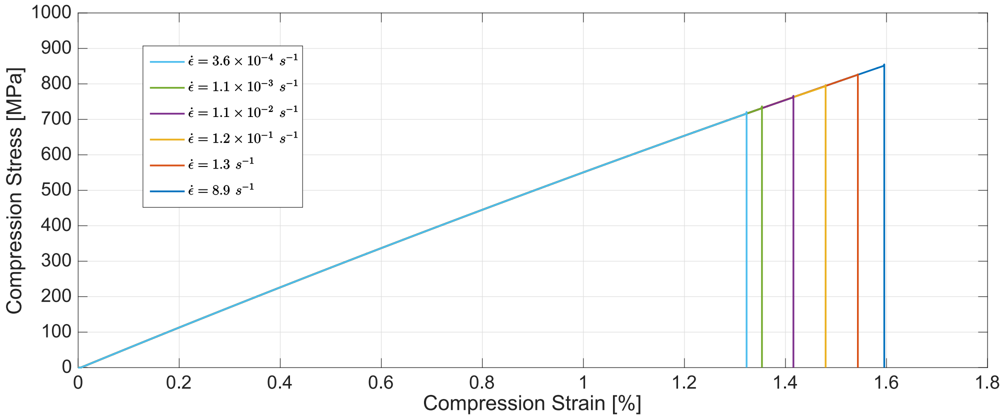

Figure 4.8: Stress-strain curves of the calibration model using a $[0°/90°]_{4s}$ layup.

Table 4.5: Comparison of compressive strength and failure strain between experimental and simulation results for the $[0°/90°]_{4s}$ layup.

Strain Rate	Compression Strength			Compression Failure Strain		
$\dot{\varepsilon}$ $[s^{-1}]$	Exp. [MPa]	Sim. [MPa]	Error [%]	Exp. [%]	Sim.[%]	Error [%]
3.6×10^{-4}	704	714	+1.4	1.37	1.33	-3.0
1.1×10^{-3}	745	732	-1.8	1.45	1.37	-5.8
1.1×10^{-2}	754	760	+0.8	1.50	1.42	-5.6
1.2×10^{-1}	763	791	+3.5	1.57	1.49	-5.3
1.3	793	821	+3.4	1.59	1.55	-2.5
8.9	811	848	+4.3	1.63	1.60	-1.8

4.2.4.2 $[+45°/-45°/0°/90°]_{2s}$ layup simulation results

A similar analysis can also be carried out for the other multidirectional laminate tested: $[+45°/-45°/0°/90°]_{2s}$.
In the current case, the maximum strain failure criterion in the longitudinal (in-fibre) direction has to be modified for the same reason as mentioned in the previous subsection. Instead of the 1.15% longitudinal strain, the maximum strain criterion is set to 1.71% for QS speeds, as this was the value achieved experimentally. Nonetheless, the evolution law presented in Figure 4.2 is unchanged, thus the increase in longitudinal fracture strain with increasing strain rate is identical to the previously implemented in section 4.1.

Figure 4.9 presents the compression stress-strain curves obtained by running the one-element shell model at strain rates comparable with the experimental ones, using the current quasi-isotropic layup. For high strains (above 1.6%), the laminate stiffness reduces slightly, which is expected and can be explained by the occurrence of yielding in the plies oriented transversely. Furthermore, the trend of increasing failure strain with increasing strain rate is in agreement with the experimentally obtained results presented in subsection 3.4.6.

A summarized comparison of the experimentally and numerically obtained results for this layup is presented in Table 4.6. Similarly to the results presented in the previous subsection, the simulation model overpredicts the compression strength, in this case by an average relative error of 4.5%. In contrast, the compression failure strain is underpredicted by 2.1%.

Overall, the simulations ran on multidirectional laminates are in very good agreement with the experimental data. The main reason for this good correlation is the fact that the mechanical response of both these multidirectional laminates is dominated by the 0° plies. Since the implementation of the ply in the longitudinal direction presented in subsection 4.2.1 was in excellent compliance with the experimental data, it is carried over to both multidirectional layups.
Furthermore, failure is also sudden and abrupt, without a significant drop in laminate stiffness, which is an indication that the 0° plies also govern failure for the multidirectional laminates. Therefore, the same law of evolution for the fracture strain can be used for the different laminates and the dynamic failure strains are quite accurate.

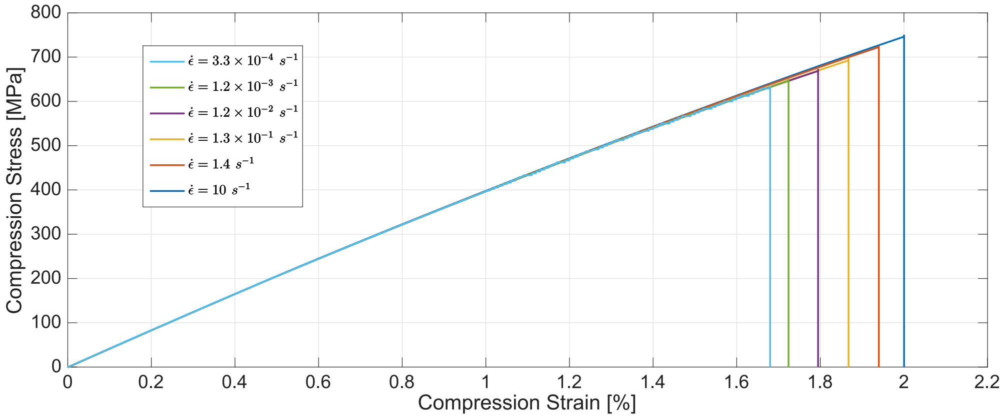

Figure 4.9: Stress-strain curves of the calibration model using a $[+45°/-45°/0°/90°]_{2s}$ layup.

Table 4.6: Comparison of compressive strength and failure strain between experimental and simulation results for the $[+45°/-45°/0°/90°]_{2s}$ layup.

Strain Rate	Compression Strength			Compression Failure Strain		
$\dot{\varepsilon}$ $[s^{-1}]$	Exp. [MPa]	Sim. [MPa]	Error [%]	Exp. [%]	Sim.[%]	Error [%]
3.3×10^{-4}	610	629	+3.0	1.71	1.68	-1.8
1.2×10^{-3}	606	645	+6.0	1.78	1.73	-2.8
1.2×10^{-2}	629	665	+5.4	1.83	1.79	-2.2
1.3×10^{-1}	640	685	+6.5	1.88	1.87	-0.5
1.4	690	721	+4.3	2.02	1.94	-4.1
10	730	745	+2.0	2.03	2.00	-1.5

4.3 Crash Simulations on Omega-profile Specimens

An important aspect of the implementation of the laminate strain rate dependent properties in a simulation code is to verify if the behaviour of structural components with somewhat complex shapes under impact loads is similar between experiments and simulation. This will provide authentication that entire car structures with components made of carbon-epoxy laminates can be simulated using the developed simulation model and the obtained results are realistic and in agreement with the experimental behaviour.

Therefore, a simulation model was developed that depicts the crash tests performed with the omega-profile cross-section component presented previously in section 3.5. The model is composed of 4224 shell elements, each with a side length of approximately 1.5 mm, using the same layup as experimentally tested: $[+45°/-45°/+45°/-45°/0°/90°]_s$. A mesh convergence study was performed in order to determine the necessary number of elements/nodes and is presented in Appendix C. The load is applied through a velocity boundary condition on all the nodes on the top 20 mm of the specimen, simulating the top clamp of the fixture, which translates downwards after the impact and compresses the specimen. The magnitude of the applied velocity is chosen such that a similar strain rate is achieved between simulations and experimental tests. Figure 4.10 shows the model with the nodes where the velocity boundary conditions is applied being highlighted.

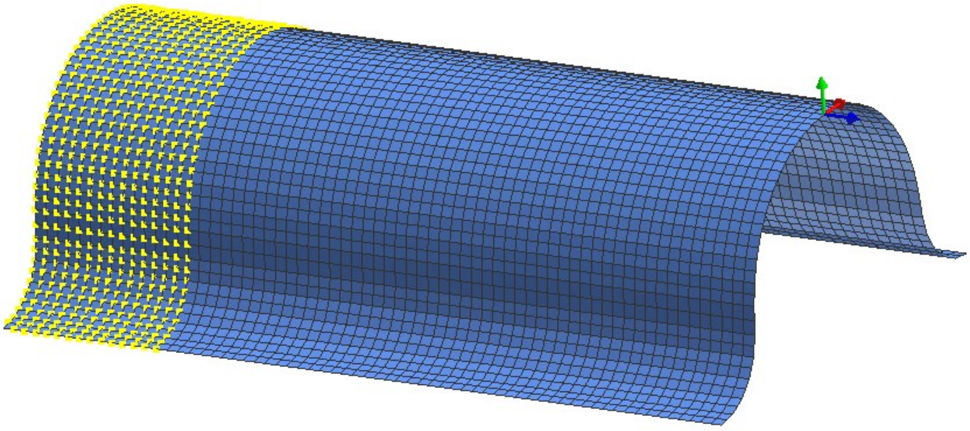

Figure 4.10: Simulation model of the omega-profile structural component with the nodes subjected to a velocity boundary condition highlighted.

Table 4.7: Comparison of maximum load and failure strain between experimental and simulation results for the omega-profile cross-section component.

Strain Rate $\dot{\varepsilon}$ $[s^{-1}]$	Maximum Load Exp. [kN]	Sim. [kN]	Error [%]	Strain at failure Exp. [%]	Sim.[%]	Error [%]
1.9×10^{-4}	55.6	57.3	+2.9	1.21	1.10	-10
5.3×10^{-2}	60.3	63.3	+4.7	1.34	1.23	-8.9
4.7	67.3	69.2	+2.7	1.42	1.35	-5.2

Figure 4.11 contains the force-displacement graphs resulting from running the crash simulation analysis for each of the three strain rates achieved experimentally. Also in Figure 4.11 the experimentally obtained force-displacement curves of each testing velocity are presented for a better comparison with the simulation curves.

The simulation force-displacement curves are linear until failure, where the cross-section force immediately drops to zero. The fact that there is no drop in the component stiffness signifies that there is no manifestation of buckling, crippling or any other failure phenomenon related with the specimen geometry. The sudden drop in cross-sectional force indicates that failure occurs due to material failure, which in the simulation is seen as elements being eliminated because their longitudinal maximum allowed strain is reached. This kind of failure is in total agreement with the experimental results, where failure is also abrupt. Furthermore, the simulation model fails in the elements close to the center of the specimen, just like the experimental results presented in Figure 3.22.

Regarding the maximum load and the failure strain, Table 4.7 contains a comparison between the experimentally and numerically obtained results. The simulation model overpredicts the maximum load on the specimen by an average relative error of 3.4%. On the other hand, the failure strain is underpredicted by 8%.

It is important to note that, as mentioned previously on section 3.5, the manufactured omega-profile cross-section specimens had a quite significant amount of defects due to adversities emerged during hand-layup of the plies. This resulted in a significant variation of the experi-

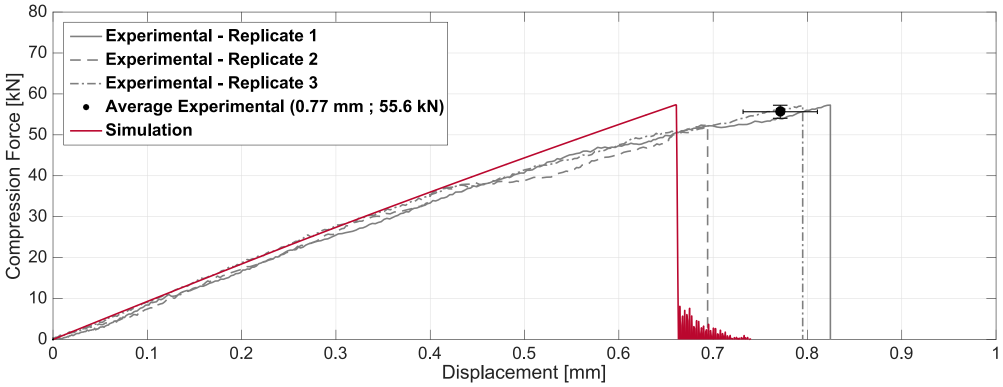

(a) $\dot{\varepsilon} \approx 1.9 \times 10^{-4}\ s^{-1}$

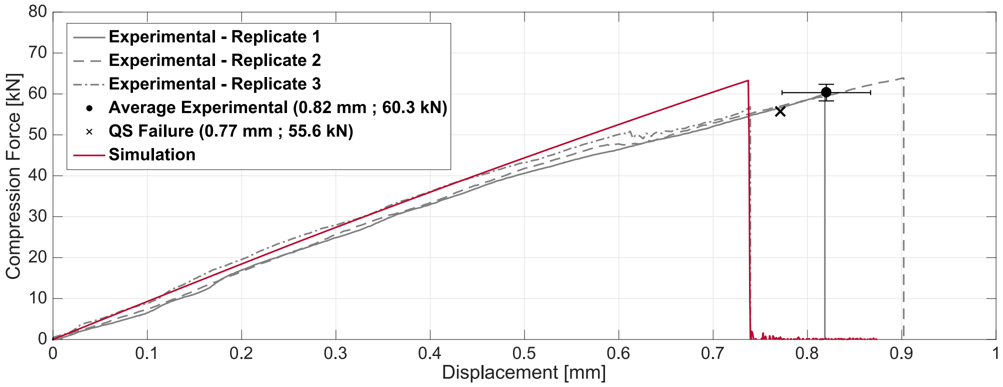

(b) $\dot{\varepsilon} \approx 5.3 \times 10^{-2}\ s^{-1}$

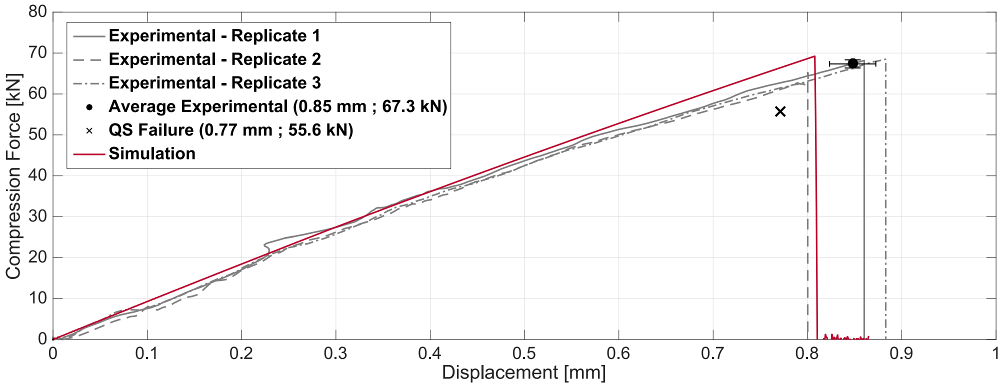

(c) $\dot{\varepsilon} \approx 4.7\ s^{-1}$

Figure 4.11: Force-displacement plots resulting from the simulation analysis at three different strain rates, together with the experimentally obtained curves.

mentally achieved failure strains, which translates into a not-so-accurate mean value presented in Table 4.7. Furthermore, as the experimental failure strains were lower than expected, the maximum failure criterion of the simulation model had to be readjusted back to the longitudinal failure strain observed in $[0°]_{16}$ layup specimens, instead of the higher values observed in $[+45°/-45°/0°/90°]_{2s}$ layup specimens, which is similar to the layup of the omega-profile components.

Nonetheless, the most important output of the comparison between experimental and simulation results is the very good agreement in terms of maximum cross-section load. The simulation model is able to not only accurately predict the maximum load, but also the growth in mechanical properties with increasing strain rate.

It can be concluded from the current analysis that the implemented finite element model is able to correctly simulate the mechanical compressive behaviour of carbon-epoxy laminates with a non-elementary shape/cross-section, subjected to different impact velocities. The agreement between experimental and simulation maximum load and type of failure is extremely reliable. However, there is a slight inconsistency on the failure strain between experiments and simulations, which most likely results from manufacturing defects.

4.4 Summary and Conclusions

In this section, a summary of the current chapter is presented and conclusions regarding the implementation of the strain rate dependent mechanical properties on a finite element software are drawn. Firstly, the used numerical model was explained in detail together with the inclusion of the varying properties of the carbon-epoxy laminate previously found and show in chapter 3. Then, a single shell element model was used to calibrate and validate the laminate's strain rate dependent properties. Finally, the results of performing simulations on a structural component are displayed and compared with the experimental data of chapter 3.

The used finite element model makes use of Mindlin plate theory to describe shell elements, together with the ply mechanics developed by Ladeveze and Le Dantec [52] based on a continuum damage mechanics approach. The model's transverse and shear damage propagation processes were explained and the influence of the strain rate on the laminate's longitudinal, transverse and shear mechanical properties were described in detail. Furthermore, functions of evolution were fitted to the experimental data and implemented in the simulation material card using a logarithmic law - the mechanical properties increase linearly with the logarithm of the strain rate.

To calibrate and validate the implementation of the laminate's properties in the simulation material card, especially the strain rate dependent ones, a single shell element model was used. Simulations were performed using this one-element model with layups and strain rates similar to ones tested experimentally in chapter 3. A very good agreement between experimental and simulation results was found for the longitudinal (in-fibre direction) properties of the laminate. Similarly, the yield stress in transverse direction was also described quite accurately by the implemented model. However, the simulation transverse and shear stress stress-strain curves do not have the exact same shape as the experimentally obtained ones, mainly due to changes in the matrix hardening law with increasing strain rate, which was not implemented in the simulation material card.

To finalize, simulations using the previously implemented ply properties were performed on a structural component also previously compressed and presented in chapter 3 - an omega-profile cross-section part. The simulation output was in good agreement with the experimental results for the three strain rates tested, especially the maximum cross-section force. The strain at failure obtained numerically is slightly different from the experimental data, and this was attributed to the manufacturing defects during lay-up of the plies.

The main conclusion of the present chapter is that strain rate dependent properties of carbon-epoxy laminates can be determined experimentally through dynamic tests on simple rectangular specimens, implemented on the finite element material card and used to perform simulations on structural components with more complex shapes or cross-sections. The presented simulations on the omega-profile structural component showed a rather good agreement with the experimental results and confirmed that there is no attenuation or increase in the strain rate dependent properties determined from simple rectangular specimens.
There is, however, room for improvement in the simulation material card. Even though the yield stress varies with increasing strain rate and this was implemented in the material card, the matrix hardening law also changes (the matrix becomes less ductile) with strain rate and this effect was not included in the simulation analysis performed.

Chapter 5

Summary, Conclusions and Recommendations

To obtain the strain rate dependent compression properties of T700-DT120 carbon-epoxy material system, the work presented in the current thesis contains the experimental results of impact tests performed on rectangular specimens with five different layups, subjected to six distinct loading rates. The obtained strain rate dependent behaviour of the laminate was then accurately implemented in a commercially available finite element package. Finally, crash experiments at three different speeds were performed on a widely used structural component and compared with the results predicted by the previously implemented strain rate dependent simulation code, resulting in a good agreement between experiments and numerical simulations.
The current chapter contains a summary and the conclusions reached in each chapter of the present work, together with the answers to the research questions considered in section 2.6.

From the comprehensive literature review presented in chapter 2, it is apparent that the strain rate dependency of the reinforcement material highly depends on the type of fibre used. For carbon fibres, it was found that their mechanical response is identical under low or high loading rates. For the resin matrix, however, the mechanical behaviour greatly depends on the strain rate applied. Either under tension, compression or shear load cases, epoxy systems show an increase in mechanical properties with increasing strain rate, especially the yield and fracture stress, as the resin gets less ductile.
The strain rate dependency observed in epoxy systems is carried over to carbon-epoxy laminates when testing in matrix-dominated directions, such as transverse tension/compression and shear. In longitudinal direction (fibre-dominated), even though carbon fibres are not strain rate dependent, CFRP show an increase in fracture strain, accompanied by an identical increase in strength. This behaviour is directly related with the improvement in matrix properties at higher strain rates, causing the matrix to be able to support the fibres longer, delaying the occurrence of fibre microbuckling and consequent creation of kink bands, which is the main failure type under longitudinal compression and the reason for the lower compression properties of laminates, when compared to tension mechanical properties.

Chapter 3 contains the results obtained from the experimental impact tests at different speeds performed both on rectangular material coupons and on a structural component. It begins with a brief explanation of the experimental methods and equipment used, with a special attention on DIC and the proper alignment of the testing fixture.
An investigation was performed to find out the optimal geometry of the rectangular specimens, by carrying out a series of quasi-static tests on specimens with a unidirectional layup and different geometries. The ideal geometry was derived by analysing the influence of each geometrical factor on the basis of maximizing the achieved compression strength.
The derived optimal rectangular specimen geometry was adopted for the dynamic impact tests performed on specimens with five different layups. Each of these layups was subjected to six different impactor velocities, and the mechanical response was recorded using high-speed cameras, in combination with a piezoelectric load cell. The obtained dynamic mechanical response is in agreement with the previous studies shown in the literature review:

- In longitudinal direction, the compression fracture strain and strength increase by 26% and 22%, respectively, over the strain rate range tested. The longitudinal Young's modulus is not affected by the loading rate;
- In transverse direction, the compressive yield and fracture stress increase both by 56% over their respective QS values, when tested at a strain rate of approximately 70 s^{-1}. The transverse Young's modulus suffers no significant change;
- The shear yield stress and strength (truncated at 5% shear strain) increase by 37% and 27% over their QS values, respectively, at a strain rate of approximately 70 s^{-1}. The shear modulus is also not affected by the loading rate.

Following the analysis presented in section 3.4.4.1, it can be concluded that the increase in longitudinal compressive strength with increasing strain rate (due to an increase in matrix properties delaying fibre kinking) can be correctly predicted by the variation in the laminate's shear yield stress/strain with varying loading rate.
Additional tests were performed on laminates with multidirectional layups to check if the strain rate dependency prevails when plies of different orientations are combined to create more complex and widely used layups. The results indicate that the behaviour of these multidirectional laminates with increasing strain rate is governed by the mechanical properties increase of the 0° plies, as they are the main load-carrying plies.
Finally, chapter 3 finishes with the results of the experimental impact tests performed on a widely used structural component with a multidirectional layup subjected to three crashing speeds. It was concluded that the strain rate dependency verified on simple rectangular specimens is also detectable when testing specimens with a more complex shape, and the increase in maximum force is in line with the previously obtained for rectangular specimens.

Chapter 4 concerns the implementation of the experimentally obtained strain rate dependent compressive properties on a commercially available finite element software, and the subsequent impact simulations at different rates using models that replicate the experimental tests of chapter 3.
It initiates with a brief description of the implemented ply mechanics model and the damage

parameters that progressively decrease the ply properties. The strain rate dependent properties found experimentally are implemented in the model through the use of viscosity functions that dependent logarithmically on the strain rate. The rate dependent properties are then calibrated and validated using a single shell element model that reproduces the experimental impact tests on rectangular specimens. A very good correlation between experimental and simulation results is found for the longitudinal ply properties. For the transverse and shear ply properties, even though the simulation yield and fracture stress are on pair with the experimental results, the shape of the stress-strain curves is not entirely consistent due to changes in the matrix hardening law with increasing strain rate, which were not implemented in the numerical model.

A comparison between experimental and simulation results is also performed for the multi-directional laminates, in which a good agreement is found, mainly because the mechanical response of this laminates is dominated by the accurately implemented behaviour of 0° plies.

A final validation of the implemented strain rate dependent model is performed by comparing the experimental results on the omega-profile structural component with the simulation results of a 4224 shell elements model that replicates the impact experiments. The comparison between experiments and simulations results in a good agreement for the three impact velocities tested, especially for the maximum section force. These results indicate that the strain rate dependent compression properties of carbon-epoxy laminates can be determined experimentally via a series of dynamic tests on simple rectangular specimens, and then implemented on the simulation material card and used to perform crash simulations on components with complex shapes. The results of crash simulations performed on these complex structural components will lead to realistic failure loads because the rate dependent properties obtained in rectangular specimens are carried over quite equivalently to more complex parts.

Research Questions Answered

1. As there is no specimen geometry standard for dynamic testing, is there any influence of the geometrical factors on the measured properties of carbon-epoxy laminates?

The first research question has to do with the investigation performed in section 3.3 concerning the effects of each geometrical aspect of the rectangular specimens. It was found that only some factors have a considerable influence. The taper angle of the GFRP tabs and the width of the rectangular specimen show a critical influence on the measured compression strength. The specimen thickness and gauge length, however, display a less significant influence in the range tested.

From this investigation, an optimal specimen geometry based on the criterion of maximizing the compression strength has been derived and was adopted for the dynamic material characterization tests performed with rectangular specimens.

2. Is there any noticeable change in the compressive properties of carbon-epoxy laminates at different loading rates?

Following the experiments performed on rectangular specimens with five different layups subjected to six different impact velocities up to 1 m/s, the matrix-dominated compressive

properties of the tested carbon-epoxy system increase significantly between 27% and 56% over the respective QS values, while the fibre-dominated properties increased up to 26%.
The transverse and shear yield and fracture stress are the properties that increase the most with varying loading rates, exhibiting growths up to 56%. The longitudinal fracture strain and strength increased between 22% and 26% at a strain rate of approximately 5 s^{-1}, over the QS values. Neither the longitudinal, transverse or shear moduli suffered significant changes with varying loading rates.
These rate dependent properties were implemented in a numerical material card and an overall good agreement was found between simulation and experimental results. The simulations on multidirectional layups indicate that the behaviour of these layups can be accurately predicted by the implemented model, as the response obtained was very much alike the experimental data throughout the entire range of strain rates considered.

3. Is the strain rate dependency noticed on rectangular specimens also observable on more complex structural components?

This question can also be answered affirmatively. The impact tests performed on specimens with a more complex shape (such as the omega-profile cross-section) showed an increase in strength for higher rates which is on pair with the increase reached for simple rectangular specimens of a similar layup.
The maximum cross-section load of the omega-profile tested experimentally increased by 21% between QS and 1 m/s impactor velocities. The mechanical response of this component with a multidirectional layup is dominated by the plies aligned with the loading direction, as the increase in maximum force is analogous with the strength increase of 0° plies tested longitudinally.

5.1 Recommendations

5.1.1 Experimental Recommendations

The main improvement regarding the experimental setup is related with the high-speed cameras. As mentioned previously in section 2.6.1, during crash events of a car strain rates up to 200 s^{-1} are observable. However, in the current work, the maximum strain rate achieved ranges between 5 and 70 s^{-1}, depending of the specimen layup.
For a more accurate dynamic material characterisation, the tested range of loading rates should be extended up to 200 s^{-1}. Nonetheless, this was not possible because the high-speed cameras available for the current work were the limiting factor in terms of recording speed. For impact velocities higher than the ones used in the current work (faster than 1 m/s), the available high-speed cameras are not able to record a sufficient amount of frames during the impact event to allow for a proper analysis of the strain field. The testing machine, on the other hand, is not a limiting factor, as it can reach piston velocities up to 10 m/s, which is sufficient to increase the maximum specimen strain rate by a factor of 10.

5.1.2 Numerical Simulations Recommendations

Even though the strain rate dependent compressive properties of the tested carbon-epoxy laminate were numerically implemented with an overall acceptable correlation, there is still room for improvement, especially on the transverse and shear laminate response. As the experimental tests on transverse specimens showed, there is a growth in the yield stress and changes in the subsequent hardening law, with varying loading rates. The increase in yield stress was implemented in the numerical model, but the hardening law is assumed to be constant throughout the range of strain rates tested. This leads to disparities in the transverse stress-strain curves after yield between experiments and simulations at certain strain rates. Therefore, to obtain more accurate predictions, this evolution of the matrix hardening law for higher strain rates could be correctly implemented in the numerical model.

Another important aspect that should be kept in mind when running simulations with the implemented model is related with the longitudinal fracture strain and the laminate layup. As shown in sections 3.4.5 through 3.4.7, the strain at which the longitudinal fibres fail due to the formation of kink bands highly depends on the layup in which these 0° plies are embedded into. For example, when performing impact tests on rectangular specimens with a QI layup ($[+45°/-45°/0°/90°]_{2s}$), the fracture strain is 40 to 50% larger than when testing unidirectional specimens ($[0°]_{16}$ layup). This difference leads to issues in the implemented numerical model because failure is governed by the maximum strain criterion in the 0° plies. For this reason, the longitudinal fracture strain of the maximum strain failure criterion has to be adjusted in accordance with the layup of the component being simulation, to obtain a realistic failure strain.

Furthermore, in the current work, when performing impact experiments on the omega-profile structural component (which layup is close to QI), the failure strain was closer to the one obtained in unidirectional specimens, instead of being analogous to the QI rectangular specimens. This aspect was attributed to the manufacturing defects introduced during hand lay-up of the concave shape, which reduced the fracture strain as the formation of kink bands occurred at lower strain levels. Therefore, the simulations performed with the implemented omega-profile component model used the maximum longitudinal strain criterion analogous to that of unidirectional specimens, even if the layup was closer to the QI specimens.

In summary, the implemented maximum strain failure criterion in fibre-direction has to be adjusted for the layup of the component being simulated and the presence of manufacturing defects that affect the failure strain of the physical component.

References

[1] Y. Wang and Y. M. Xia. The effects of strain rate on the mechanical behaviour of kevlar fibre bundles: an experimental and theoretical study. *Composites Part a-Applied Science and Manufacturing*, 29(11):1411–1415, 1998.

[2] Y. M. Xia, J. M. Yuan, and B. C. Yang. A statistical-model and experimental-study of the strain-rate dependence of the strength of fibers. *Composites Science and Technology*, 52(4):499–504, 1994.

[3] Y. X. Zhou, D. Z. Jiang, and Y. M. Xia. Tensile mechanical behavior of t300 and m40j fiber bundles at different strain rate. *Journal of Materials Science*, 36(4):919–922, 2001.

[4] Y. X. Zhou, Y. Wang, Y. M. Xia, and S. Jeelani. Tensile behavior of carbon fiber bundles at different strain rates. *Materials Letters*, 64(3):246–248, 2010.

[5] A. Gilat, R. K. Goldberg, and G. D. Roberts. Experimental study of strain-rate-dependent behavior of carbon/epoxy composite. *Composites Science and Technology*, 62(10-11):1469–1476, 2002.

[6] A. Gilat, R. K. Goldberg, and G. D. Roberts. Strain rate sensitivity of epoxy resin in tensile and shear loading. *Journal of Aerospace Engineering*, 20(2):75–89, 2007.

[7] J. D. Littell, C. R. Ruggeri, R. K. Goldberg, G. D. Roberts, W. A. Arnold, and W. K. Binienda. Measurement of epoxy resin tension, compression, and shear stress-strain curves over a wide range of strain rates using small test specimens. *Journal of Aerospace Engineering*, 21(3):162–173, 2008.

[8] R. Gerlach, C. R. Siviour, N. Petrinic, and J. Wiegand. Experimental characterisation and constitutive modelling of rtm-6 resin under impact loading. *Polymer*, 49(11):2728–2737, 2008.

[9] W. Chen, F. Lu, and M. Cheng. Tension and compression tests of two polymers under quasistatic and dynamic loading. *Polymer Testing*, 21(2):113–121, 2002.

[10] Y. Tian, H. Zhang, J. Zhao, T. Li, B. X. Bie, S. N. Luo, and Z. Zhang. High strain rate compression of epoxy based nanocomposites. *Composites Part a-Applied Science and Manufacturing*, 90:62–70, 2016.

[11] J. Harding and L. M. Welsh. A tensile testing technique for fiber-reinforced composites at impact rates of strain. *Journal of Materials Science*, 18(6):1810–1826, 1983.

[12] N. Taniguchi, T. Nishiwaki, and H. Kawada. Tensile strength of unidirectional cfrp laminate under high strain rate. *Advanced Composite Materials*, 16(2):167–180, 2007.

[13] B. R. K. Blackman, J. P. Dear, A. J. Kinloch, H. Macgillivray, Y. Wang, J. G. Williams, and P. Yayla. The failure of fibre composites and adhesively bonded fibre composites under high rates of test .1. mode i loading - experimental studies. *Journal of Materials Science*, 30(23):5885–5900, 1995.

[14] H. M. Hsiao and I. M. Daniel. Strain rate behavior of composite materials. *Composites Part B-Engineering*, 29(5):521–533, 1998.

[15] M. V. Hosur, J. Alexander, U. K. Vaidya, and S. Jeelani. High strain rate compression response of carbon/epoxy laminate composites. *Composite Structures*, 52(3-4):405–417, 2001.

[16] Q. D. Bing and C. T. Sun. Modeling and testing strain rate-dependent compressive strength of carbon/epoxy composites. *Composites Science and Technology*, 65(15-16):2481–2491, 2005.

[17] H. Koerber and P. P. Camanho. High strain rate characterisation of unidirectional carbon-epoxy im7-8552 in longitudinal compression. *Composites Part A: Applied Science and Manufacturing*, 42(5):462–470, 2011.

[18] I. M. Daniel, H. M. Hsiao, and S. C. Wooh. Failure mechanisms in thick composites under compressive loading. *Composites Part B-Engineering*, 27(6):543–552, 1996.

[19] Bernard Budiansky and Norman A. Fleck. Compressive kinking of fiber composites: A topical review. *Applied Mechanics Reviews*, 47(6S):S246, 1994.

[20] A. Jumahat, C. Soutis, F. R. Jones, and A. Hodzic. Fracture mechanisms and failure analysis of carbon fibre/toughened epoxy composites subjected to compressive loading. *Composite Structures*, 92(2):295–305, 2010.

[21] H. M. Hsiao, I. M. Daniel, and R. D. Cordes. Strain rate effects on the transverse compressive and shear behavior of unidirectional composites. *Journal of Composite Materials*, 33(17):1620–1642, 1999.

[22] H. Koerber, J. Xavier, and P. P. Camanho. High strain rate characterisation of unidirectional carbon-epoxy im7-8552 in transverse compression and in-plane shear using digital image correlation. *Mechanics of Materials*, 42(11):1004–1019, 2010.

[23] ASTMD3518. Standard test method for in-plane shear response of polymer matrix composite materials by tensile test of a ±45° laminate. *ASTM International, West Conshohocken, PA*, 2001.

[24] G. H. Staab and A. Gilat. High-strain rate response of angle-ply glass epoxy laminates. *Journal of Composite Materials*, 29(10):1308–1320, 1995.

[25] M. M. Shokrieh and M. J. Omidi. Investigation of strain rate effects on in-plane shear properties of glass/epoxy composites. *Composite Structures*, 91(1):95–102, 2009.

[26] H. Cui, D. Thomson, A. Pellegrino, J. Wiegand, and N. Petrinic. Effect of strain rate and fibre rotation on the in-plane shear response of ±45° laminates in tension and compression tests. *Composites Science and Technology*, 135:106–115, 2016.

[27] J. L. Tsai and C. T. Sun. Strain rate effect on in-plane shear strength of unidirectional polymeric composites. *Composites Science and Technology*, 65(13):1941–1947, 2005.

[28] E. T. Camponeschl. Compression testing of thick-section composite materials. *Composite Materials Fatigue and Fracture (Third Volume).*, pages 439–456, 1991.

[29] H. M. Hsiao, I. M. Daniel, and S. C. Wooh. A new compression test method for thick composites. *Journal of Composite Materials*, 29(13):1789–1806, 1995.

[30] J. Lee and C. Soutis. A study on the compressive strength of thick carbon fibre-epoxy laminates. *Composites Science and Technology*, 67(10):2015–2026, 2007.

[31] J. Lee and C. Soutis. Measuring the notched compressive strength of composite laminates: Specimen size effects. *Composites Science and Technology*, 68(12):2359–2366, 2008.

[32] Q. Bing and C. T. Sun. Specimen size effect in off-axis compression tests of fiber composites. *Composites Part B-Engineering*, 39(1):20–26, 2008.

[33] J. M. Whitney and N. J. Pagano. Shear deformation in heterogeneous anisotropic plates. *Journal of Applied Mechanics*, 37(4):1031, 1970.

[34] ASTMD3410. Standard test method for compressive properties of polymer matrix composite materials with unsupported gage section by shear loading. *ASTM International, West Conshohocken, PA*, 2016.

[35] M. Xie and D. F. Adams. Tab adhesive in a composite compression specimen. *Polymer Composites*, 16(6):529–535, 1995.

[36] M. Xie and D. F. Adams. Effect of specimen tab configuration on compression testing of composite materials. *Journal of Composites Technology & Research*, 17(2):77–83, 1995.

[37] ASTMD6641. Standard test method for compressive properties of polymer matrix composite materials using a combined loading compression (clc) test fixture. *ASTM International, West Conshohocken, PA*, 2016.

[38] B. P. Bussadori, K. Schuffenhauer, and A. Scattina. Modelling of cfrp crushing structures in explicit crash analysis. *Composites Part B-Engineering*, 60:725–735, 2014.

[39] E. V. Morozov and V. A. Thomson. Simulating the progressive crushing of fabric reinforced composite structures. *Composite Structures*, 76(1-2):130–137, 2006.

[40] M. A. McCarthy, J. R. Xiao, N. Petrinic, A. Kamoulakos, and V. Melito. Modelling of bird strike on an aircraft wing leading edge made from fibre metal laminates - part 1: Material modelling. *Applied Composite Materials*, 11(5):295–315, 2004.

[41] M. A. McCarthy, J. R. Xiao, C. T. McCarthy, A. Kamoulakos, J. Ramos, J. P. Gallard, and V. Melito. Modelling of bird strike on an aircraft wing leading edge made from fibre metal laminates - part 2: Modelling of impact with sph bird model. *Applied Composite Materials*, 11(5):317–340, 2004.

[42] M. Schossig. *Schaedigungsmechanismen in faserverstaerkten Kunststoffen.* Thesis, 2011.

[43] I. M. Daniel, B. T. Werner, and J. S. Fenner. Strain-rate-dependent failure criteria for composites. *Composites Science and Technology*, 71(3):357–364, 2011.

[44] J. E. Field, S. M. Walley, W. G. Proud, H. T. Goldrein, and C. R. Siviour. Review of experimental techniques for high rate deformation and shock studies. *International Journal of Impact Engineering*, 30(7):725–775, 2004.

[45] H. Zhao and G. Gary. On the use of shpb techniques to determine the dynamic behavior of materials in the range of small strains. *International Journal of Solids and Structures*, 33(23):3363–3375, 1996.

[46] H. Meng and Q. M. Li. Correlation between the accuracy of a shpb test and the stress uniformity based on numerical experiments. *International Journal of Impact Engineering*, 28(5):537–555, 2003.

[47] B. Pan, K. M. Qian, H. M. Xie, and A. Asundi. Two-dimensional digital image correlation for in-plane displacement and strain measurement: a review. *Measurement Science and Technology*, 20(6), 2009.

[48] M. Sutton, J. Orteu, and H. Schreier. *Image Correlation for Shape, Motion and Deformation Measurements.* Springer, 2009.

[49] Schmack T. *Entwicklung von Methoden fur die Hochgeschwindigkeitsprufung von Faserverbundkunststoffen.* Thesis, 2015.

[50] D. F. Adams and E. M. Odom. Influence of specimen tabs on the compressive strength of a unidirectional composite-material. *Journal of Composite Materials*, 25(6):774–786, 1991.

[51] C. Kassapoglou. *Design and Analysis of Composite Structures: with Applications to Aerospace Structures.* The Aerospace Series. Wiley, United Kingdom, 1st edition, 2010.

[52] P. Ladeveze and E. Ledantec. Damage modeling of the elementary ply for laminated composites. *Composites Science and Technology*, 43(3):257–267, 1992.

[53] M. P. Rozycki. *Contribution au developpement de lois de comportement pour materiaux composites soumis a l'impact.* Phd thesis, 2000.

[54] J. Robinson. A single element test. *Computer Methods in Applied Mechanics and Engineering*, 7(2):191–200, 1976.

Appendix A

Fixture Modal Analysis

During the early experimental tests performed on rectangular carbon-epoxy specimens, it was noted that at an impactor velocity of 1 m/s, the load signal generated by the piezoelectric load cell mounted on the testing fixture was being significantly affected by noise.
At low testing speeds, the load signal was increasing at a constant rate until specimen failure, causing the load being measured to suddenly drop to zero. However, as Figure A.1 shows, the load signal with an impactor velocity of 1 m/s was being superimposed by what seems to be a sinusoidal wave with an approximate frequency of 1000 Hz. This noise signal was also apparent in the pictures obtained from the high-speed cameras, in which it was possible to see that the entire fixture was vibrating.

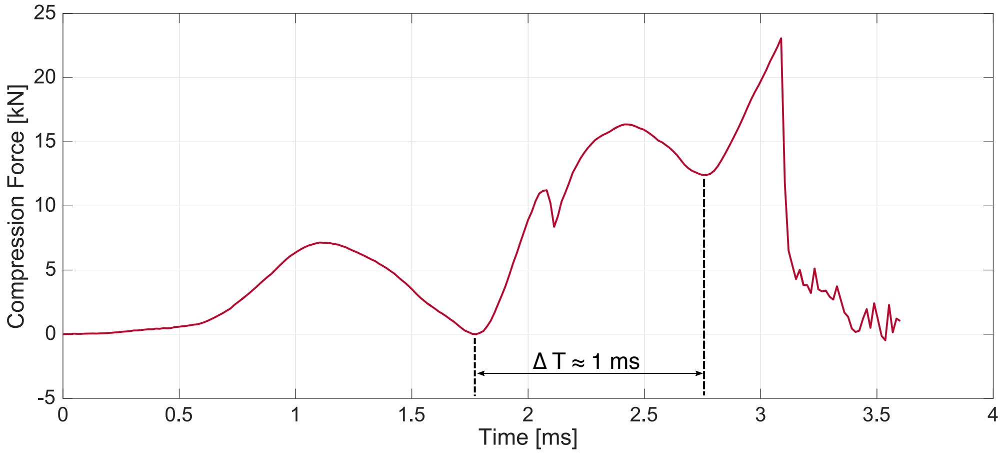

Figure A.1: 1 m/s load signal with superimposed fixture noise and indication of noise period.

It was decided to investigate the cause of this noisy force signal at high testing speeds, as it could be affecting the results being obtained. A possible reason could be that the entire fixture holding the specimen starts to vibrate at its eigenfrequencies when hit by the impactor at high velocity. As the impactor and the part of the fixture being hit are both made of steel, it was plausible that after the initial impact, there was a detachment between these two parts, causing the fixture to receive an excitation which approximates a Dirac delta function.

An accurate way to determine the fixture's natural frequencies is to employ a modal analysis technique. The method used in the current work consists of using an impulse hammer to hit and excite the fixture with a signal that is very close to a Dirac delta function, as Figure A.2 shows. Using the load cell incorporated in the fixture, its vibration after the impulse of the hammer is recorded (see Figure A.2) and analysed.

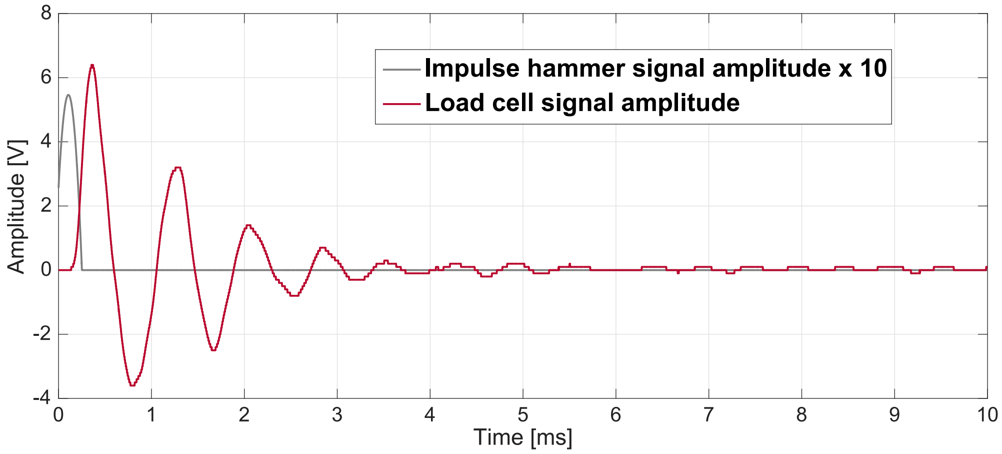

Figure A.2: Impulse hammer and load cell signals after stimulus with impulse hammer.

The signal of the fixture's vibration coming from the load cell can be converted from the time domain into the frequency domain using a fast Fourier transform (FFT) to better analyse the natural frequency. The results of applying a FFT to the signal of Figure A.2 are presented in Figure A.3.

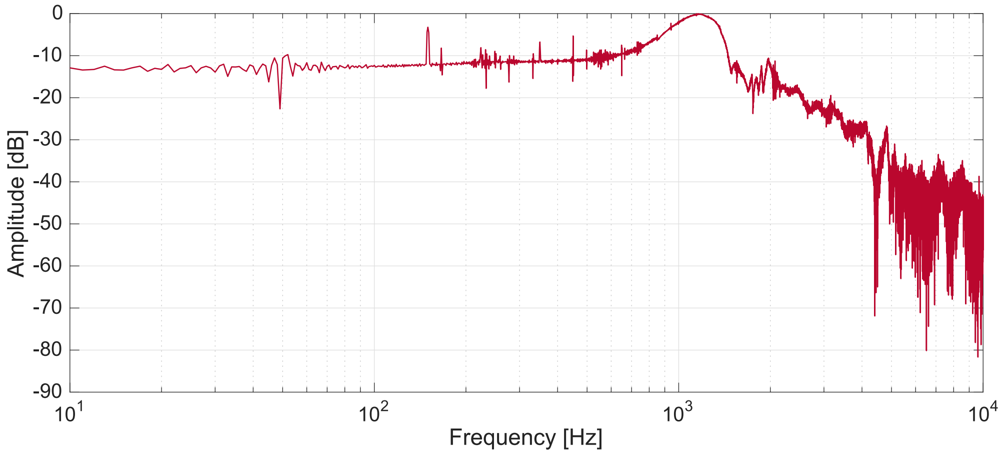

Figure A.3: Response of the fixture to an impulse stimulus in the frequency domain.

In the frequency domain, the natural frequency of the fixture is easily determined by finding the peak of Figure A.3, which is at approximately 1163 Hz.

Previously in Figure A.1 it was indicated that the noise on the load cell signal when testing at 1 m/s was at a frequency of approximately 1000 Hz, which is very much alike the natural frequency of 1163 Hz found for the fixture. Therefore, it can be concluded that the noise is indeed due to the fixture being excited by the impactor and vibrating at its natural frequencies. A possible solution for this issue is to change the mas of the fixture, thus altering its natural frequencies. The natural frequency changes with varying mass according to:

$$\text{natural frequency} \propto \frac{1}{\sqrt{\text{mass}}} \tag{A.1}$$

which means that, by increasing the mass of the fixture, its natural frequency decreases (thus, increasing the period of oscillation). If the period of oscillation increases significantly such that it becomes somewhat longer than the entire duration of the experimental test at an impactor velocity of 1 m/s (approximately 3 to 4 ms), its influence on the measured signal is fairly reduced.

One of the fixture's main components was redesigned to becomes a solid piece of steel, which increased its mass by a factor of 4. This increase in mass led to a significant effect on the load signal being measured when testing at 1 m/s, as the effect of the fixture's vibration at its natural frequencies was considerably reduced, as Figure A.4 shows.

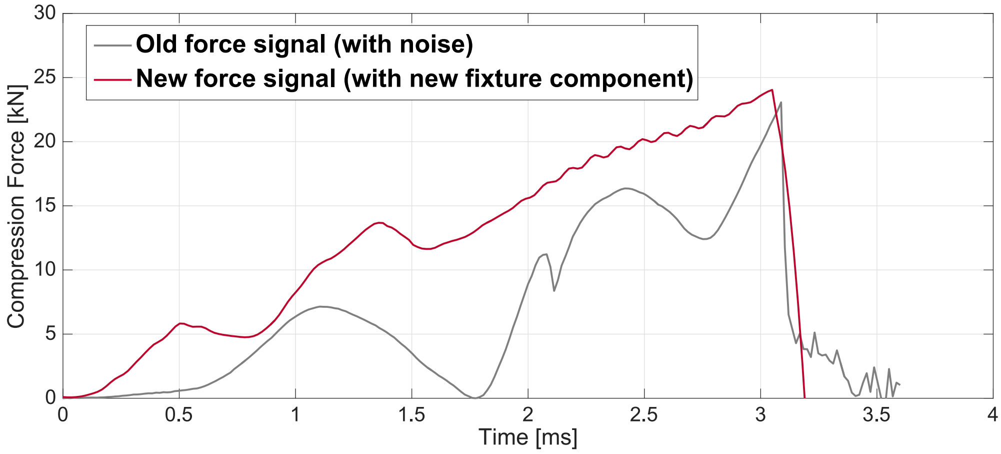

Figure A.4: Comparison of load cell signal before and after performing modal analysis and modifying the fixture mass.

The load signal after applying changes to the fixture, even though it still shows quite some significant vibrations in the beginning of the test, becomes smoother during the second half of the test, and, consequently, a constant strain rate is reached before specimen failure.

Appendix B

Comparison Between Experimental and Simulation Stress-strain Curves

In the current Appendix, the stress-strain curves obtained experimentally and presented in section 3.4 are plotted together with the numerically obtained stress-strain curves used to calibrate the simulation model, using the one-element shell model.

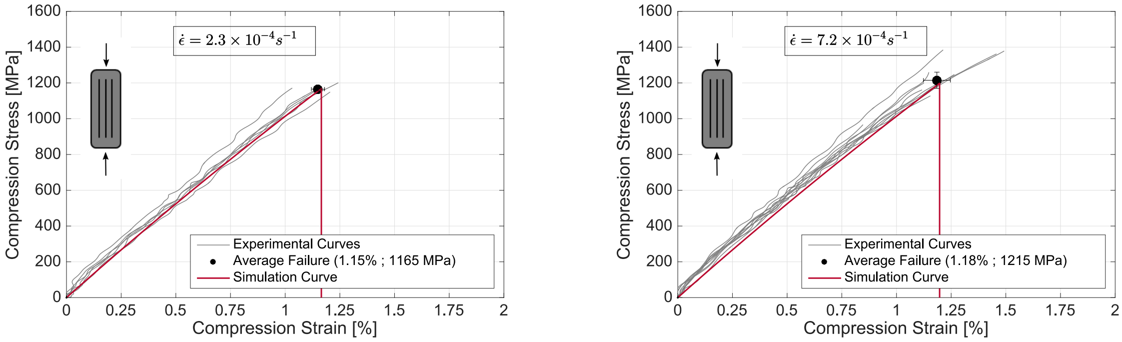

(a) $\dot{\varepsilon} \approx 2.3 \times 10^{-4}\ s^{-1}$

(b) $\dot{\varepsilon} \approx 7.2 \times 10^{-4}\ s^{-1}$

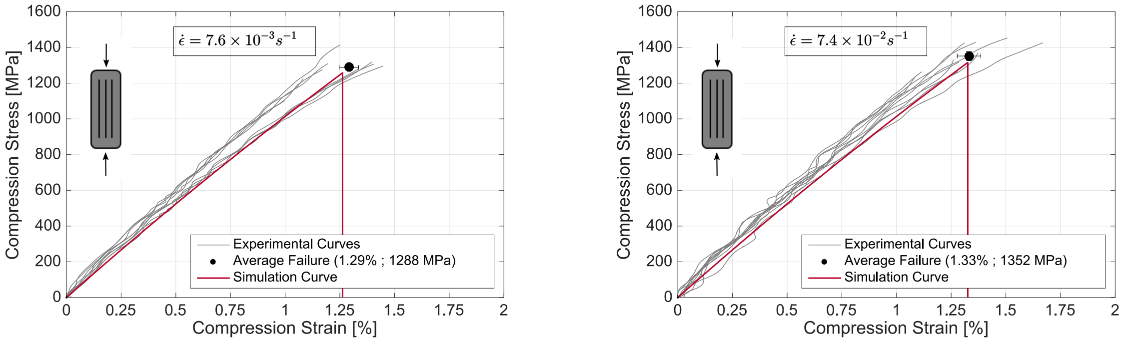

(c) $\dot{\varepsilon} \approx 7.6 \times 10^{-3}\ s^{-1}$

(d) $\dot{\varepsilon} \approx 7.4 \times 10^{-2}\ s^{-1}$

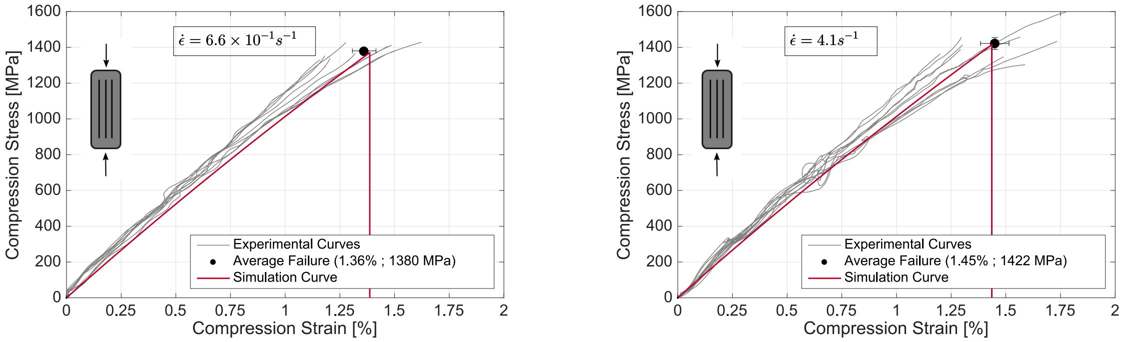

(e) $\dot{\varepsilon} \approx 6.6 \times 10^{-1}\ s^{-1}$

(f) $\dot{\varepsilon} \approx 4.1\ s^{-1}$

Figure B.1: Experimental and simulation stress-strain curves of $[0°]_{16}$ layup specimens at different strain rates.

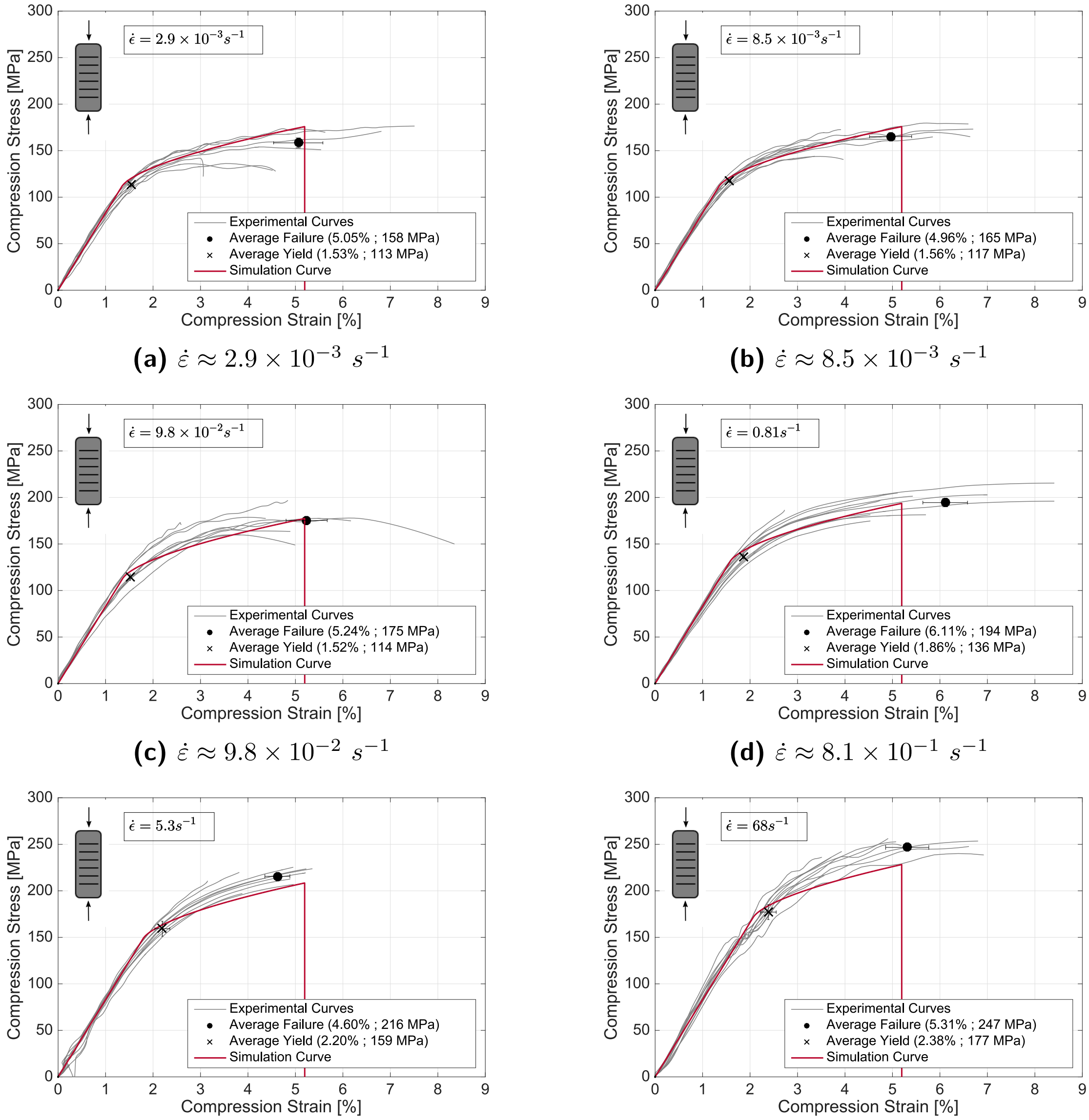

(a) $\dot{\varepsilon} \approx 2.9 \times 10^{-3}\ s^{-1}$

(b) $\dot{\varepsilon} \approx 8.5 \times 10^{-3}\ s^{-1}$

(c) $\dot{\varepsilon} \approx 9.8 \times 10^{-2}\ s^{-1}$

(d) $\dot{\varepsilon} \approx 8.1 \times 10^{-1}\ s^{-1}$

(e) $\dot{\varepsilon} \approx 5.3\ s^{-1}$

(f) $\dot{\varepsilon} \approx 68\ s^{-1}$

Figure B.2: Experimental and simulation stress-strain curves of $[90°]_{16}$ layup specimens at different strain rates.

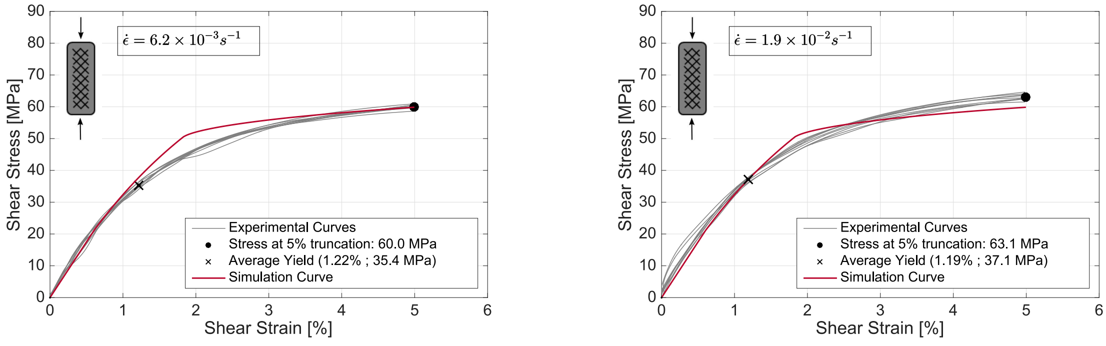

(a) $\dot{\varepsilon} \approx 6.2 \times 10^{-3}\ s^{-1}$ **(b)** $\dot{\varepsilon} \approx 1.9 \times 10^{-2}\ s^{-1}$

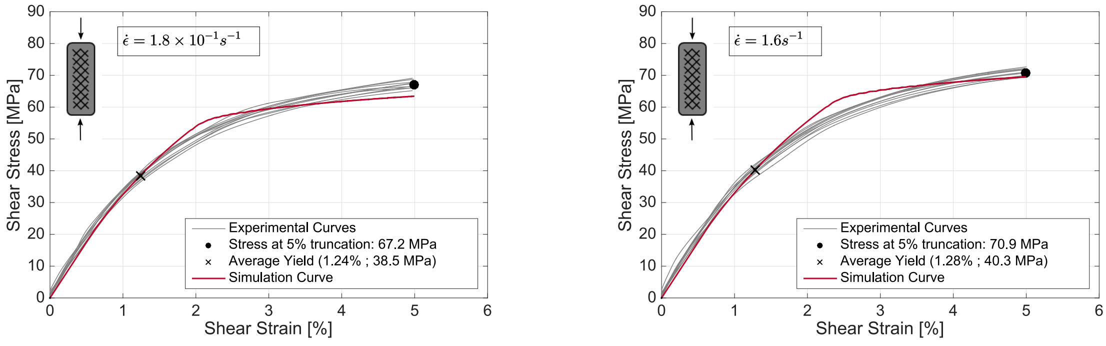

(c) $\dot{\varepsilon} \approx 1.8 \times 10^{-1}\ s^{-1}$ **(d)** $\dot{\varepsilon} \approx 1.6\ s^{-1}$

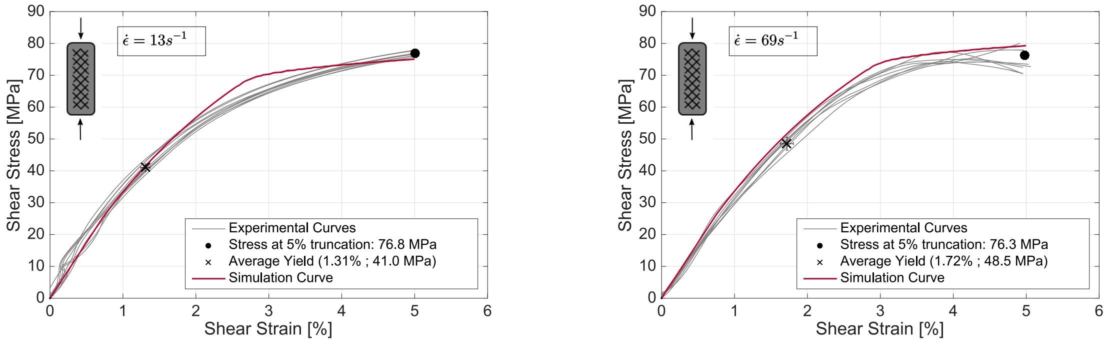

(e) $\dot{\varepsilon} \approx 13\ s^{-1}$ **(f)** $\dot{\varepsilon} \approx 69\ s^{-1}$

Figure B.3: Experimental and simulation stress-strain curves of $[+45°/-45°]_{4s}$ layup specimens at different strain rates.

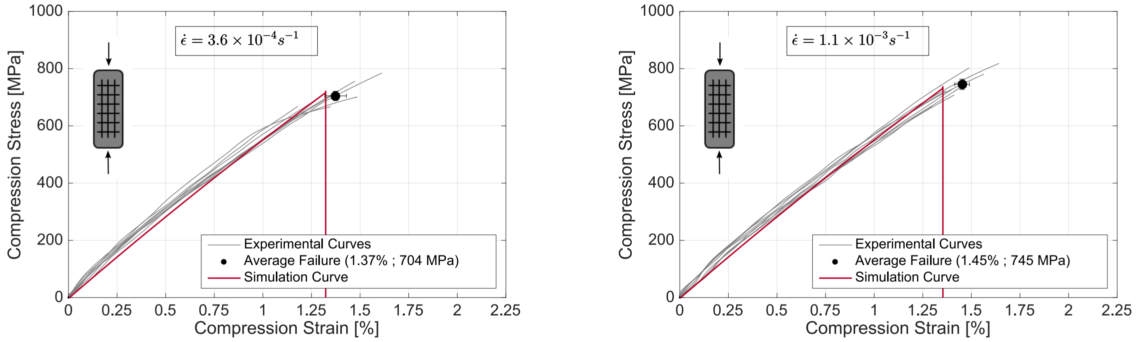

(a) $\dot{\varepsilon} \approx 3.6 \times 10^{-4}\ s^{-1}$ **(b)** $\dot{\varepsilon} \approx 1.1 \times 10^{-3}\ s^{-1}$

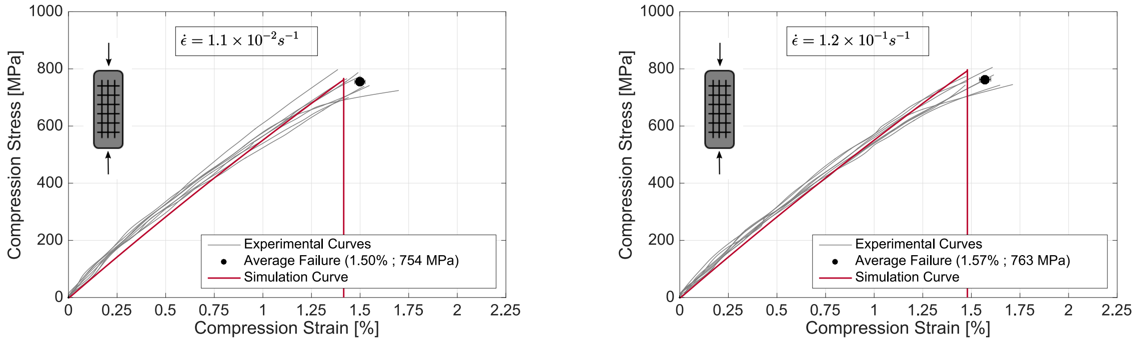

(c) $\dot{\varepsilon} \approx 1.1 \times 10^{-2}\ s^{-1}$ **(d)** $\dot{\varepsilon} \approx 1.2 \times 10^{-1}\ s^{-1}$

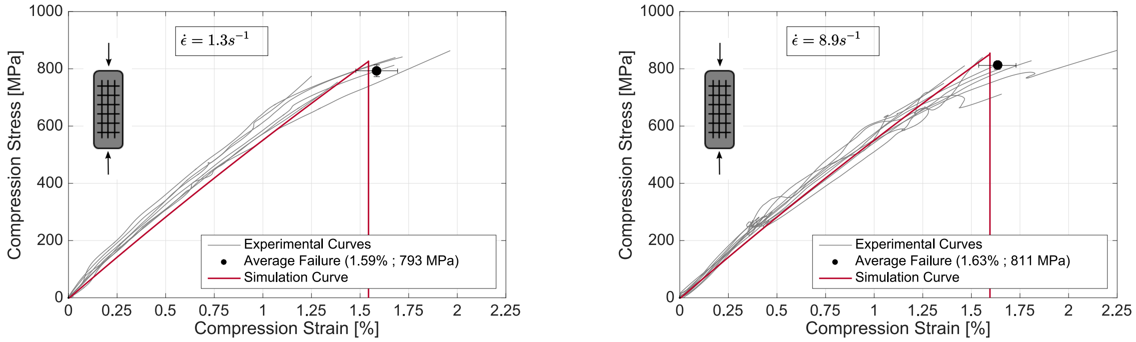

(e) $\dot{\varepsilon} \approx 1.3\ s^{-1}$ **(f)** $\dot{\varepsilon} \approx 8.9\ s^{-1}$

Figure B.4: Experimental and simulation stress-strain curves of $[0°/90°]_{4s}$ layup specimens at different strain rates.

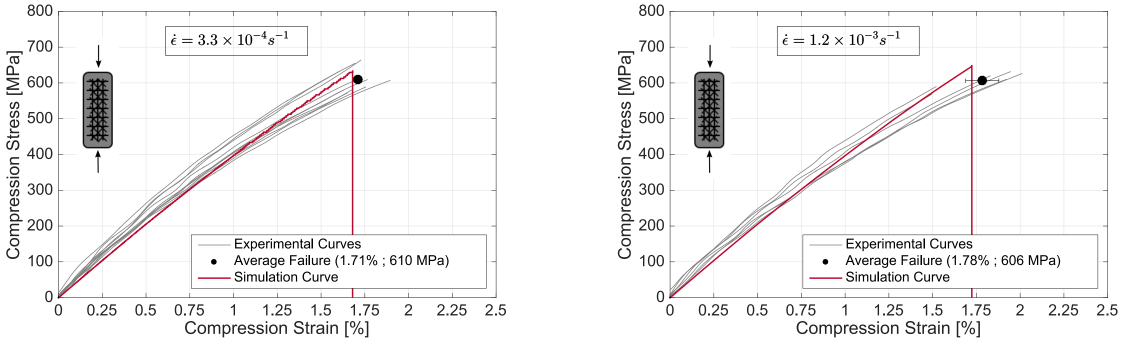

(a) $\dot{\varepsilon} \approx 3.3 \times 10^{-4}\ s^{-1}$ **(b)** $\dot{\varepsilon} \approx 1.2 \times 10^{-3}\ s^{-1}$

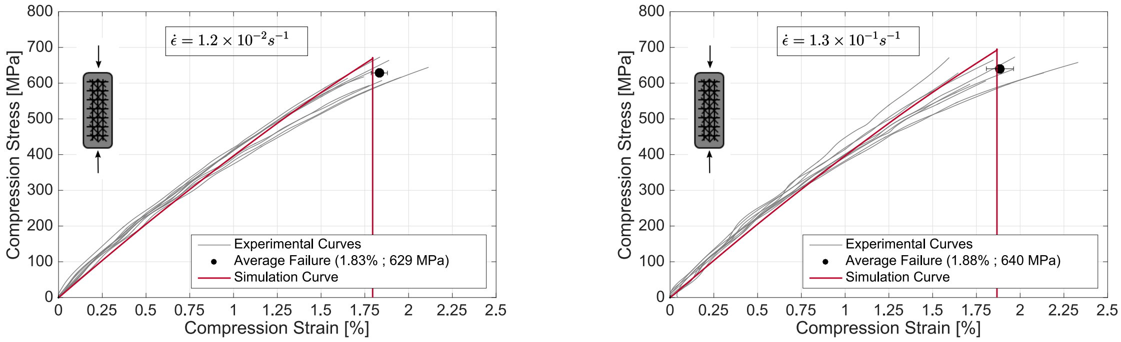

(c) $\dot{\varepsilon} \approx 1.2 \times 10^{-2}\ s^{-1}$ **(d)** $\dot{\varepsilon} \approx 1.3 \times 10^{-1}\ s^{-1}$

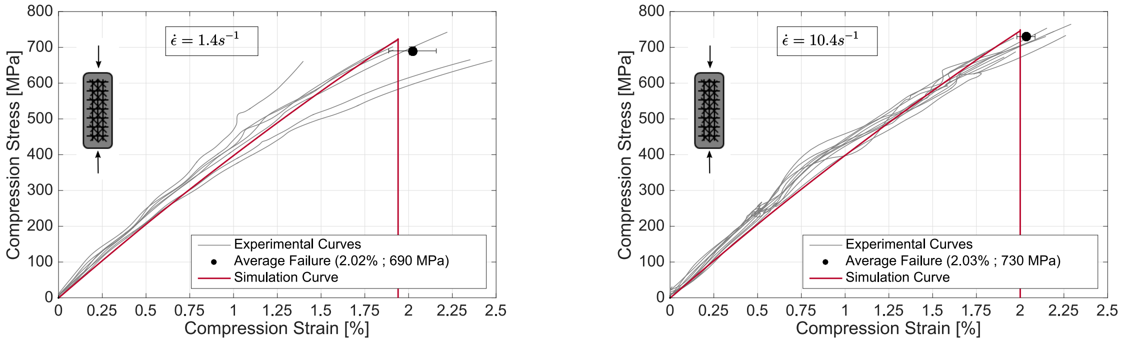

(e) $\dot{\varepsilon} \approx 1.4\ s^{-1}$ **(f)** $\dot{\varepsilon} \approx 10.4\ s^{-1}$

Figure B.5: Experimental and simulation stress-strain curves of QI ($[+45°/-45°/0°/90°]_{2s}$) layup specimens at different strain rates.

Appendix C

Omega-profile Simulation Model Mesh Convergence Study

A mesh convergence study was performed to determine the necessary number of nodes/elements that assures convergence in the results for the simulations of the omega-profile structural component model. Figure C.1 depicts how the internal strain energy and the peak section force at failure evolve with different mesh refinements.

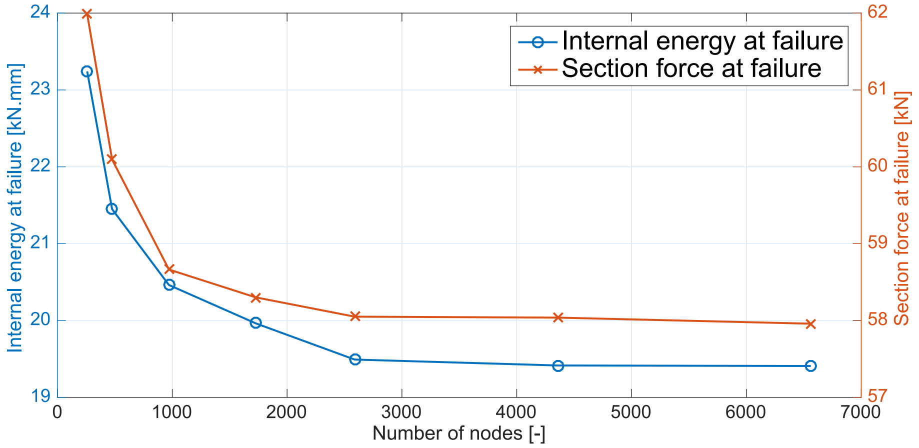

Figure C.1: Internal strain energy and section force at failure as functions of the number of nodes for the omega-profile structure model simulated at QS speeds.

The results indicate that after 4356 nodes, the model is converged and refining the mesh further leads to no significant changes in the results. Therefore, a model with 4356 nodes was adopted for the dynamic simulations performed and presented in section 4.3, which corresponds to 4224 shell elements with a side length of approximately 1.5 mm.